IPP-Report

MAX-PLANCK-INSTITUT
FÜR PLASMAPHYSIK

Christian Schuster

Influence of Fuelling on Transport in the Tokamak Edge Plasma

IPP 2023-05
Juni 2023

TUM SCHOOL OF NATURAL SCIENCES

TECHNISCHE UNIVERSITÄT MÜNCHEN

Influence of Fuelling on Transport in the Tokamak Edge Plasma

Christian Schuster

Vollständiger Abdruck der von der TUM School of Natural Sciences der Technischen Universität München zur Erlangung des akademischen Grades eines Doktors der Naturwissenschaften genehmigten Dissertation.

Vorsitz:		Prof. Dr. Andreas Weiler
Prüfer der Dissertation:	1.	Prof. Dr. Ulrich Stroth
	2.	Prof. Dr. Lorenzo Frassinetti

Die Dissertation wurde am 11.01.2023 bei der Technischen Universität München eingereicht und durch die TUM School of Natural Sciences am 13.03.2023 angenommen.

TUM SCHOOL OF NATURAL SCIENCES
TECHNISCHE UNIVERSITÄT MÜNCHEN

Influence of Fuelling on Transport in the Tokamak Edge Plasma

Author:	Christian Schuster
Supervisor:	Prof. Dr. Ulrich Stroth
Advisor:	Prof. Dr. Elisabeth Wolfrum
Submission Date:	January 11th, 2023

Abstract

Controlled thermonuclear fusion is envisioned as a sustainable energy source which does not emit green house gases during operation. To achieve the necessary high temperatures, the hydrogen plasma can be confined by magnetic fields in different configurations, the tokamak concept being the one which is developed the furthest. The confinement of the plasma has to be sufficient: Particles, i.e. density, and heat are transported radially, mainly due to turbulence. Heat transport is diffusive, leading to a power flux from the hot core outside. For particles, there are additional convective contributions, whose existence in the plasma edge is an open question. In this work, the influx of neutral hydrogen gas into the tokamak vessel is modulated to gain additional information about transport from the temporal evolution of the plasma. The discharges are subsequently modelled with the transport code ASTRA.

It is shown that fuelling increases both heat and particle transport at the outermost confined radii, just inside the so-called *separatrix*, for the investigated L-mode, H-mode, EDA H-mode and QCE discharges. Particle transport increases stronger close to the separatrix than in the rest of the steep gradient region. Transport and *collisionality*, a parameter found important in various turbulence studies, are strongly correlated. Transport reacts also further inside, with the response depending on the plasma scenario. The changing transport coefficients introduce additional unknowns, making the determination of particle diffusivity and convection impossible, a finding that challenges previous results. The density evolution for all scenarios can be explained with a particle source that increases with fuelling, and purely diffusive particle transport, which changes analogously to heat transport. A pinch is not required. Linear and local turbulence simulations with GENE are able to reproduce the experimental findings for L-mode and the QCE pedestal. For future reactors, a density gradient in the edge plasma is predicted, even if particle transport is purely diffusive.

Zusammenfassung

Die kontrollierte Kernfusion wäre eine nachhaltige Energiequelle, bei deren Betrieb keine Treibhausgase freigesetzt werden. Um die erforderlichen hohen Temperaturen zu erreichen, kann das Wasserstoffplasma durch Magnetfelder in verschiedenen Konfigurationen eingeschlossen werden, wobei das Tokamak-Konzept am weitesten entwickelt ist. Der Einschluss des Plasmas muss ausreichend sein: Teilchen, d.h. die Dichte, und Wärme werden radial transportiert, hauptsächlich aufgrund von Turbulenz. Der Wärmetransport ist diffusiv und führt zu einem Leistungsfluss vom heißen Zentrum nach außen. Für Teilchen gibt es zusätzliche konvektive Beiträge, deren Existenz im Plasmarand eine offene Frage ist. In dieser Arbeit wird der Zufluss von neutralem Wasserstoffgas in das Tokamak-Gefäß moduliert, um zusätzliche Informationen über den Transport aus der zeitlichen Entwicklung des Plasmas zu gewinnen. Die Entladungen werden anschließend mit dem Transportcode ASTRA modelliert.

Für die untersuchten L-Mode-, H-Mode-, EDA-H-Mode- und QCE-Entladungen wird gezeigt, dass das Einleiten von Wasserstoffgas sowohl den Wärme- als auch den Teilchentransport an den äußersten begrenzten Radien, direkt innerhalb der sogenannten Separatrix, erhöht. Der Teilchentransport nimmt in der Nähe der Separatrix stärker zu als im übrigen Bereich des steilen Randdichtegradienten. Transport und Kollisionalität, ein Parameter, der in verschiedenen Turbulenzstudien als wichtig eingestuft wurde, sind stark korreliert. Der Transport reagiert auch weiter innen, wobei die Reaktion vom Plasmaszenario abhängt. Die sich ändernden Transportkoeffizienten führen zusätzliche Unbekannte ein, die die Bestimmung der Teilchendiffusivität und der Konvektion unmöglich machen, ein Ergebnis, das bisherige Ergebnisse in Frage stellt. Die Dichteentwicklung für alle Szenarien kann mit einer Teilchenquelle erklärt werden, die mit Wasserstoffeinleitung zunimmt, und einem rein diffusiven Teilchentransport, der sich analog zum Wärmetransport verändert. Ein Pinch ist nicht erforderlich. Lineare und lokale Turbulenzsimulationen mit GENE sind in der Lage, die experimentellen Ergebnisse für die L-Mode und das QCE-Pedestal zu reproduzieren. Für zukünftige Reaktoren wird ein Dichtegradient im Randplasma vorhergesagt, auch wenn der Teilchentransport rein diffusiv ist.

Contents

1. Introduction

Since the beginning of the industrial revolution the global energy demand is on a steep rise, which is predominately being met by burning fossil fuels [Smi16]. The green house gasses emitted in the process lead to an increase in the global temperature and an increasing number of weather extremes such as droughts, heatwaves, heavy precipitation and tropical cyclones that are already experienced today [MD21, pars. A.1 and A.3].

The U.S. Energy Information Administration estimates an increase of the global energy demand by nearly 50 % until 2050 [IEO21]: most of the additional demand would be met by renewable energy sources. However, the absolute contribution of fossil fuels would also grow. This results in a rise of the global surface temperature by $\approx 3\,^{\circ}\mathrm{C}$ by the end of the century [MD21, SPM.1.4]. Additional to the increase of the mean temperature, weather extremes would continue to increase in frequency and intensity [MD21, B.2, figure SPM.6]: for example, intense heat waves which occurred once in 50 years before 1900 would occur 10 to 40 times in the same time span.

New technologies, not exclusively but also for supplying energy, have the potential to reduce green house gas emissions. One option for weather independent and carbon lean energy is the fusion of light nuclei in a power plant on earth, similar to hydrogen fusion in stars. Plant construction and operation would result in the emission of some green house gases, as with renewable energy sources or fission power plants. The fusion reaction itself does not yield any green house gases.

Fusion will most likely not be the main solution for climate change: in the Paris Agreement [Par15] the participating nations agree to holding the temperature increase well below $2\,^{\circ}\mathrm{C}$ compared to pre-industrial levels. As discussed, this requires reducing carbon emissions well before 2050. The 'European Research Roadmap to the Realisation of Fusion Energy' [Roa18] however estimates that electricity from the prototype fusion reactor DEMO will be available only 'early in the second part of this century'. Fusion is still not obsolete: increasing the fraction of renewables in the energy mix becomes more and more difficult because their power output is depending on external factors and ill-suited for baseline power provisioning [Nic21]. Fusion could help in making this remaining fraction sustainable.

1.1. Thermonuclear Fusion

Atomic nuclei harbor vast amounts of energy. This energy can, for example, be released by

Fission Splitting the nucleus of an heavy element, e.g. uranium

Fusion Merging the nuclei of light elements, e.g. hydrogen

Splitting and fusing nuclei are two opposite actions. So why, depending on the size of the nucleus, both splitting and fusing nuclei can release energy? Following Krane [Kra91, section 3.3] we find the explanation:

Nucleons, i.e. protons and neutrons, are attracted to each other due to the nuclear force, while protons repel each other due to the electrostatic force. The nuclear force between two adjacent protons is stronger than the electrostatic repulsion between them. However, the nuclear force only acts on short length scales while the electrostatic force is also effective across large distances.

When a single proton or a whole light nucleus is added to another light nucleus, the nuclear force acts between all nucleons and binds them tightly to each other. This drop in potential energy is released in the reaction, making the fusion of light elements exothermic.

If one continues to add nucleons, the nucleus grows larger than the length scale on which the nuclear force can act. The new nucleons are then attracted only to their neighboring nucleons within reach of the nuclear force. They are however electrostatically repelled by all protons in the nucleus. Thus, the larger the nucleus becomes, the less influence the attracting nucleons have compared to the repulsion from the whole nucleus. When fusing two large nuclei, energy has to be added to overcome this large electrostatic repulsion among protons. Therefore, fusion is an endothermic reaction for heavy nuclei.

Summarizing, on one hand it is energetically favorable to split uranium into smaller nuclei because it reduces electrostatic repulsion, but on the other hand it is energetically favorable to fuse hydrogen to helium because of the attractive nuclear force.

Fusing two nuclei requires reducing the distance separating them sufficiently for the nuclear force to bind them together. The Coulomb repulsion between the nuclei hinders fusion in two ways:

- The electrostatic repulsion forms a potential energy hill called the Coulomb barrier. The center-of-mass energy of the nuclei has to be sufficiently high to overcome the Coulomb barrier. Fusion is still achievable: quantum mechanical tunneling greatly reduces the required energy. And if the incident nuclei originate from thermal distributions, the high energy tail of the Maxwellian leads to fusion reactions even if the thermal energy is low. [Kra91, section 14.2]

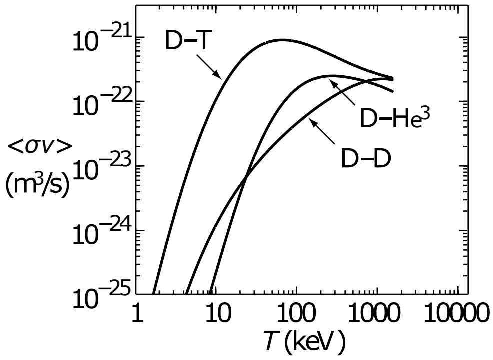

Figure 1.1.: The fusion rates of deuterium with deuterium, tritium and helium-3 as a function of temperature. While all three reactions occur with comparable rates at $T \approx 1\,\mathrm{MeV}$, the D-T reaction is far more probable at lower temperatures. Figure from Freidberg [Fre08].

- Fusion between two incident nuclei is far less likely than Coulomb scattering [Kra91, chapter 14]. Beam ions lose their energy too fast in such elastic collisions to be able to result in a positive energy balance [Wes11, section 1.1]. In thermonuclear fusion, scattering does not (directly) waste energy because the fuel is anyways in thermal equilibrium, making it the most promising candidate for fusion power plants on earth [Wes11, section 1.1].

The most promising fuel for terrestrial fusion reactors is a mixture consisting of equal parts of deuterium (denoted as D or ^{2}H) and tritium (denoted as T or ^{3}H), aiming at the reaction [Wes11, Fre08]

$$\mathrm{D}^+ + \mathrm{T}^+ \longrightarrow {}^4\mathrm{He}^{2+} + \mathrm{n} + 17.58\,\mathrm{MeV}. \tag{1.1}$$

The benefits of this reaction are the comparably large energy release and the large reaction rates, compared to other fuels, due to a nuclear resonance [Fre08]. Figure 1.1 shows the fusion rates of three different fuels as a function of temperature. The D-T reaction shows the largest reaction rate, which is reached at comparably low temperatures. Deuterium occurs naturally in large quantities in water, while tritium will have to be bred from lithium in the reactor [Fre08, Wes11].

1.2. Magnetic Confinement

The envisioned operating temperature for a fusion reactor utilizing reaction (1.1) is of the order of 10 keV [Wes11]. The fuel will then be heated by the alpha particles, which carry 1/5-th of the energy released from the reaction, and will be cooled by losses. When losses and alpha heating

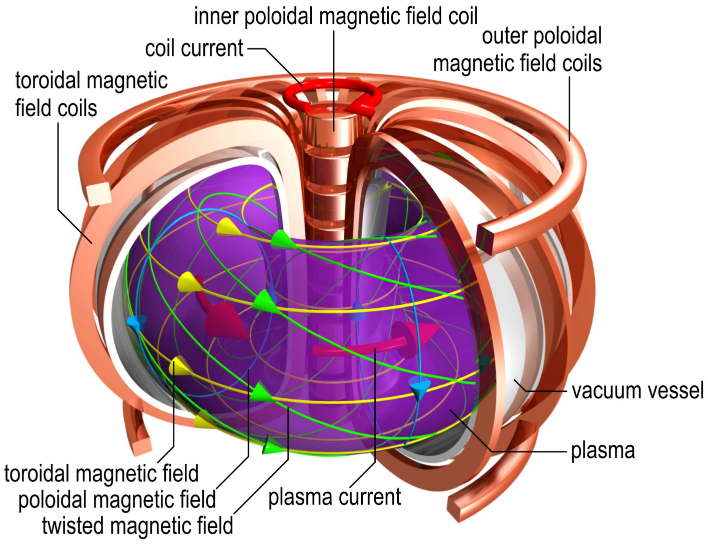

Figure 1.2.: Sketch of a Tokamak by Dr. Christian Brandt, IPP.

compensate each other, an ignition criterion can be formulated [Wes11]:

$$nT\tau_{\mathrm{E}} > 3 \times 10^{21}\,\mathrm{keV\,s\,m^{-3}}. \tag{1.2}$$

Here n and T are the plasma density and temperature, and τ_{E} the time in which the plasma would lose its energy without heating. The product $nT\tau_{\mathrm{E}}$ is called triple product.

Direct contact between the high-temperature plasma and a vessel would lead to high heat fluxes, strongly reducing τ_{E} and with it the triple product. To avoid this, one can utilize magnetic fields to isolate the charged constituents of the plasma from the reactor wall. A single charged particle in a (homogeneous) magnetic field gyrates around the magnetic field lines, preventing it from travelling further than one gyroradius in the direction normal to the magnetic field. Along the field line the particle can still escape any finite volume. However, one can confine the charged particle in a torus by bending the field lines. It is then necessary to twist the field lines to counteract so-called drifts, which are caused by the now inhomogeneous magnetic field and lead to movement perpendicular to the magnetic field. In a tokamak, the currently most successful device for magnetic confinement, this twisting is achieved by inducing a current parallel to the magnetic field. Figure 1.2 shows a sketch of a tokamak. The toroidal and outer poloidal magnetic field coils create the confining magnetic field; the inner poloidal field coilds, called the central solenoid, induces the plasma current; the vacuum vessel, among other functions, prevents the influx of air. The direction of the plasma current is called *toroidal*; the direction outwards from the red arrow depicting the plasma current is called *radial*. Perpendicular to both toroidal and radial is the *poloidal* direction.

Interactions between particles lead to nonzero heat and particle fluxes in radial direction. Collisions between particles lead to the comparably simple, but for heat and particle fluxes usually small neoclassical transport. Collective behavior of particles, together with the electromagnetic fields they create and interact with, lead to plasma turbulence and large scale magnetohydrodynamical instabilities which are the main cause of heat and particle fluxes in a tokamak fusion plasma. The transport processes resulting in the fluxes determine the density and temperature of the plasma as a function of radius, together with the radius dependent heat and particle input. A quantity such as temperature or density as function of radius is called the profile of said quantity. [Fre08, Wes11]

1.3. Role of the Plasma Edge

Understanding the transport processes in the edge is an important building block for designing future machines and predicting their performance [Lud20, Sny11]. Edge and core regions of the plasma are coupled through the transport mechanisms outlined in the previous sections. While the core plasma properties determine the fusion performance, the colder plasma edge is crucial in setting the core plasma's parameters. An illustrative example of the influence of the plasma edge on the core plasma is the so-called H-mode [Wag07]: when sufficient power flows through the edge plasma, turbulence is strongly suppressed due to sheared flows. The reduced transport in the edge leads to an accumulation of energy in the core, improving fusion performance considerably. The plasma edge in a reactor also has tasks on its own, besides providing beneficial boundary conditions for the core plasma. An example is the dissipation of heat to avoid damage to the first wall [Kal13, Zoh13].

Determining the heat transport in the edge of nowadays machines is comparably straight forward: heat transport can be described by diffusion [Per02]. Therefore, the transport coefficients can be determined directly with the heat input, the local density and the temperature gradients. Particle transport on the other hand is known to have convective contributions in addition to diffusion [Tal19]. Furthermore the particle source, which arises when neutral atoms from fuelling and the wall are ionized, is only poorly known. Measuring the steady state density profile is therefore not enough for understanding particle transport. As a result particle transport, particularly at the edge, is not understood sufficiently.

The edge density profile directly influences important quantities such as the power needed to achieve H-mode [Sha16] or the attainable pressure in the edge region [Dun16]. In the past, modulation experiments [Sal15] have been performed and naturally transient plasma states [Wil13] have been investigated to identify diffusive and convective contributions to the particle transport. The nature of particle transport at the edge however still remains an open question. The lack of understanding leads to strongly different predictions for the edge density profile in future machines [Rom15, Mor20], leaving many questions about the properties of future machines unanswered.

1.4. Aim of this Work

As in previous particle transport studies [Sal15, Gen92, Kop00, Tal19] the *fuelling* particle flux, i.e. the particle flux of neutral deuterium gas entering the vacuum vessel, is modulated to cause a perturbation of the plasma. It is investigated how the edge density is building up due to the additional fuelling, and the density evolution is interpreted to understand how the underlying processes cause these changes. Other than in previous work, not only the density is considered, but also the temperature measurements of the plasma. This allows the investigation of the connection between heat and particle transport, and heat transport itself.

To approach these questions the work is arranged in the following outline:

In **Concepts of Transport Analysis in Tokamaks** the principles, effects and methods required for the study are discussed. Also the existing research relating to the questions under consideration is described.

The approach followed in this work relies on the measurements of various plasma quantities. In the chapter on **Diagnostics** the working principle and limitations of the key measurement devices, on which the obtained results depend, is described.

Experimental Design, Analysis Method and Case Study describes and motivates the experimental setup for the conducted plasma discharges. The model used for the interpretation of the experimental data is developed. Finally, results for an L-mode discharge as case study are shown and discussed as case study.

In the chapter **Particle and Heat Transport in the Edge of Tokamak Plasmas** the analysis is extended to more scenarios.

The thereafter following **Discussion** assesses strengths and limitations of the developed method, and encompasses the results presented in the previous chapters.

Summary and Outlook gives a concise description of the taken approach, collect the main results, and gives an outlook to future work.

2. Concepts of Transport Analysis in Tokamaks

This chapter discusses the concepts underlying the experiments, analysis and interpretation presented in this thesis.

2.1. Tokamak Geometry

Section 1.2 introduced the tokamak principle in figure 1.2. Here the focus is on the geometry of the confining magnetic field, which determines the geometry of the plasma, and the transport processes within.

Because the toroidal magnetic field is stronger close to inner poloidal coils the portion of a flux surface close to the central solenoid is said to be on the high field side (HFS), while the outer portion is said to be on the low field side (LFS).

The currents flowing in the plasma twist the magnetic field lines created by the toroidal field coils with their induced magnetic field. To sustain pressure gradients it is necessary for field lines to form surfaces [Wes11], shown in figure 2.1. The solid blue line is the last closed flux surface, or separatrix. Particles on a flux surface can move freely and transport heat very efficiently. The pressure is therefore constant on each flux surface, and also the electron and ion temperatures and the density can be approximated to be only dependent on which flux surface they are on for many applications [Fre08, Wes11]. The innermost surface which collapses to a line is called magnetic axis (cross in figure 2.1). The magnetic axis lies on a plane. The magnetic flux through this plane, as a function of distance to the symmetry axis, is called poloidal flux [Zoh15]. The ratio of toroidal turns to poloidal turns when following a field line is q, the safety factor.

The size of the plasma is given by the distance of the magnetic axis to the symmetry axis and is called major radius R, and the radius of the plasma cross section called minor radius a (red arrows in figure 2.1). R/a is called aspect ratio. The poloidal field coils modify the shape of the plasma: the shape is characterized by the elongation or ellipticity κ and the triangularity δ, which specifies how pointed and how much inward the upper and lower corners of the last closed flux surface are.

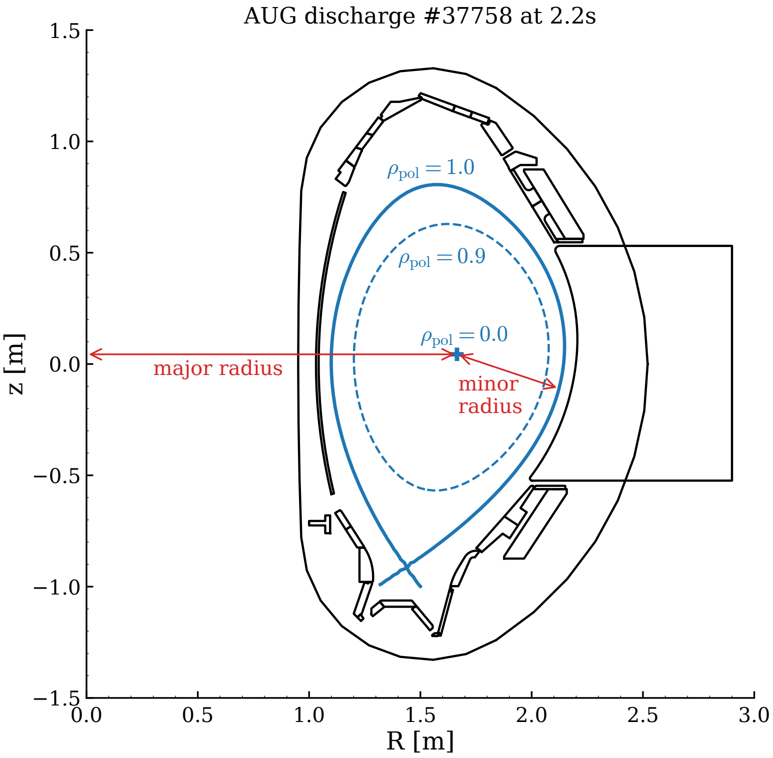

Figure 2.1.: Poloidal cross section of the ASDEX Upgrade tokamak for discharge #37758 at 2.2 s, with the separatrix at $\rho_{\mathrm{pol}} = 1.0$ and the magnetic axis at $\rho_{\mathrm{pol}} = 0.0$. The red arrows show the major and minor radii of the torus-shaped plasma.

In the core plasma all flux surfaces are closed, i.e. encompass finite volume and do not intersect wall components. Using poloidal field coils it is possible to open the outer flux surfaces. Here the particles and the residual power that were transported radially outward contact the material wall in a structure called divertor. The last closed flux surface (LCFS) is called separatrix (blue solid line in figure 2.1. The poloidal flux is normalized to be 0 on the magnetic axis and 1 at the separatrix, and take the square root to obtain the important radial coordinate ρ_{pol}. The plasma outside of the separatrix forms the scrape-off-layer (SOL).

2.2. Description of Transport

After the previous description of the geometry in which transport takes place this section discusses how transport of particles and heat between flux surfaces is described. Parts of this explanation have been published already [Sch22].

Both turbulence, which shows chaotic behavior, and collisions can be described statistically. The upcoming transport equations can be understood with a simple picture: a particle or heat quantum is transported to adjacent flux surfaces according to a probability distribution. If the turbulent structures are small then the particle or heat quantum undergoes many jumps to traverse a macroscopic distance. The travelled distance is then the sum of many jumps of random distance. The central limit theorem then dictates that the travelled distance follows a Gaussian distribution with only two parameters: standard deviation which corresponds to diffusion, and a mean distance which corresponds to convection. An inward convection is called pinch.

It is not certain how large the turbulent structures causing transport are close to the separatrix. But their statistics are still Gaussian [Boe03, Nol10], resulting in diffusive-convective transport on the time scales of interest for this work [Nau07].

Further outside in the SOL the structures are larger and occur intermittently [D'i11, Via19], but on the comparably long time scales investigated in this thesis one can still describe the resulting transport as diffusive [Man20].

The diffusive-convective nature of transport results in the following transport equations:

$$\frac{\partial n_\mathrm{e}}{\partial t} = \frac{\partial}{\partial \rho}\left(D\frac{\partial n_\mathrm{e}}{\partial \rho} - v n_\mathrm{e}\right) + S_\mathrm{e} \tag{2.1}$$

$$\frac{3}{2}\frac{\partial\left(n_\mathrm{e}T_\mathrm{e}\right)}{\partial t} = \frac{\partial}{\partial \rho}\left(n_\mathrm{e}\chi_\mathrm{e}\frac{\partial T_\mathrm{e}}{\partial \rho}\right) + P_\mathrm{e} \tag{2.2}$$

$$\frac{3}{2}\frac{\partial\left(n_\mathrm{i}T_\mathrm{i}\right)}{\partial t} = \frac{\partial}{\partial \rho}\left(n_\mathrm{i}\chi_\mathrm{i}\frac{\partial T_\mathrm{i}}{\partial \rho}\right) + P_\mathrm{i}, \tag{2.3}$$

where geometrical factors are omitted which are given elsewhere [Per02]. n_e is the electron density, $n_\mathrm{i} \approx n_\mathrm{e}\left(Z_\mathrm{i} - Z_\mathrm{eff}\right)/\left(Z_\mathrm{i} - 1\right)$ the ion density with $Z_\mathrm{eff} = 1.2$, ρ the normalized flux coordinate, S_e the electron particle source, P_e the power density heating the electrons, and P_i the power density heating the ions. The interaction between neutral atoms and the plasma, which is treated in the next section, occurs through S_e, P_e and P_i. The heat diffusivities χ_e and χ_i are effective diffusivities, which include convective contributions from the finite particle flux

Before continuing with the neutral particles in the torus and their interaction with the plasma, some more words will be spent on the nature of transport in the edge of tokamak plasmas.

2.3. Turbulence and Edge Transport Regimes

Turbulence, which is responsible for the largest contribution of transport in most situations, can be pictured as follows: in the plasma small perturbations in density, temperature and other quantities grow exponentially until they saturate nonlinearly. This is an intuitive description that fails in some cases [Jen00a, VW16], but can be used successfully in many situations [Sta07, Cit17].

The growth of the small initial perturbations is due to various instabilities of the plasma. Kotschenreuther et al. [Kot19] give an overview of the instabilities and modes a plasma can exhibit. The growth rates of the instabilities depend on various quantities such as the temperature, density and pressure gradients. A dependency that is investigated in this work is collisionality

$$\nu^* = 6.921 \times 10^{-18}\,\mathrm{m}^3\,\mathrm{eV}^2 \frac{R q n_\mathrm{e} Z_\mathrm{eff} \ln \Lambda_\mathrm{e}}{\epsilon^{3/2} T_\mathrm{e}^2}, \tag{2.4}$$

where R is the major radius, q the safety factor, Z_eff the effective ion charge, $\ln \Lambda_\mathrm{e}$ the Coulomb logarithm, and $\epsilon = a/R$ the inverse aspect ratio [Oya06]. Several theoretical works predict stronger turbulent transport in the edge at higher collisionalities [Bon19, Bou12, Rog98, Sco07].

The plasma edge greatly influences the general plasma performance. Based on transport properties one distinguishes between different operational modes of a tokamak plasma.

2.3.1. L-Mode

If only low heating power is injected in nowadays tokamaks, the plasma tends to be in the low confinement mode, or L-mode. Strong turbulence transports heat and particles across the separatrix into the so-called Scrape-Off-Layer (SOL). Because of the strong transport the power entering the SOL spreads across a comparably large radial distance in the SOL: on the one hand the 'power fall off length' λ_q is large, resulting in low power densities in the divertor. On the other hand the large transport leads to low energy confinement times τ_E. Increasing the heating power initially leads to stronger turbulence, reducing τ_E.

2.3.2. H-Mode

In 1982 Wagner et al. made a surprising discovery: increasing the heating power above a threshold leads to a sudden increase in τ_E [Wag82]. 40 years after the initial discovery a predictive model is still not available, but understanding has improved considerably [Wag07]. In H-mode the edge turbulence between $\rho_\mathrm{pol} = 0.97$ and the separatrix is reduced strongly. Shear flows can suppress turbulence [Big90, Cav16], and together with other stabilizing effects one can understand why a particular plasma is in L- or H-mode [Eic21].

In H-mode the edge (temperature) gradients have to be much steeper than in L-mode to transport all the power injected into the plasma despite the reduced transport coefficients χ_e and χ_i (see equations (2.2) and (2.3)). The steep gradient region is referred to as pedestal because it raises the core profiles as if they would sit on a pedestal. Besides improving the fusion performance the steep gradients lead to instabilities called edge localized modes which are discussed in the next section. The reduced transport also leads to an uncomfortably small λ_q [Eic13].

2.3.3. Edge Localized Modes (ELMs) and their Avoidance

After the plasma enters H-mode the reduced transport leads to a steepening of the temperature and densities profiles, and therefore the pressure profile. The steep gradient region becomes wider, until ideal magnetohydrodynamical (MHD) modes become unstable [Cav17]. These instabilities only saturate nonlinearly after they reached a large amplitude, unlike the instabilities responsible for turbulence. The growing edge localized mode (ELM) ejects heat and particles into the SOL resulting in large heat loads in the divertor. After the ELM the gradients are flattened and increase again until the plasma becomes unstable once more and the next ELM occurs, or 'crashes'. The large instabilities described here are referred to as type-I ELMs [Zoh96].

The transient heat loads caused by the ELMs are too extreme for the divertor in a reactor [Loa14]. Because of the good confinement properties of H-mode one would nevertheless like to operate a reactor in H-mode and not L-mode. Instead, different operational regimes are developed where additional transport hinders the plasma from becoming unstable with respect to type-I ELMs. A variety of approaches are investigated at the moment, for example the perturbation of the plasma with nonaxisymmetrical magnetic fields [Eva05, Sut11] or the operation in configurations with naturally enhanced transport [Gil20, Gre99, Har22, Vie18]. The only type-I ELM free regime investigated in this work is the QCE regime [Har22, Rad22] because it is compatible with comparably high densities and is resilient to the injection of neutral gas into the torus, called fuelling. In the quasi-continuous exhaust (QCE) regime, which exists at high triangularity δ and density, small ELMs become unstable in a narrow region just inside the separatrix and cause sufficient transport to avoid large type-I ELMs [Rad22].

2.4. Neutral Particles and their Influence on the Plasma

Ions which reach the wall due to transport processes are neutralized. The resulting atom can stick to the wall, be pumped from the torus or might re-enter the plasma, a process that is called recycling. The focus here is on hydrogen isotopes, which constitute the main ions in both fusion plasmas and most nonnuclear plasmas.

Together with injected fuel the recycled hydrogen forms a population of neutral atoms and molecules in the edge region of the plasma. Unhindered by the magnetic field they move across flux surfaces. Hydrogen molecules are dissociated by electron impact, a process which results in characteristic kinetic energies of the emerging neutral atoms between $2\,\mathrm{eV}$ and $5\,\mathrm{eV}$ known as Franck-Condon neutrals.

One of the two most important processes involving the neutral atoms are charge exchange reactions. A neutral atom colliding with an ion can transfer its electron to the ion, which is equivalent to the neutral atom and the ion switching their momentum vectors. As the ion temperature is usually higher than the neutral energy, this results in an acceleration of the neutral population. The effective energy loss of the plasma is contained in the power term P_i in equation (2.3).

The second process is electron impact ionization. After ionization of an atom both the electron and the ion are confined to the local flux surface and contribute to the local plasma density, which is expressed through the particle source term S_e in (2.1). Most atoms are ionized in the edge region of the plasma. Ionization of a hydrogen atom in ground state requires 13.6 eV, an energy that the impacting electron provides. The resulting power loss in the electron channel is included in the power term P_e in equation (2.2).

The neutral population is not solely composed of fuelled and recycled neutrals. Energetic neutral atoms, created in particle accellerators, can cross the separatrix and are used for heating the plasma (neutral beam injection, abbreviated as NBI). They present a particle source when ionized, but the recycling and fuelling neutrals are dominant in the edge region. Neutral atoms do also not necessarily cross the separatrix as individual neutral atoms: by injecting pellets of frozen hydrogen one can create a particle source located inside the core plasma.

In a future reactor the particle source will behave differently than in nowadays experiments. The plasma in the SOL strongly affects the neutral dynamics and with it the distribution function of neutrals reaching the separatrix: in the International Thermonuclear Experimental Reactor (ITER) less than 2 % of the total recycling flux are expected to reach the core plasma [Loa15, Rom15].

2.5. The Density Profile in the Pedestal Region and the Modulation Technique

The density profile depends both on particle transport and on the particle source. Figure 2.2 shows the density profiles of three different discharges in the AUG tokamak which are representative for the three different regimes investigated in this work. All scenarios show a peaked density profile, meaning that the core density is higher than the edge density at e.g. $\rho_\mathrm{pol} = 0.8$. Because the particle source is located at the edge this peaking has to be due to a particle pinch [Str99, Tal19]. At the plasma edge, outside of $\rho_\mathrm{pol} = 0.95$, the density gradient is far larger than in the core plasma. For the L-mode and ELMy H-mode in figure 2.2 the density decays quickly to 0 outside the separatrix, but the QCE discharge shows a phenomenon known as density shoulder.

This work focuses on the steep gradient region just inside the separatrix. The density profile is a result of both particle source and transport, with diffusive and possibly convective contributions. A simple one dimensional model can already reproduce the general shape of the edge density profile in nowadays tokamaks [Mah02, Gro02]: particle transport is assumed to be purely diffusive. Neutral particles cross the separatrix at one poloidal position and are ionized by the plasma.

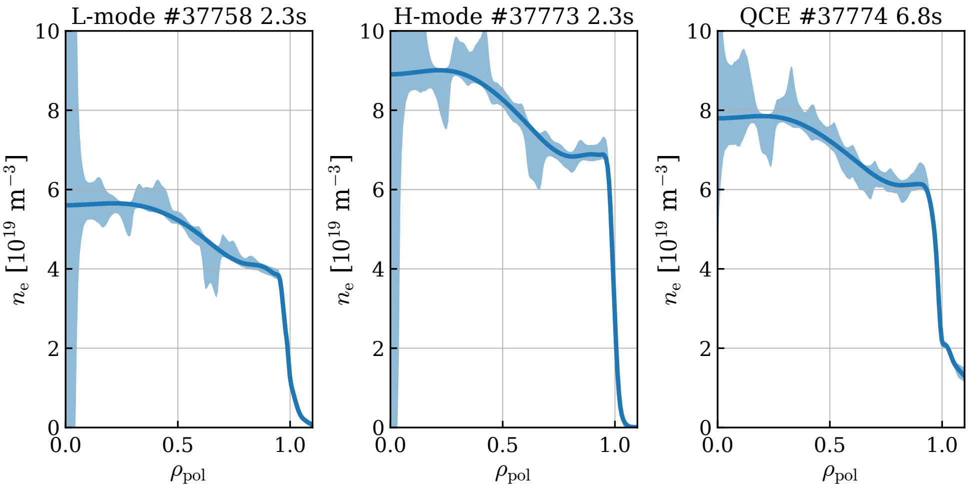

Figure 2.2.: Density profiles of three different AUG discharges with error bars. The profiles are reconstructed by the IDA framework [Fis10].

The resulting particle source is located in a narrow region inside of the separatrix. Diffusive outflux, which is proportional to the density gradient, has to balance the influx of neutrals. Just inside the separatrix, at flux surfaces which many neutrals pass, a large density gradient provides sufficient diffusive outflux. Moving inward the gradient becomes flatter as less and less neutrals penetrate sufficiently deep. Solving the nonlinear equation for n_e yields a hyperbolic tangent, matching the shape of experimental edge density profiles, [Mah02, Gro02].

The predictions of the analytical model agree with many experiments: at higher density, neutrals are ionized in a narrower region, leading to a narrower steep gradient region [Gro02, Kir04]. A higher density also coincides with an outward shift of the density profile [Beu11, Ste18]. Simultaneously, the simple model has several shortcomings that result in discrepancies with experiments: Wang et al. [Wan18] found deviations from the predicted width scaling, Hughes et al. [Hug07] found density profiles mostly invariant against fuelling changes, and Dunne et al. [Dun16] found effects that are not contained in the model which shift the density pedestal. A more sophisticated treatment of the neutrals and fuelling [Rei17] is necessary, but cannot resolve all disagreements [Rek21]. The big unknown is transport: a pinch would react differently to altered fuelling changes than diffusion alone. And there is evidence that transport changes when fuelling is increased [Hug07, Rek21, Mac21]. The lack of understanding leads to large uncertainties when considering future machines [Mor20, Rom15].

The steady state profiles do not contain sufficient information to understand the determining effects of the density profile. First, consider the core plasma, where the particle source is often of minor importance and can be quantified accurately [Tal19]. From equation (2.1) it follows that, without particle source and in steady state, the ratio of v and D determines the density gradient. In steady state it is therefore only possible to determine the ratio of v and D and not their individual values. But the temporal evolution of the density depends also on the absolute values of D and v allowing to determine them [Tal19]. Such transient states can be created by modulating the fuelling gas flux [Nag93], a technique known as gas-puff modulation.

In the pedestal region the fast timescales, small spatial scales and a particle source which is notoriously hard to quantify make it difficult to gain understanding similar to transport in the core region. Nevertheless results have been obtained: Willensdorfer et al. [Wil13] analyzed the density build-up after transitioning from L-mode to H-mode. Best agreement was found with $D = 0.031\,\mathrm{m^2\,s^{-1}}$ and $v = -0.5\,\mathrm{m\,s^{-1}}$, but a pinch up to $-5\,\mathrm{m\,s^{-1}}$ is possible. Also without a pinch good agreement between model and experiment could be reached. Salmi et al. [Sal15] considered gas-puff modulation experiments at the JET tokamak [Jof19]. They found particle diffusivities just inside the separatrix of the order of several $0.1\,\mathrm{m^2\,s^{-1}}$ and an inward pinch for the considered H-mode plasma.

In this work gas puff modulation experiments are performed at the ASDEX Upgrade tokamak and the plasma response is modelled, simultaneously considering plasma density and temperatures. It is found that the fuelling modulation strongly alters heat and particle transport, adding another complexity to the problem. Nevertheless it is possible to draw conclusions about particle transport, among other results. Before the discussion of these experiments and the developed methods in chapters 4 and 5 the utilized measurement methods are introduced in chapter 3.

3. Diagnostics

This chapter discusses the principles and limitations of the key measurement methods used in the experimental studies. For the conducted transport analysis these are the plasma density and temperatures inside the separatrix.

3.1. Interferometry

Interferometry allows to obtain very accurate electron density measurements with high temporal resolution, albeit with poor spatial resolution.

An electromagnetic wave with a vacuum wavelength λ, and a frequency much higher than the plasma frequency ω_{pl} [Wes11]:

$$\omega_{\mathrm{pl}} = \sqrt{\frac{n_{\mathrm{e}} e^2}{\epsilon_0 m_{\mathrm{e}}}}, \tag{3.1}$$

that traverses a plasma along a path l experiences a phase shift of $\Delta\phi$

$$\Delta\phi = \lambda \frac{e^2}{4\pi\epsilon_0 m_{\mathrm{e}} c^2} \int_l n_{\mathrm{e}} \, \mathrm{d}l, \tag{3.2}$$

as given by Wesson [Wes11]. e is the charge of an electron, ϵ_0 the permittivity of vacuum, c the speed of light in vacuum, and m_{e} the mass of an electron in its rest frame.

This effect offers an opportunity for a robust and accurate diagnostic of the electron density in magnetic confinement plasmas, as described by Mlynek et al. [Mly10]: the phase shift of a laser beam, which traverses the plasma, is proportional to the line averaged density. Based on this principle a Mach-Zehnder-type interferometer with a deuterium cyanide (DCN) laser is used as density diagnostic in the ASDEX Upgrade Tomakak. Some spatial resolution is recovered by using five individual laser beams, differing in geometry, that traverse the plasma. [Mly10]

Figure 3.1 shows the geometry of the interferometry system. Depending on the path of the laser beam the integration in equation 3.2 has contributions from most radii (H-0 and H-1) or only

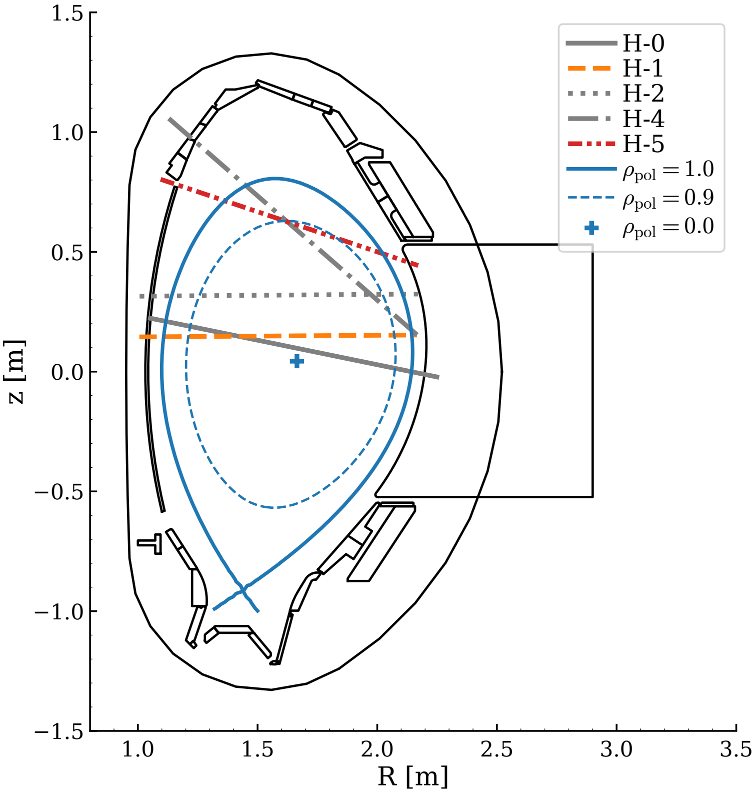

Figure 3.1.: Poloidal projection of ASDEX Upgrade showing the geometry of the different DCN interferometry channels. The channels H-1 (orange) and H-5 (red) are emphasised. Also shown are flux surfaces and the magnetic axis in blue.

from the edge (H-5). The channels H-1 (orange) and H-5 (red) will be shown more often than other channels in this dissertation, motivating their highlighting in figure 3.1.

3.2. Lithium Beam

Atomic emissions from within a plasma offer an opportunity for spatially and temporally well resolved measurements [Wol93, Gri18, McD18]. The first discussed diagnostic of this type is the lithium beam operated at ASDEX Upgrade [Wil14, Fis08].

The diagnostic, which is described in Willensdorfer et al. [Wil14], consists of two subsystems: the apparatus creating the beam of neutral lithium atoms that enter the plasma, and the spectroscopy system responsible for recording the emissions of said lithium atoms. The beam is formed outside of the main vacuum vessel of the tokamak. Lithium ions are emitted from a source [McC97] and accelerated to 35–60 keV. After the acceleration the ions pass through a sodium vapor chamber where most ions are neutralized [McC97]. The neutralized lithium atoms subsequently enter the main vessel, undisturbed by the present magnetic fields, and collide with plasma particles. Lithium atoms are excited, mostly by electron impact, a process whose rate depends only weakly on the electron temperature but strongly on the electron density [Wol93]. Photons emitted from de-excitation are collected by an optical system, the wavelengths of the 2p-2s transition of lithium are selected by a band-pass filter, and digitalized. [Wil14]

Fischer et al. [Fis08] describe how the edge density is reconstructed from the emissions: lithium atoms with several 10 keV travel a non negligible distance in the time between excitation and de-excitation [Wol93]. Additionally lithium atoms are not only excited but also ionized, leading to a decreasing beam intensity for the lines of sight further inside the plasma. The emitted light is therefore not a function of the local density but a functional of the density along the beam. The local density is reconstructed by comparing the measured emissions to a forward model and applying Bayesian inference. Because of ionization the signal-to-noise ratio decreases the further the atoms have to penetrate. The use of this diagnostic is therefore restricted to the edge region, with the minimal radius which is still covered depending on the required accuracy and the plasma discharge. [Fis08]

3.3. Thermal Helium Beam and Fast Piezo Valves

The thermal helium beam diagnostic is related to the lithium beam diagnostic, but differs in several important aspects. The system and its principle are described in Griener et al. [Gri17a]. First of all, the helium atoms are injected as gas at room temperature and not accellerated. Secondly, the intensities of four different atomic transitions are individually measured. The intensities of the transitions depend differently on the electron temperature and density. Other than with the lithium beam diagnostic at AUG it is therefore possible to estimate the electron temperature and density. The most accurate results are obtained with a collisional-radiative model and Bayesian inference [Wen22].

The gas puff modulation experiments utilize a valve of the same type as the one used to inject the diagnostic helium. The design, function and properties thereof are therefore described in more detail, following Griener et al. [Gri17b]. In between plasma discharges a reservoir inside the vacuum vessel is filled with the gas of choice up to the set pressure. The gas can exit the reservoir and enter the SOL through a capillary, which is only 66 mm long. In between shots and when no gas shall enter the SOL, the entry of the capillary is sealed with a Viton plate. For opening the valve the Viton plate is lifted by a piezo actuator located inside the reservoir. The short capillary and the fast piezo actuator result in fast transitions between zero and full flow of less than 1 ms, [Gri17b].

3.4. Electron Cyclotron Emission Spectroscopy (ECE)

ECE offers temporally and spatially well resolved electron temperature measurements in the core plasma. Other than with the previous diagnostics it is sufficient to monitor emissions of the plasma itself, without the need of diagnostic atoms or photons, [Wes11].

Here a short introduction to the diagnostic principle is given, details and sources can be found in Wesson [Wes11]. Electrons in a magnetic field gyrate with the gyrofrequency

$$\omega_\mathrm{c} = \frac{|e|\,B}{m_\mathrm{e}}, \tag{3.3}$$

with B being the magnetic field. In a tokamak ω_c is of the order of 100 GHz. Due to this accelerated motion of the electrons in the plasma, electromagnetic radiation of the same frequency is emitted, i.e. cyclotron emissions. Adjacent electrons, which gyrate with the same frequency, can reabsorb this radiation. With sufficient reabsorption the intensity of the cyclotron radiation directly corresponds to the electron temperature T_e. The relevant criterion for this is $\tau \gtrsim 1$ with the optical depth $\tau \propto T_\mathrm{e} n_\mathrm{e}$ [Sut96]. At the frequencies and magnetic fields in question the radiation intensity then follows the Reyleigh-Jeans law

$$I\left(\omega_\mathrm{c}\right) = \frac{\omega_\mathrm{c}^2 T_\mathrm{e}}{8\pi^3 c^2} \tag{3.4}$$

with c being the speed of light. Note that a plasma volume with uniform ω_c does not radiate in the full spectrum but only at ω_c, with the intensity given by Eq. 3.4.

The magnetic field in a tokamak is approximately proportional to the inverse major radius:

$$B \underset{\sim}{\propto} \frac{1}{R}. \tag{3.5}$$

As $\omega_c \propto B$ also the gyrofrequency is a known function of R. The ECE diagnostic collects the emissions along a line of sight and determines the energy spectrum thereof. Each frequency corresponds to a position, and the intensity at this frequency to the local electron temperature.

3.5. Charge Exchange Recombination Spectroscopy (CXRS)

Ion temperatures are routinely measured using a technique called charge exchange recombination spectroscopy (CXRS). A general overview is given by Wesson [Wes11]. The system at AUG is described by McDermott [McD18], where also the underlying physical processes are described in more detail. For heating of the plasma a neutral deuterium beam is injected into the torus (NBI). Electrons of beam atoms are transferred to impurity ions in so-called charge exchange reactions. The receiving atoms are in an excited state after the reaction, and they will spontaneously decay. The emitted photons are coupled into glass fibers and analyzed in a spectrometer. The temperature of the impurity ions results in Doppler broadening of the de-excitation line, allowing the determination of the temperature from the measurements. Main and impurity ions equilibrate on shorter time scales than ions and electrons because their masses are more similar. In practice, it is therefore often justified to equate the impurity and main ion temperatures. At AUG there are lines of sight both for the core and edge regions. Because the diagnostic relies on NBI neutrals, measurements are only available if the plasma is heated by NBI, [McD18].

3.6. Neutral Particle Analyzer (NPA)

At one location at the outer midplane, neutral particles leaving the plasma from a single direction are collected by a neutral particle analyzer. The energy spectrum of is determined with a setup similar to a mass spectrometer [Bar87]: the neutral atoms are ionized, after which they are deflected by a magnetic field perpendicular to the incident atoms. The radius of the gyromotion is proportional to the velocity of the atoms. Detectors at different positions then count the energy-resolved particles. Deuterium atoms are selected by applying an electric field perpendicular to both the incident particles and the magnetic field. The resulting deflection in the direction of the electric field depends on the ratio of mass and electric charge. Using the plasma density and temperatures it is then possible to infer the neutral density profile [Bog21].

Because the neutral density profile is reconstructed along one line of sight, and not averaged on the respective flux surfaces, it cannot be used directly for interpreting the density response. Data from the NPA diagnostic is therefore excluded for the major part of the presented analysis.

4. Experimental Design, Analysis Method and Case Study

This dissertation is based on experiments conducted by the author, and integrated modelling developed by the author. In this chapter one single discharge is discussed, both to obtain results about the physics governing the plasma behavior and to discuss the developed and used analysis method. The analysis will be expanded to more discharges in the next chapter, which draws more general conclusions.

The chapter starts with a description of the chosen experimental setup. Thereafter the behavior of the plasma density, plasma temperature and of the neutral atoms will be discussed. Section 4.2 develops the analysis method used to reach the results. After a high-level overview of the workflow the modelling of the plasma response, and how the model is used to infer physical quantities from the experimental data, is discussed in detail. Starting in section 4.3 results are shown and conclusions drawn. Unless stated otherwise the contents of this chapter have been published in Nuclear Fusion [Sch22].

4.1. Experimental Setup and Measurements

For the transport analysis the plasma is perturbed by modulating the gas flow into the vacuum vessel utilizing fast acting valves [Gri17b]. Transitioning from zero to full fuelling takes less than 1 ms. The fuelling rate is 8×10^{21} deuterium atoms per second ($120\,\mathrm{Torr\,L\,s^{-1}}$) with a modulation frequency of 25 Hz, giving a modulation period of 40 ms. The valve, which was characterized by Griener et al. [Gri17b], is located at the outer midplane.

The modulation period of 40 ms is chosen because it is long enough such that the plasma at the separatrix reaches steady state for the open and closed state, which is beneficial for the interpretation of the data. Making it even longer would reduce the number of periods one can average over, resulting in less clear data.

For small perturbations the response will be linear with respect to the perturbation, but too large perturbations will eventually cause a nonlinear disturbance. A nonlinear answer is more difficult to interpret and further distant to the nominal operation parameters, suggesting to

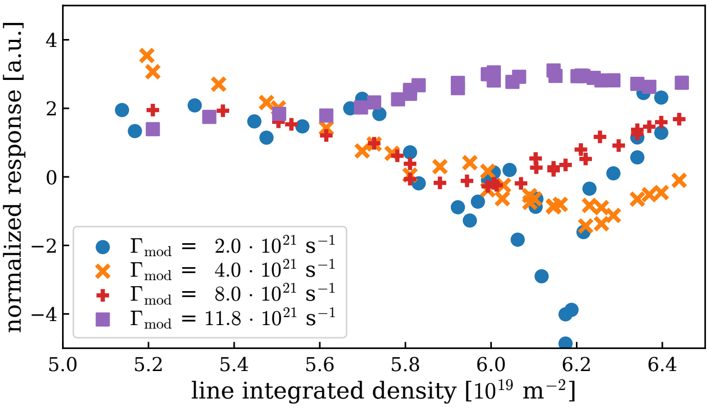

Figure 4.1.: The normalized response, i.e. the steady state change in density at $\rho_{\text{pol}} = 0.99$ from the Lithium beam diagnostic when opening the valve divided by the modulating fuelling flow, against the line averaged electron density as measured by the core interferometry channel H-1. Four discharges, which utilize different deuterium fluxes for the modulation, are shown: $2 \times 10^{21}\,\text{s}^{-1}$ (#37018), $4 \times 10^{21}\,\text{s}^{-1}$ (#37017), $8 \times 10^{21}\,\text{s}^{-1}$ (#37019), $11.2 \times 10^{21}\,\text{s}^{-1}$ (#37020). Each point corresponds to one modulation period.

aim for a modulation amplitude in the linear regime. Simultaneously, one wants to select the particle flux used for the modulation as large as possible because a stronger response is less influenced by experimental noise. To determine this maximal modulating particle flux four discharges were carried out, each with a different perturbation amplitude. It is not productive to take the same setup, use different modulating particle fluxes, and compare the results: The different average fuelling particle flux leads to different background densities and different plasma conditions. Instead, a background fuelling flux is added to the discharges which increases from 0 to $10 \times 10^{21}\,\text{s}^{-1}$ over a time span of 3.5 s. To judge whether the response of the plasma is linear, identical densities are compared, and not e.g. time points. Except for the fuelling the setup is identical to #37758, the discharge analyzed in this chapter.

In figure 4.1 the density change, divided by the fuelling particle flux, at $\rho_{\text{pol}} = 0.99$ is shown as a function of density for the four different cases as measured by the Lithium beam when switching from the closed valve state to the open valve state. If the response of the plasma was linear then the points should collapse to the same curve because a larger response is normalized to an equally larger perturbation. For the three cases with smaller fuelling flux (blue circles for $2 \times 10^{21}\,\text{s}^{-1}$, orange crosses for $4 \times 10^{21}\,\text{s}^{-1}$, and red pluses for $8 \times 10^{21}\,\text{s}^{-1}$), the normalized response decreases with increasing density between $5.2 \times 10^{19}\,\text{m}^{-3}$ and $5.8 \times 10^{19}\,\text{m}^{-3}$, and increases between $6.2 \times 10^{19}\,\text{m}^{-3}$ and $6.5 \times 10^{19}\,\text{m}^{-3}$. Apart from experimental noise there are systematic differences visible, but they are much smaller than the differences between the three lower fuelling cases and the highest fuelling case with a fuelling flux of $11.8 \times 10^{21}\,\text{s}^{-1}$ (purple squares). For this last case the trends are reversed.

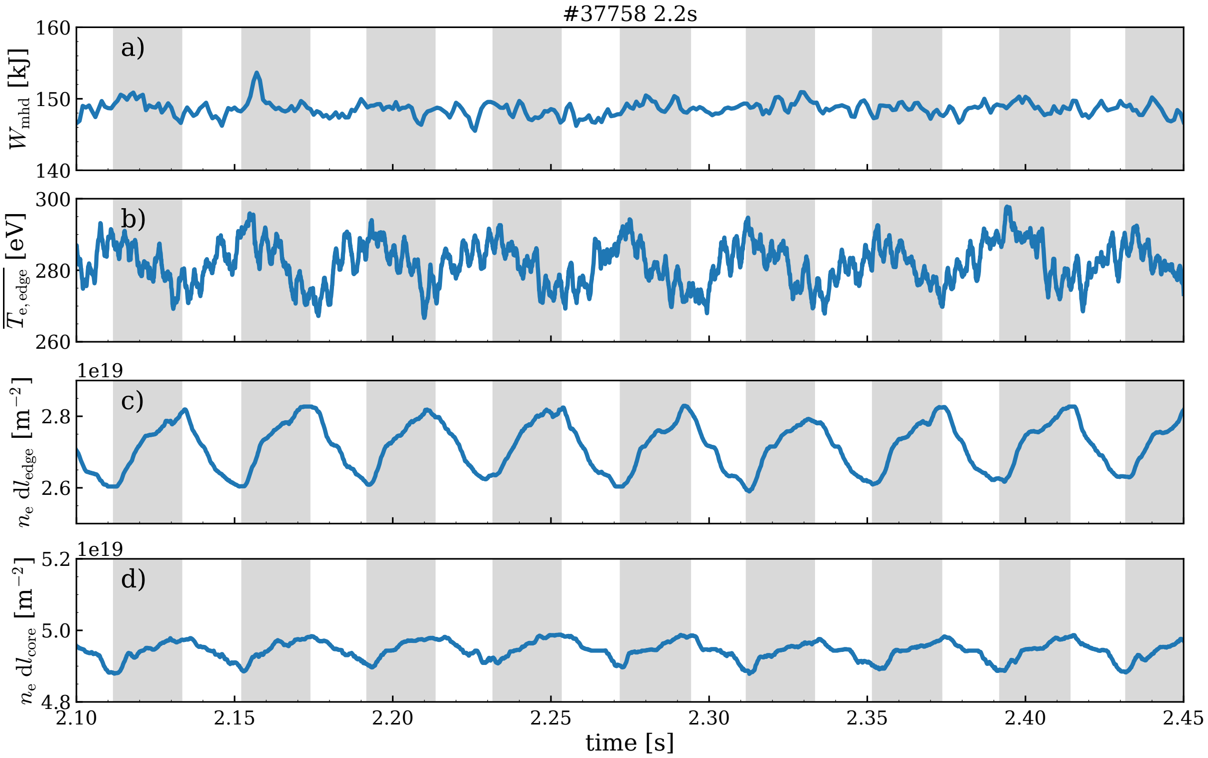

Figure 4.2.: Overview of the discharge segment under investigation. The fuelling valve is open in the grey shaded intervals, and closed in the unshaded intervals. The figure shows the stored energy (a), the average electron temperature as measured by ECE channels between $\rho_{\mathrm{pol}} = 0.8$ and $\rho_{\mathrm{pol}} = 0.9$ (b), and the line integrated density from the interferometry edge channel H5 (c) and the core channel H1 (d).

In the following, the fuelling flux is selected as $8 \times 10^{21}\,\mathrm{s}^{-1}$ because it is the largest flux that still shows a linear response.

All experimental data is from L-mode discharge #37758 in the tokamak ASDEX Upgrade (AUG) with a plasma current of $I_{\mathrm{P}} = 0.8\,\mathrm{MA}$ and a toroidal magnetic field of $B_{\mathrm{t}} = -2.4\,\mathrm{T}$. Central electron cyclotron resonance heating (ECRH) of 590 kW is applied in addition to Ohmic heating of 440 kW, while the radiation losses are about 200 kW [Dav21]. Figure 4.2 shows selected quantities for the discharge under investigation. The stored energy W_{mhd} (figure 4.2a) remains constant except for experimental noise, while the electron temperature (figure 4.2b) and the line integrated electron density (figures 4.2c and 4.2d) oscillate with the fuelling modulation around a constant background. In the following the measured modulation is investigated in detail. The data is averaged over the nine modulation periods to obtain a more accurate mean response and the standard deviation.

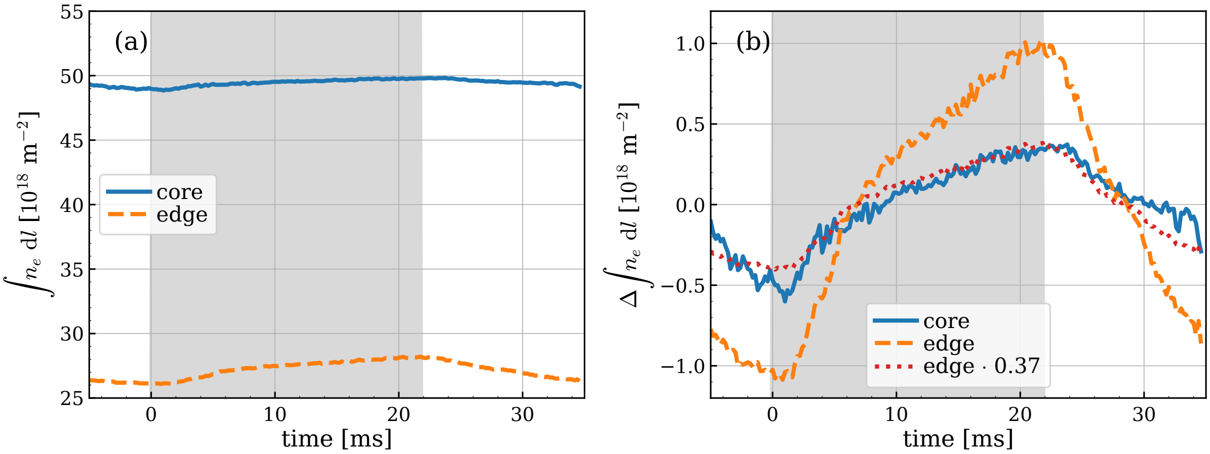

Figure 4.3.: Interferometry channels H1 (core) and H5 (edge), conditionally averaged. In the grey shaded intervals the fuelling valve is open, and closed otherwise. The figure shows the full signals (a) and the signals with the mean subtracted (b). The red dotted line is the signal one would expect if only plasma outside of $\rho_{\mathrm{pol}} = 0.9$ modulates.

4.1.1. Edge Density

The density modulation is clearly visible in interferometry [Mly10] measurements. Figure 4.3 shows the core channel H1 and the edge channel H5 ((see figure 3.1). The other channels behave analogously and are not shown to avoid clutter. While the full signal is shown in figure 4.3a, figure 4.3b subtracts the mean to highlight the modulation. After the valve is opened the density increases, it decreases again when the valve is closed. The time t is defined to be 0 when the valve opens, at 22 ms the valve closes. Until $t \approx 9\,\mathrm{ms}$ the density increase is steeper than afterwards. The modulation is dominated by the plasma inside the separatrix because the measured SOL modulation of $\approx \pm 2 \times 10^{18}\,\mathrm{m}^{-3}$ integrated over few centimeters is small compared to the modulation amplitude of $\approx \pm 1 \times 10^{18}\,\mathrm{m}^{-2}$. Later during modelling the SOL contribution is nevertheless included. Already without modelling one can conclude that the modulation mainly comes from the plasma edge: When assuming that the modulation measured by the edge channel is exclusively due to a uniform density modulation between $\rho_{\mathrm{pol}} = 0.9$ and $\rho_{\mathrm{pol}} = 1.0$ one would expect the red dotted line as signal for the core channel. Because the red dotted line agrees well with the measured signal from the core channel, one can conclude that the density modulation is, mostly, localized outside of $\rho_{\mathrm{pol}} = 0.9$. When modelling the discharge the density will be integrated accurately without relying on such assumptions.

Outside of $\rho_{\mathrm{pol}} \approx 0.985$ the lithium [Wol93, Fis08] and thermal helium beam [Gri18, Wen22] diagnostics measure the density modulation temporally and spatially resolved. The profiles are shown in figure 4.4a and 4.4b. The SOL density increases strongest, with diminishing increase towards the separatrix: While the separatrix density still increases this is not the case at $\rho_{\mathrm{pol}} = 0.99$. As a result the separatrix density gradient flattens by 8 % (lithium beam) or 9 % (helium beam) when the valve opens. Unless an increase in fuelling leads to less particle flux this shows

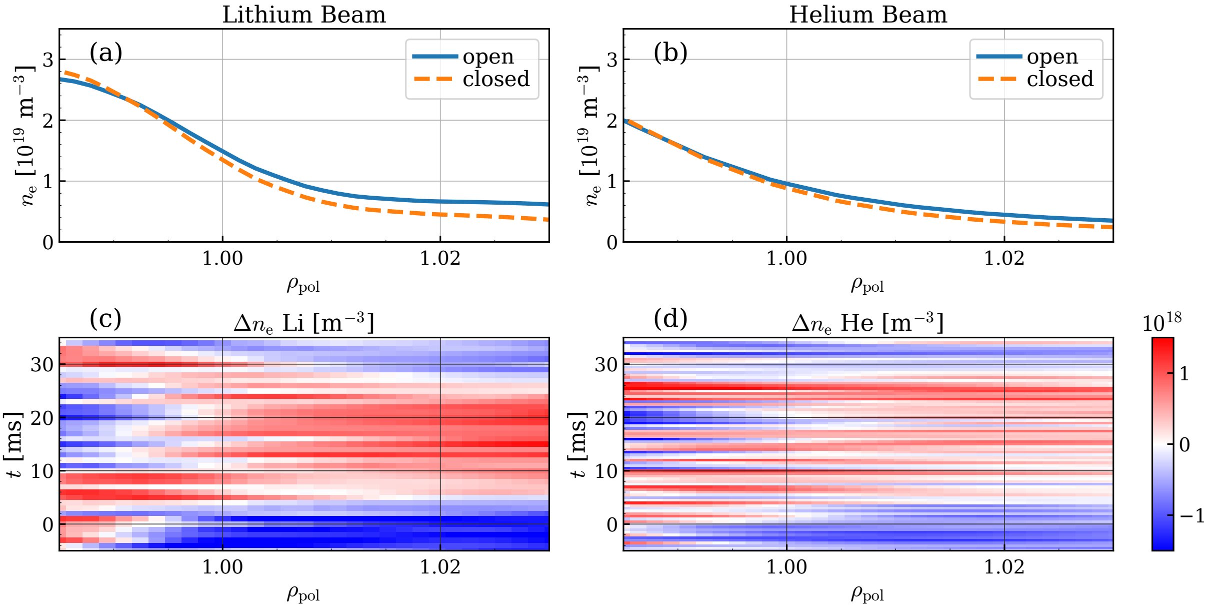

Figure 4.4.: Edge density profiles from the lithium beam (a) and the thermal helium beam (b) in the equilibrated phase before the valve opens (−5–0 ms, dashed orange line) and the equilibrated phase just before the valve closes (15–20 ms, solid blue line). The temporal evolution of the density is shown in (c) for the lithium beam and in (d) for the thermal helium beam.

that more particles are transported with a shallower gradient, suggesting an increase in transport or a change of the profile shape due to ionization.

The temporal evolution of the density is shown in figures 4.4c and 4.4d. Instead of the quantities themselves, the changes thereof are displayed: for each radius the mean density is subtracted. After the valve is opened at $t = 0$ density increases with a delay of about 3 ms. The gradient flattens at $t \approx 10$ ms, visible in the lithium beam data as a change from red to blue in the confined region. Meanwhile the SOL density remains high. According to the lithium beam data the density relaxes back to the state before the valve was opened after the valve closes at $t = 22$ ms, again with a delay of ≈ 3 ms. The helium beam shows an increase in density at $t = 22$ ms, which appears to be a diagnostic artifact as the electron temperature increases simultaneously.

4.1.2. Electron Temperature: ECE and Thermal Helium Beam

Figure 4.5 shows the electron temperature profile, and the temporal changes of the electron temperature, outside of $\rho_{\mathrm{pol}} = 0.7$. The electron temperature further inside does not influence the edge transport studies, and the temporal evolution is dominated by saw-tooth activity. The ECE is optically thick until $\rho_{\mathrm{pol}} = 0.98$, resulting in reliable T_e measurements. Further outside the thermal helium beam is able to measure the temperature profile, the modulation amplitude and the modulation phase. As stated before the ECE measurements outside of $\rho_{\mathrm{pol}} = 0.98$ could

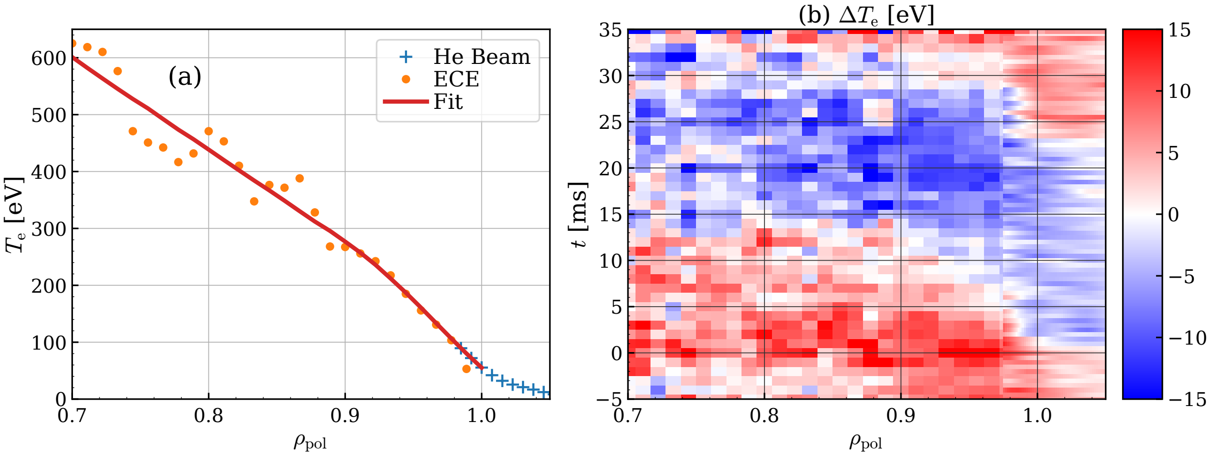

Figure 4.5.: The electron temperature profile, temporally averaged, from ECE and thermal helium beam diagnostics, with the fit used later for quantitative modelling in section 4.2 (a); and the temporal evolution of T_e (b), where only temperature *differences* are shown. In the SOL and around the separatrix, the temperatures are obtained with the thermal helium beam diagnostic. Further inside ECE provides the data.

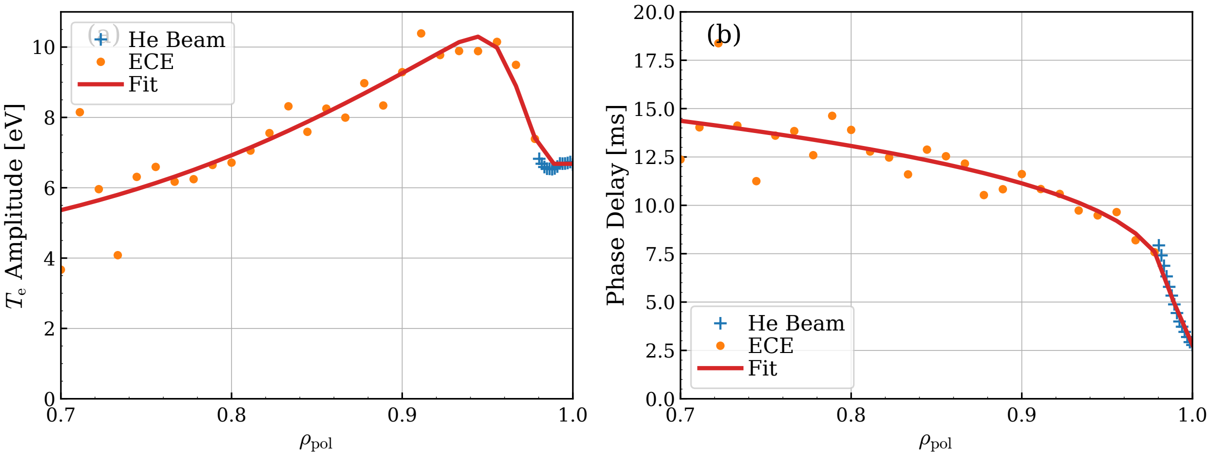

Figure 4.6.: Amplitude (a) and phase (b) of the electron temperature modulation as measured by ECE (orange circles) and the thermal helium beam (blue crosses). Additionally the fits used in modelling are shown in red.

be corrupted and are therefore not included in the analysis. It is however still worth noting that the ECE measurements show qualitatively and quantitatively the same temporal delay between $\rho_{pol} = 0.98$ and $\rho_{pol} = 0.99$ as the thermal helium beam.

After the valve is opened at $t = 0$, the temperature in the SOL drops by $\approx 10\,\mathrm{eV}$ over 3 ms, and recovers on the same time scale after the valve is closed. This perturbation continues in the confined region as a cold pulse. By fitting a sine at every radial position to the electron temperature one obtains the amplitude and phase of the modulation, which are shown in figure 4.6. Note that in this work the amplitude is defined as the prefactor of the sine, therefore a modulation amplitude of 1 eV corresponds to a difference between minimum and maximum of

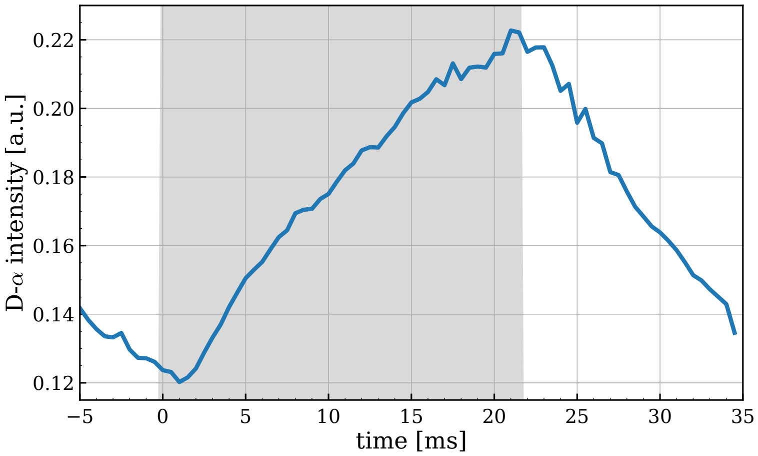

Figure 4.7.: D-α emissions as measured by a photo diode in the divertor as function of time. The fuelling valve is open in the grey shaded area.

2 eV. Starting from the separatrix with ±7 eV the amplitude of the pulse increases strongly and peaks at $\rho_{\mathrm{pol}} \approx 0.92$ at ±10 eV. Going further inwards the amplitude decays to ±5 eV at $\rho_{\mathrm{pol}} = 0.7$. The phase delay increases when moving inwards, starting at 2.5 ms. Initially the propagation speed is comparably slow (large time difference for small change in ρ_{pol}), with the delay increasing to 9 ms at $\rho_{\mathrm{pol}} = 0.98$. Then, the propagation speeds up, reaching $\rho_{\mathrm{pol}} = 0.7$ with a total delay of 14 ms. Noise, both on the profile and the temporal evolution, disturbs the transport analysis performed in section 4.2.1. The noise is therefore removed by using the red fits shown in figures 4.5 and 4.6 instead of the raw data.

4.1.3. Neutral Behavior: Ionization Gauges, D-α Emissions and the Neutral Particle Analyzer

In the following, the measurements of two diagnostics showing the temporal evolution of the neutral density, will be discussed. Then, a comparably direct measurement of the temporally averaged neutral density will be discussed.

Figure 4.7 shows the D-α emission in the divertor as collected by an unfocused photo diode as function of time, giving information about the particle recycling flux. From 1 ms after the valve is opened until the valve is closed at 22 ms the emissions rise. Initially the slope is steeper than in the end. After the valve is closed the intensity sinks until it reaches the level before the valve is opened. The time trace resembles a triangle wave. With D-α as a proxy for the neutral density, one finds that even though the fuelling gas flux operates on a sub-millisecond time scale the divertor neutral density evolves on a much longer time scale. One interpretation is that a reservoir, which is filled by the fuelling flux, acts as low pass filter for the flux. One such reservoir could be the plasma facing components in the tokamak to which deuterium adheres. Another contributing reservoir could be the sub-divertor volume. Low-pass filtering a square wave such

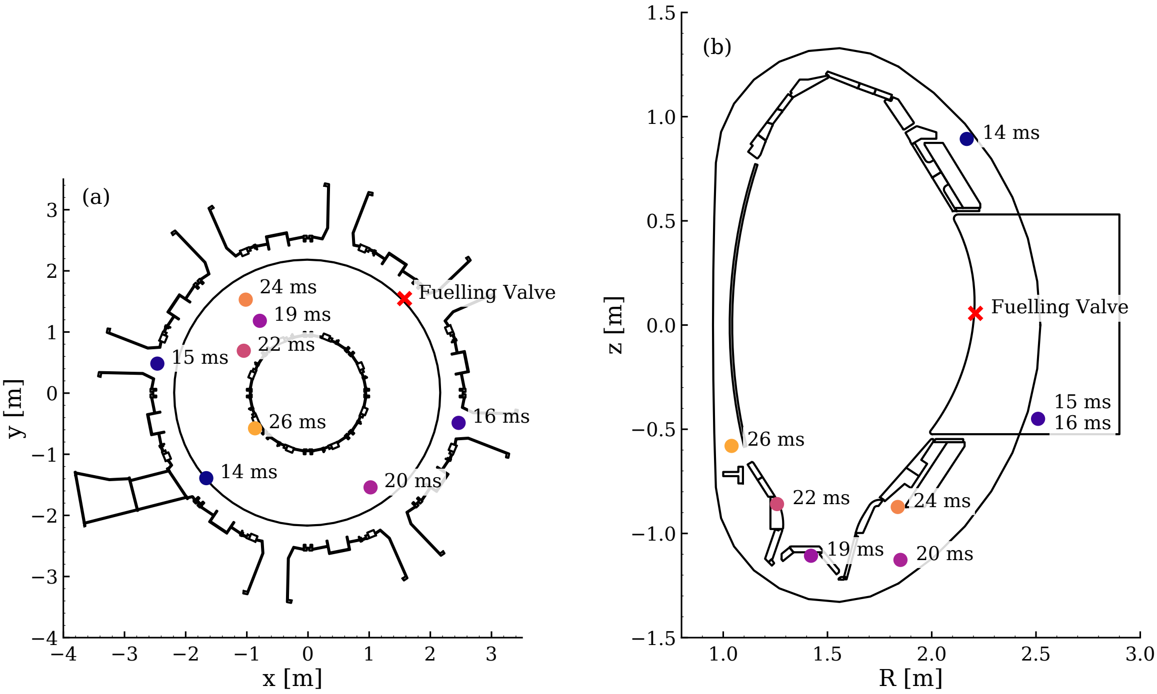

Figure 4.8.: Toroidal (a) and poloidal (b) projections of the ASDEX Upgrade tokamak with the ionization gauges (colored circles). Next to each manometer the phase delay of the measured neutral particle flux with respect to the valve opening, which also governs the color of the circles, is noted. The position of the fuelling valve is shown as red cross.

as the fuelling flow with a time constant much larger than the period of the modulation leads, in addition to the triangular shape, to a phase delay of $\pi/2 \hat{=} 10\,\text{ms}$. Fitting a sine to the measured intensity yields a phase delay of 9.3 ms.

Not only does the neutral density appear to be low-pass-filtered compared to the fuelling particle flux, there are also temporal delays depending on the poloidal position. Ionization gauges [Haa98] measure the neutral particle flux, which is a proxy for the neutral density, at different poloidal and toroidal locations. The gauges cannot react instantly to changing conditions, but their response time of $\approx 1.5\,\text{ms}$ [Lag17] is much shorter than the time scales the neutral density requires to adjust to new fuelling fluxes. Figure 4.8 shows the phase delay of the signals of these ionization gauges. All signals are delayed more strongly than the D-α emissions from the divertor. The least delayed gauges are the three radially outermost manometers with phase shifts of 14 ms, 15 ms and 16 ms. Their large toroidal separaration (see figure 4.8a) does not lead to any significant additional phase shifts. The manometers in the divertor region are delayed between 19 ms and 24 ms. The largest delay is 26 ms.

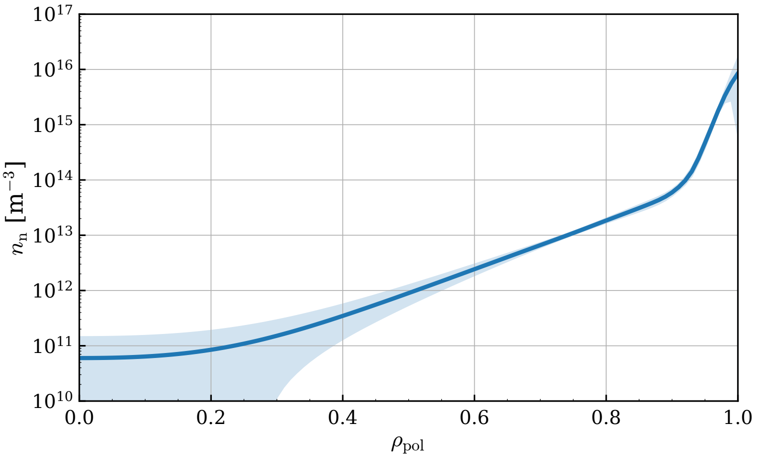

Figure 4.9.: The neutral density profile as reconstructed from NPA measurements.

The neutral density, which enters the particle density equation (2.1), is more difficult to characterize than plasma density and temperature because the neutral density is poloidally and potentially toroidally asymmetric. One therefore has to be careful when interpreting measurements from a single location. With the neutral particle analyzer (NPA) it is possible to reconstruct the density profile along one line of sight [Bog21].

Figure 4.9 shows this profile for the L-mode discharge considered in this chapter. The time resolution is not sufficient to resolve the modulation.

At the separatrix the neutral density is $1 \times 10^{16}\,\mathrm{m}^{-3}$. It drops quickly to $1 \times 10^{14}\,\mathrm{m}^{-3}$ at $\rho_\mathrm{pol} \approx 0.9$, going further inside the neutral density declines more slowly. The sharp bend in the profile at $\rho_\mathrm{pol} = 0.9$ likely comes from the reconstruction method which utilizes a modified hyperbolic tangent function to parametrize the neutral density profile.

4.2. Analysis Method

This section describes and motivates how transport properties are recovered from the measured data presented in the previous section.

A key component of the workflow is the ASTRA transport code [Per02]. It is used to compute the temporal evolution of the density profile, given the prescribed transport coefficients, and to obtain the heat diffusivity from the measured T_e and the reconstructed density.

Figure 4.10 shows the workflow of the analysis. As described in detail later (section 4.2.3) the conclusions are drawn by fitting parameters, such as the particle transport coefficients, to the experimental data for several initial guesses of the coefficients.

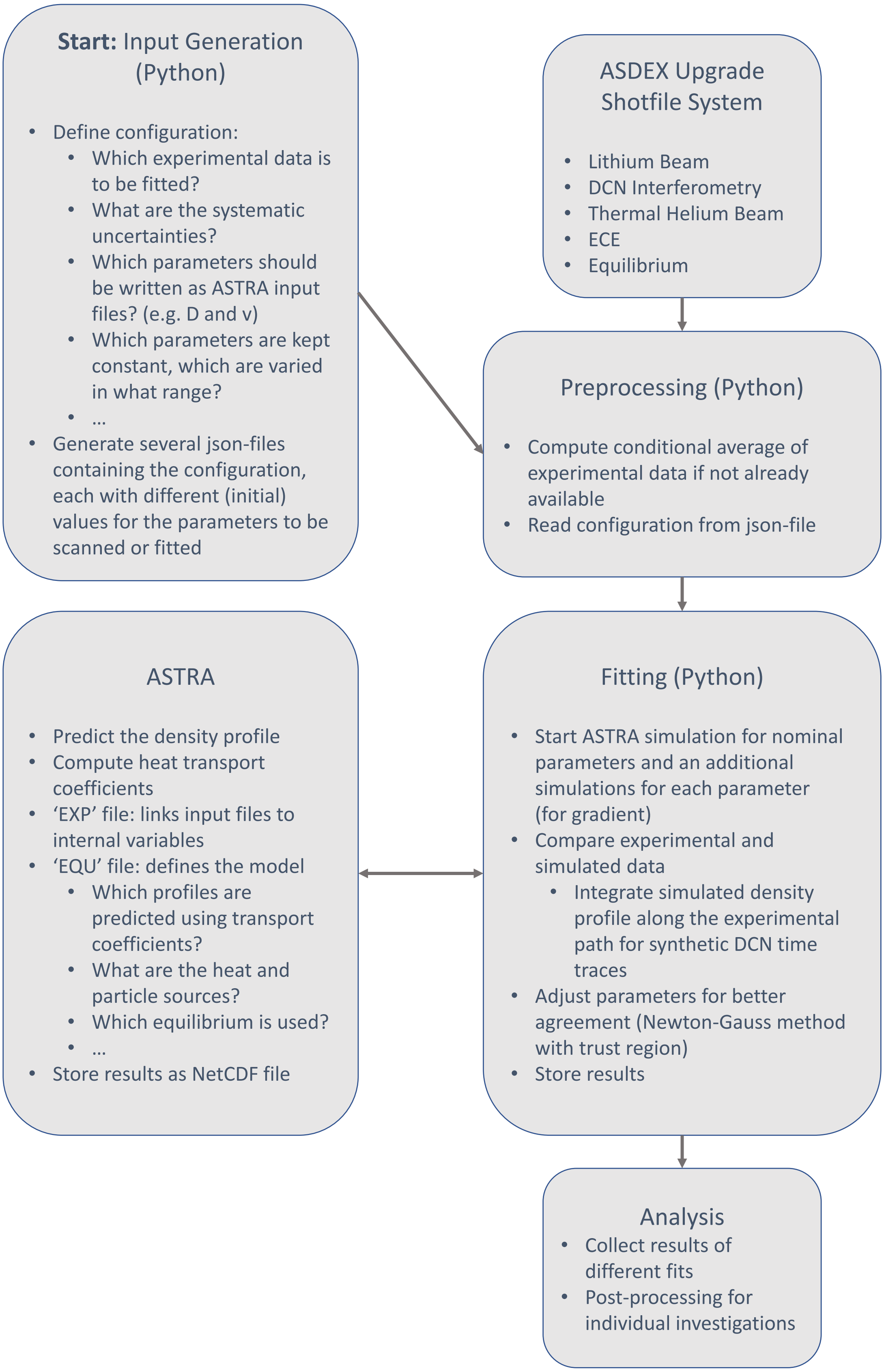

Start: Input Generation (Python)

- Define configuration:
  - Which experimental data is to be fitted?
  - What are the systematic uncertainties?
  - Which parameters should be written as ASTRA input files? (e.g. D and v)
  - Which parameters are kept constant, which are varied in what range?
  - …
- Generate several json-files containing the configuration, each with different (initial) values for the parameters to be scanned or fitted

ASDEX Upgrade Shotfile System

- Lithium Beam
- DCN Interferometry
- Thermal Helium Beam
- ECE
- Equilibrium

Preprocessing (Python)

- Compute conditional average of experimental data if not already available
- Read configuration from json-file

ASTRA

- Predict the density profile
- Compute heat transport coefficients
- ‘EXP’ file: links input files to internal variables
- ‘EQU’ file: defines the model
  - Which profiles are predicted using transport coefficients?
  - What are the heat and particle sources?
  - Which equilibrium is used?
  - …
- Store results as NetCDF file

Fitting (Python)

- Start ASTRA simulation for nominal parameters and an additional simulations for each parameter (for gradient)
- Compare experimental and simulated data
  - Integrate simulated density profile along the experimental path for synthetic DCN time traces
- Adjust parameters for better agreement (Newton-Gauss method with trust region)
- Store results

Analysis

- Collect results of different fits
- Post-processing for individual investigations

Figure 4.10.: Flowchart of the analysis workflow.

The first step is to generate the inputs for the subsequent fits and simulations. For each individual fit, a configuration file is created which specifies

- the diagnostics whose data is to be fitted,
- the systematic uncertainties of the data,
- and which parameters ASTRA requires, whether they are fixed or to be fitted, and in which ranges they are allowed to vary.

For each configuration file the parameters are selected randomly inside their allowed range. This results in scans of the fixed parameters and different initial positions for each fit, which then result in a set of possible physical values for the parameters.

After the configuration files are created, the pre-processing can start. The conditional average of all needed diagnostics is computed, as done in section 4.1, and the fitting routine is started.

The ASTRA model itself and the inputs are described in section 4.2.1. The so-called EXP file links the data and parameters written by the fitting routine to the corresponding ASTRA variable, and the EQU file defines the model.

During fitting, multiple ASTRA simulations are started in parallel: one with the nominal parameters and one each with a small increase in a parameter which has to be fitted (for computing derivatives). For each simulation the parameters and required experimental data are written into ASTRA input files. After the simulations are finished, the NetCDF files containing the results are read and the *residues* are computed. The residues are a vector of the difference between all experimental data points and the corresponding simulated values, divided by the experimental uncertainties. For comparison with interferometry the simulated density profiles are integrated along the experimental paths.

Using finite differences as approximation and the simulation results at slightly different parameters, the first derivative, i.e. the Jacobian matrix, of the residues can be computed. With `scipy.optimize.least_squares` [Vir20], a Newton-Gauss method with trust region, the new nominal parameters are calculated and the next iteration is started. The process is repeated until a local minimum is reached.

For the analysis all fits better than a threshold, defined in section 4.2.3, are considered. The different fits give samples for each quantity under investigation, giving a range of possible values for each inferred parameter, e.g. particle transport coefficients. The inferred quantities are given in section 4.2.3.

4.2.1. ASTRA Model

The 1.5D transport code ASTRA is used to model the plasma profiles in realistic geometry.

The transport coefficients in equations (2.1) to (2.3) are not necessarily constant, but are allowed to change as function of time or of plasma parameters. The discharge was initally modelled with temporally constant transport coefficients and additional off-diagonal terms such as thermodiffusion, but reproducing both the temperature profile and the cold pulse propagation was only possible by allowing an evolving χ_e. With χ_e not being temporally constant, the experimental data does not allow to draw conclusions about the off-diagonal terms, which therefore are not considered in the following.

To let the plasma background equilibrate, 50 periods are simulated, resulting in a simulated time of 2 s. Data is taken from the last simulated period. In the following the setup for the transport coefficients and source terms in equations (2.1)-(2.3) is described. Because many quantities appearing in the transport equations are not known a priori, several unknown parameters have to be introduced. The treatment of these parameters will be discussed in section 4.2.3.

Particle Transport The lithium beam data for n_e is used for $\rho_\mathrm{pol} > 0.99$, while further inside predictive simulations are performed as for T_i. The transport coefficients D and v are prescribed, enabling computing the resulting density profile and its evolution. Previously, when discussing figure 4.4, indications that the particle transport might evolve with time were found. To investigate how strongly the analysis is influenced by this uncertainty, two different cases are considered: a temporally constant D and a D that modulates outside of $\rho_\mathrm{pol} = 0.95$. Phase and amplitude of the D modulation are two parameters of the model.

Evidence of a nonzero pinch velocity v in the plasma edge will not be found when discussing the results. The analysis therefore does not investigate a temporal evolution of v, as this would be a comparably small change in a poorly determined quantity, and keeps v constant. Piece wise constant profiles with jumps at $\rho_\mathrm{pol} = [0.5, 0.7, 0.95]$ are prescribed for the particle transport coefficients. These jumps are positioned to coincide with abrupt changes in the gradients of the experimental profiles. These positions are therefore not universal for L-modes in general but depend on the analyzed discharges. The outer position $\rho_\mathrm{pol} = 0.95$, which is the only one relevant for the edge transport studies conducted here, is however typical for ASDEX Upgrade L-modes. Inside of $\rho_\mathrm{pol} = 0.7$, the ratio of D and v is fitted because it is not possible to disentangle them for a lack of experimental data showing the modulation. A nonpositive pinch velocity is imposed for $\rho_\mathrm{pol} < 0.7$ to avoid hollow profiles.

Neutral Population and Particle Source There are no measurements of the flux-surface averaged neutral particle density or its temporal evolution available, therefore the neutral population is parameterized and varied. With ASTRA one can calculate the neutral density profile for a given separatrix density and a given ratio between cold and hot neutrals, which are defined to have 2 eV for Franck-Condon neutrals and 25 eV for neutrals that underwent charge exchange in the SOL. The analysis does not rely on the standard ASTRA routine for this calculation, instead a novel method, described in section 4.2.2, is developed. For solving the Fokker-Planck equation describing the neutral population, slab geometry is used. Slab geometry cannot capture the effect of different flux expansions, which would lead to wider or narrower neutral density profiles. But because the ratio of cold and hot neutrals is varied, which also influences the width of the neutral density profile, the effects of the fuelling position and flux expansion are indirectly included when varying the energy distribution of the neutrals at the separatrix. Analogously, an altered source profile due to turbulent fluctuations as calculated by Marandet et al. [Mar11], is included due to the flexible width of the particle source.

The neutral population interacts with the plasma according to ionization and charge exchange cross sections and rate coefficients: an electron impact ionization leads to a loss of 13.6 eV in the electron channel and the gain of the neutral energy in the ion channel. A charge exchange reaction leads to the loss of thermal ion energy and the gain of the original neutral energy in the ion channel.

The neutral population, and therefore the source term, are parametrized as follows: in addition to the ratio between cold and hot neutrals, and the separatrix neutral densities in the phases with open and closed valve, there are two parameters for the timing of the neutrals: the delay between the valve opening and the change in neutral density, and the temporal width of the linear transition between the open and closed state.

Power Terms Electrons receive power from Ohmic and (central) ECR heating, and are cooled by radiation, collisional heat transfer to ions, and ionizing and exciting neutral atoms. The contributions of neutrals are much smaller than the other terms, but as they are directly influenced by the gas puff modulation they are included to avoid attributing changes to altered transport when they actually stem from neutral interactions. Ions are only heated by collisional heat exchange, and cooled by charge exchange reactions with cold neutrals. Recombination of ions and electrons also removes heat from the ion channel. Although this last contribution is very small it is included as it does not complicate the analysis. The tungsten concentration is selected such that the radiated power matches the experiment.

Heat Transport For T_e, accurate measurements for the whole domain are available. The experimental profile and its temporal evolution can therefore be prescribed. As the power fluxes and ∇T_e are known one can calculate the electron heat diffusivity χ_e needed to arrive at the experimental T_e. For T_i on the other hand there are no measurements available. Therefore, $T_\mathrm{e} = T_\mathrm{i}$ is assumed at $\rho_\mathrm{pol} > 0.99$, which is realistic for L-modes with moderately high density such as the discharge analyzed here. To correctly predict the heat fluxes, T_i in the whole plasma is needed. To obtain the missing data, T_i is predicted using $\chi_\mathrm{i} \propto \chi_\mathrm{e}$. The proportionality constant is varied to scan reasonable values thereof.

Upper Bound for Particle Flux due to Energy Considerations Each neutral atom that is ionized results in a cold electron and a cold ion that have to be heated up to local plasma temperatures, in addition to the comparably little 13.6 eV required for ionization. This power for heating up freshly ionized particles is kept track of indirectly: in the long term, every electron and every ion that was added to the plasma leaves the plasma again and takes thermal energy with it, resulting in outward convective heat fluxes. In most works, including this work, these convective heat fluxes do not appear explicitly in equations (2.2) and (2.3). Instead these losses are included implicitly in χ_e and χ_i, which are effective diffusivities. This however can hide the following issue: with large particle fluxes the convective heat fluxes could become larger than the heating power entering the plasma. The turbulent heat conduction would then have to be negative to transport power from the outer plasma boundary inward, from low to high temperatures.

This section describes how such unphysical situations are detected. To this end the power needed to ionize and heat all particles entering the main plasma is calculated. If this power exceeds the total heating power the simulation is discarded.

The speed of the neutral particle before ionization is negligible when considering the energy required for heating up the electron, but not for the ion. With $Z_\mathrm{eff} \approx 1$ the particle fluxes of electrons, ions, and neutrals have to be equal in absolute value for the ionization process: $\Gamma_\mathrm{e} = \Gamma_\mathrm{i} = \Gamma_\mathrm{n}$.

$$\begin{aligned} P_\mathrm{heatup,e} &= \frac{3}{2} T_\mathrm{e} \Gamma_\mathrm{n} && (4.1)\\ P_\mathrm{heatup,i} &= \frac{3}{2} \left(T_\mathrm{i} - T_\mathrm{n}\right) \Gamma_\mathrm{n} && (4.2)\\ P_\mathrm{ion} &= 13.6\,\mathrm{eV} \cdot \Gamma_\mathrm{n} && (4.3)\\ P_\mathrm{loss,tot} &= P_\mathrm{heatup,e} + P_\mathrm{heatup,i} + P_\mathrm{ion} && (4.4)\\ &= \left(\frac{3}{2} \left(T_\mathrm{e} + T_\mathrm{i} - T_\mathrm{n}\right) + 13.6\,\mathrm{eV}\right) \Gamma_\mathrm{n}. && (4.5) \end{aligned}$$

All results where $P_\mathrm{loss,tot} > 1.2\left(P_\mathrm{heat} - P_\mathrm{rad}\right) \approx 1.2 \cdot 830\,\mathrm{kW}$ are excluded, where a tolerance of 20 % is included to account for uncertainties.

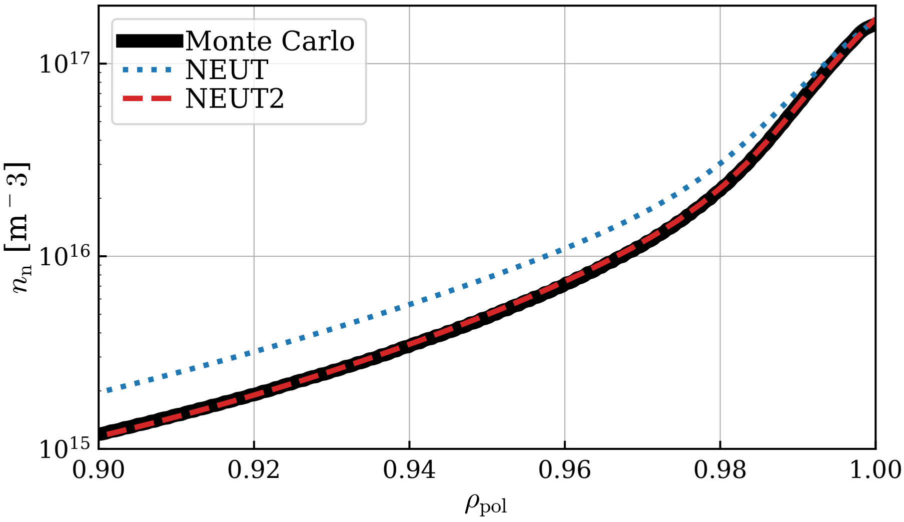

Figure 4.11.: Comparison of the neutral atom density as calculated by three different algorithms for the L-mode #37758 under investigation.

4.2.2. Novel Algorithm for Computing the Edge Neutral Atom Density

Usually, ASTRA simulations use the included NEUT subroutine to calculate the density of neutral atoms in the edge. Because the particle source is an important quantity for the study presented in this dissertation, the accuracy of the NEUT subroutine was investigated, and subsequently a novel algorithm for solving for the neutral particle source was developed.

A python program that performs a Monte Carlo simulation was developed as benchmark. Because the neutral particle density decays over distances much smaller than the minor radius, slab geometry is used. Neutral atoms cross the separatrix with a velocity vector according to a set distribution. Because all forces acting on the particles are negligible, they are advanced according to

$$\vec{x}(t_0 + \tau) = \vec{x}(t_0) + \vec{v}\tau \tag{4.6}$$

using a small time step $\tau = 4\,\mathrm{ns}$. Because of the slab geometry, and because only the distribution in real space is of interest, this equation can be simplified to be one dimensional. At each time step the probability to undergo an atomic process during a time span of τ is calculated. The same cross sections as ASTRA are used. The two considered processes are:

Electron Impact Ionization The neutral atom is removed from the simulation. A new particle is launched at the separatrix.

Charge Exchange Reaction with Plasma Ion The velocity vector of the neutral atom is set to a random value from the local thermal ion distribution.

Figure 4.11 shows the neutral particle density as a function of radius. Using NEUT (blue dotted line) one obtains a neutral density profile that does not decay as fast as the neutral density profile from the Monte Carlo simulation (black solid line). Documentation explaining how NEUT works and what the underlying assumptions are is not available.

The neutral density is recalculated at every time step in ASTRA. The Monte Carlo simulation requires tens of seconds for a profile instead of the several milliseconds NEUT requires. It is not feasible to replace NEUT with a Monte Carlo simulation similar to the one used for the benchmark because NEUT is already as computationally expensive as the transport solver. Therefore, a novel algorithm is developed that reproduces the Monte Carlo simulation while being four orders of magnitudes faster.

The neutral atom population is treated kinetically. The distribution function $f\left(\vec{x}, \vec{y}, t\right)$ is described by the Fokker-Planck equation

$$\partial_{\mathrm{t}} f = -v \cdot \nabla_{\mathrm{x}} f - F \cdot \nabla_{\mathrm{v}} f + S\left(f, x, v, t\right). \tag{4.7}$$

v is the vector of the velocity coordinates, F the force vector and S the source term which treats the atomic processes:

$$\begin{aligned} S\left(f, x, v, t\right) = & - s_{\mathrm{ion}}\left(x, t\right) n_{\mathrm{e}}\left(x, t\right) f(v, x, t) & (4.8) \\ & - s_{\mathrm{cx}}\left(x, t\right) n_{\mathrm{i}}\left(x, t\right) f(v, x, t) & (4.9) \\ & + s_{\mathrm{cx}}\left(x, t\right) n_{\mathrm{i}}\, \mathcal{M}\left(v, T_{\mathrm{i}}(x, t)\right) \int_{\mathbb{R}^3} f(v, x, t)\, \mathrm{d}v. & (4.10) \end{aligned}$$

$\mathcal{M}\left(v, T_{\mathrm{i}}(x, t)\right)$ is the normalized Maxwellian distribution function which depends on the ion temperature T_{i}. Term (4.8) is the electron impact ionization, term (4.9) represents the charge exchange losses, and term (4.10) the charge exchange gains. s are the respective reaction rate coefficients. If one integrates terms (4.9) and (4.10) the Maxwellian becomes 1, and the terms cancel: the charge exchange process does not lead to the gain or loss of particles, but to a redistribution of the particles in phase space.

The time a Franck-Condon neutral takes to cross the minor radius is of the order of several microseconds. Therefore the neutral particle density will reach the steady state very fast compared to the millisecond time scale ASTRA resolves, and one can assume the steady state for the distribution function. The time derivative of f is therefore 0. We also set $F = 0$ because all forces acting on the particles are negligible. Finally x is simply the radial coordinate because of the used slab geometry. Then only the radial derivative appears in equation (4.7), only requiring considering the radial velocity for v. Equation (4.7) then becomes

$$0 = -v\partial_{\mathrm{x}} f - s_{\mathrm{ion}} n_{\mathrm{e}} f - s_{\mathrm{cx}} n_{\mathrm{i}} f + s_{\mathrm{cx}} n_{\mathrm{i}}\ \mathcal{M} \int_{-\infty}^{\infty} f \ \mathrm{d}v \tag{4.11}$$

$$\partial_{\mathrm{x}} f = \frac{1}{v}\left[-s_{\mathrm{ion}} n_{\mathrm{e}} f - s_{\mathrm{cx}} n_{\mathrm{i}} f + s_{\mathrm{cx}} n_{\mathrm{i}}\ \mathcal{M} \int_{-\infty}^{\infty} f \ \mathrm{d}v\right]. \tag{4.12}$$

This is the integro-differential equation for $f(x, v)$ one must solve to obtain the neutral density. The boundary conditions are as follows:

$f(0, v) = f(0, -v)$: At the magnetic axis, which becomes a plane at $x = 0$ in slab geometry, a particle that moves inward becomes a particle that moves outward (mirror boundary condition). Therefore, just at the reflection point, there is an outward travelling particle for each inward travelling particle. This is equivalent to $f(x, v) = f(-x, -v)$: Symmetry dictates that we obtain the same distribution function independent of the side of the plasma slab.

$f(a, v < 0) = f_0$: The velocity distribution of neutral particles that enter the confined region at the effective minor radius a is prescribed.

To understand the problem better, several simplified and insufficient methods are discussed before arriving at the final method. If $s_{\mathrm{cx}} = 0$, equation (4.12) becomes an ordinary differential equation that is easily solvable with standard numerical methods: one starts with f_0 as initial condition and integrates from $x = a$ to $x = -a$ for various different v values. The indexing of the discrete f_{i} and v_{i} such that negative i refer to inward travelling velocities and positive i index outward travelling velocities. Because the different f_{i} do not interact, one can solve for them individually. This yields $f(x, v < 0)$. From the mirror boundary one knows $f(x, v) = f(-x, -v)$: if one solves for the distribution function of the inward travelling particles, and crosses the magnetic axis, the inward travelling particles become the outward travelling particles. By continuing to solve until $x = -a$, the distribution function of the outward travelling particles is obtained.

Another comparably easily solvable problem is solving the same equation (4.12) with different boundary conditions, even if $s_{\mathrm{cx}} \neq 0$: if, instead of the mirror boundary condition, the full distribution function at the separatrix is prescribed, f can be discretized as before, along the v coordinate. The integral can be approximated with a numerical quadrature rule, making it a weighted sum of the different f_{i}:

$$\partial_{\mathrm{x}} f_{\mathrm{i}} = \frac{1}{v_{\mathrm{i}}}\left[-s_{\mathrm{ion}} n_{\mathrm{e}} f_{\mathrm{i}} - s_{\mathrm{cx}} n_{\mathrm{i}} f_{\mathrm{i}} + s_{\mathrm{cx}} n_{\mathrm{i}}\ \mathcal{M}\left(x, v_{\mathrm{i}}\right) \sum_i w_{\mathrm{i}} f_{\mathrm{i}}\right]. \tag{4.13}$$

This is an ordinary differential equation for each f_i which is coupled to all other f_i. Together with $f(x=a)$ this is an initial value problem which can be solved with a numerical integrator as before.

One approach to solve the physical problem with the mirror boundary condition at the separatrix, which the approach above generally violates, is to prescribe $f(x=a, v<0)$ and search for an $f(x=a, v>0)$ that satisfies the mirror boundary condition $f(0,v)=f(0,-v)$. This is cumbersome as the search space is high-dimensional (many different f_i).

A more performant solution is to instead develop an iterative algorithm. The problematic part is the charge exchange gain due to the sum: it is necessary to sum also over the outward travelling part of f, which is not yet know. In the first approach they are therefore replaced with the charge exchange gains calculated with the neutral density from the previous iteration:

$$\partial_\mathrm{x} f_\mathrm{i,n} = \frac{1}{v_\mathrm{i}}\left[-s_\mathrm{ion} n_\mathrm{e} f_\mathrm{i,n} - s_\mathrm{cx} n_\mathrm{i} f_\mathrm{i,n} + s_\mathrm{cx} n_\mathrm{i}\,\mathcal{M}\left(x, v_\mathrm{i}\right)\sum_i w_\mathrm{i} f_\mathrm{i,n-1}\right]. \tag{4.14}$$

Equation (4.14) is solved for $f(x, v<0)$ for $x \in [-a, a]$. $f(x, v>0)$ is obtained with $f(x,v) = f(-x,-v)$. In the first iteration we set $f_\mathrm{i,n-1} = 0$. Unfortunately this approach does not converge: in reality the charge exchange process conserves the number of particles, but here mass conservation is violated because the losses are calculated with $f_\mathrm{i,n}$ and the gains with $f_\mathrm{i,n-1}$.

Forcing mass conservation leads to the second approach. Instead of calculating only the gains with the old f_i one also calculates the losses with the old f_i:

$$\partial_\mathrm{x} f_\mathrm{i,n} = \frac{1}{v_\mathrm{i}}\left[-s_\mathrm{ion} n_\mathrm{e} f_\mathrm{i,n} - s_\mathrm{cx} n_\mathrm{i} f_\mathrm{i,n-1} + s_\mathrm{cx} n_\mathrm{i}\,\mathcal{M}\left(x, v_\mathrm{i}\right)\sum_i w_\mathrm{i} f_\mathrm{i,n-1}\right]. \tag{4.15}$$

While now the particle number is conserved other properties are violated: previously, all losses were proportional to f_i (and the prefactors are bounded), therefore the f_i never became zero or negative. Now this is not guaranteed anymore. As soon as one f_i is smaller in the current iteration than it was in the previous iteration, it can easily become negative. Such unphysical f_i lead to oscillations which prevent convergence. A small, but insufficient improvement is to distribute the charge exchange losses not proportional to the old distribution function but to the new one:

$$\partial_\mathrm{x} f_\mathrm{i,n} = \frac{1}{v_\mathrm{i}}\left[-s_\mathrm{ion} n_\mathrm{e} f_\mathrm{i,n} - s_\mathrm{cx} n_\mathrm{i} f_\mathrm{i,n-1}\frac{f_\mathrm{i,n}}{\sum_{i<0} w_\mathrm{i} f_\mathrm{i,n}} + s_\mathrm{cx} n_\mathrm{i}\,\mathcal{M}\left(x, v_\mathrm{i}\right)\sum_i w_\mathrm{i} f_\mathrm{i,n-1}\right]. \tag{4.16}$$

It is possible to execute the sum over the negative i in equation (4.16) because those are the values that we obtain directly and not by using $f(x,v) = f(-x,-v)$ for which the necessary values are obtained only later.

We can find a functioning iteration scheme with the following realization: the number of particles that travel outwards is smaller than the number of particles that travel inwards because particles are ionized inside the plasma. Therefore the problematic contribution of $f_{\mathrm{i,n-1}}$ is mostly from the inward travelling $i < 0$. But those $f_{i<0}$ are already known for the current iteration: when integrating at positive x they are the current values of f_{i}, and when reaching negative x one takes the values of the current iteration at $|x|$. The outward moving f_{i} is taken from the previous iteration, but because their contribution is comparably small one does not risk obtaining negative values for the distribution function. Note that it is necessary to start with equation (4.16) and not (4.15): only the real-space density of particles that travel outwards is small, the phase space density at high energies can be larger than the corresponding inward travelling density. Then individual components could still become negative. We obtain

$$\partial_{\mathrm{x}} f_{\mathrm{i,n}} = \frac{1}{v_{\mathrm{i}}} \left[-s_{\mathrm{ion}} n_{\mathrm{e}} f_{\mathrm{i,n}} - s_{\mathrm{cx}} n_{\mathrm{i}} n_{\mathrm{local}} \frac{f_{\mathrm{i,n}}}{\sum_{i<0} w_{\mathrm{i}} f_{\mathrm{i,n}}} + s_{\mathrm{cx}} n_{\mathrm{i}}\, \mathcal{M}\left(x, v_{\mathrm{i}}\right) \left(n_{\mathrm{in}} + n_{\mathrm{out}}\right) \right], \tag{4.17}$$

with

$$n_{\mathrm{in}}(x) = \begin{cases} \displaystyle\sum_{i<0} w_{\mathrm{i}} f_{\mathrm{i,n}}(x) & \text{if } x \geq 0 \\ n_{\mathrm{in}}(-x) & \text{else} \end{cases} \tag{4.18}$$

$$n_{\mathrm{out}}(x) = \sum_{i>0} w_{\mathrm{i}} f_{\mathrm{i,n-1}}(x) \tag{4.19}$$

$$n_{\mathrm{local}}(x) = \begin{cases} n_{\mathrm{in}}(x) & \text{if } x \geq 0 \\ n_{\mathrm{out}}(x) & \text{else} \end{cases} = \begin{cases} \displaystyle\sum_{i<0} w_{\mathrm{i}} f_{\mathrm{i,n}}(x) & \text{if } x \geq 0 \\ \displaystyle\sum_{i>0} w_{\mathrm{i}} f_{\mathrm{i,n-1}}(x) & \text{else} \end{cases}. \tag{4.20}$$

For each iteration, equation (4.17) is solved with the Dorman-Prince method, an explicit Runge-Kutta method of 5th order which simultaneously performs a 4th-order integration to adaptively select the step size [Hai93]. The adaptive step size proved to be crucial for resolving the steep gradient region sufficiently. During integration of the differential equation, n_{in} and the newly obtained outgoing particle density are stored as n_{out} on the ASTRA grid points. Because of the adaptive step size we also need intermediate values which we obtain by linear interpolation. The trapezoidal quadrature rule is used for solving the integral, giving us the weights w_{i}. It would be possible to use higher order methods than linear interpolation and the trapezoidal rule, but this was not necessary to obtain the required precision and could cause problems if the higher orders lead to over-swings to negative values. 25 values each are used for positive and negative

v, with linear spacing in logarithmic energy space between 1 eV and 10 keV. Usually 3 iterations are sufficient for good agreement between the novel method and the Monte Carlo method. The obtained neutral density profile is shown as dashed red line in figure 4.11, which lies above the black solid line showing the Monte Carlo results.

It is possible to prescribe arbitrary distribution functions for neutral atoms entering the confined region. To preserve compatibility with ASTRA, the distribution function is restricted to the sum of two Dirac-delta distributions in the implementation used for this work.

4.2.3. Fitting and Inference

This section discusses how values for the free parameters are determined such that simulation and experiment are in agreement. The most complete treatment would be to sample the parameter space extensively and use Bayesian inference to determine the probability distribution of the physical coefficients. Using the common Markov Chain Monte Carlo (MCMC) sampling scheme, it would be possible to directly get points in parameter space distributed according to the sought-after probability distribution. Unfortunately a single ASTRA run has a runtime of several minutes, making standard sampling schemes for Bayesian inference unfeasible. Instead, a different approach is taken: starting from random initial parameters the parameters are optimized for good agreement with the experiment. Repetition this procedure leads to a set of solutions. Due to local minima and a finite number of optimization steps, the different fits will not converge to a single point. This set does not exactly correspond to the probability distribution of the parameters as a set obtained by MCMC sampling would. It however still allows to judge which ranges of parameters result in agreement with the experiment, and are therefore plausible physical values. Just as with MCMC sampling, the samples are interpreted in a statistical sense: isolated samples in good agreement with the experiment do not mean that they must lie within the uncertainty interval. Because they are few they correspond to a small volume of parameter space and are interpreted as lying in the tail of the probability distribution.

First of all the agreement with the experiment has to be quantified. The comparison between experiment and simulation is performed with the normalized mean squared error

$$\chi^2 = \frac{1}{N} \sum_i \frac{\left(f_{i,\mathrm{ASTRA}} - f_{i,\mathrm{exp}}\right)^2}{\sigma_i^2}, \tag{4.21}$$

with N being the number of data points, $f_{i,\mathrm{exp}}$ the measured data, $f_{i,\mathrm{ASTRA}}$ the corresponding simulation result, and σ_i the experimental uncertainty. The experimental interferometry signal is compared with the signal of a virtual diagnostic which integrates n_e from ASTRA along the experimental measurement line: 5000 uniformly spaced points are placed along each beam line of the interferometer. These points in three dimensional real space are mapped to values of ρ_{pol}, and are assigned a density value using their ρ_{pol} coordinate and the interpolated density profile from ASTRA. The integration in real space is then performed using these sample points and Simpson's rule. In the SOL, which ASTRA does not model, lithium beam measurements and the assumption poloidal symmetry is used for mapping integration points to densities.

Later in this section also one case is shown where the neutral density profile is fitted to the NPA data. This is not the case for all other fits in this document. Usually one normalizes not directly by N, but subtracts one plus the number of fitted parameters [Moo76]. The different normalization only has a minor influence on χ^2 because the number of free parameters (12) is small compared to the number of fitted data points (112). The uncertainties σ_{i} for interferometry, which can only be estimated because of the poloidally unknown SOL density modulation, are far more influential. Because of the unknown SOL density response a χ^2 threshold will be selected manually. This selection eliminates any influence the normalization would have.

The analysis discriminates between systematic uncertainties, such as calibration errors, and statistical uncertainties, i.e. noise, by treating the temporal mean and the modulation as separate data points. The mean is normalized by the systematic error and the modulation by the statistical error. For the systematic error of interferometry the same values as the Bayesian integrated data analysis at AUG [Fis10] is used: 2 % for the three inner lines of sight, and 5 % for the two outer channels. The statistical error is determined directly from the different measurement periods as described in section 4.1. However, there is a time dependent systematic error that one has to account for: the SOL density evolution might not be poloidally symmetric. The influence of the SOL on the modulation in the interferometry signal, which was estimated in section 4.1, is therefore added to the uncertainty.

The optimizatoin is a maximum likelyhood fit of the parameters, i.e. a minimization of χ^2. For the optimization a Gauss-Newton method with trust regions is used, as implemented in the SciPy library in `scipy.optimize.least_squares` [Vir20]. The parameters and the ranges within they are uniformly random initialized are given in table 4.1. Note that during the optimization the parameters may leave the ranges for their initial values.

The proportionality constant between χ_{e} and χ_{i} is special in that it does not influence any measured quantity directly. Therefore it is not fitted but instead kept at the random initial value throughout the optimization procedure. The proportionality constant lies in $[0.05, 2]$. Similarly the amplitude (up to ±30 %) and phase of the D modulation are not adapted during the fit but are kept at a random value to test the robustness of the results.

The final step to be taken before one can discuss results is to determine which values for χ^2 can be considered as in agreement with the experiment, and which values are too high to be considered acceptable. In principle it is possible to use the obtained χ^2 value together with the χ^2 distribution [Gut20, 1.3.6.6.6] to calculate the probability that the discrepancies between fit

Quantity	No. of scalar parameters	initialization value or range
D	4	$0.4\,\mathrm{m^2\,s^{-1}}$ to $2\,\mathrm{m^2\,s^{-1}}$
v	2	$-5\,\mathrm{m\,s^{-1}}$ to $5\,\mathrm{m\,s^{-1}}$
valve opening delay	1	3 ms
valve transition time	1	3 ms
tungsten concentration	1	5.5×10^{-6}
share of cold neutrals at separatrix	1	90 %
neutral densities for open and closed valve	2	$0.5 \times 10^{16}\,\mathrm{m^{-3}}$ to $4 \times 10^{16}\,\mathrm{m^{-3}}$
phase of D modulation	1 (fixed)	0 ms to 40 ms
amplitude of D modulation	1 (fixed)	±0 % to ±30 %
proportionality constant between χ_e and χ_i	1 (fixed)	5 % to 200 %

Table 4.1.: The 15 free parameters in the ASTRA model and the values they are initialized with. The last three are kept at the initial, random values instead of being fitted to show that the results are insensitive to them.

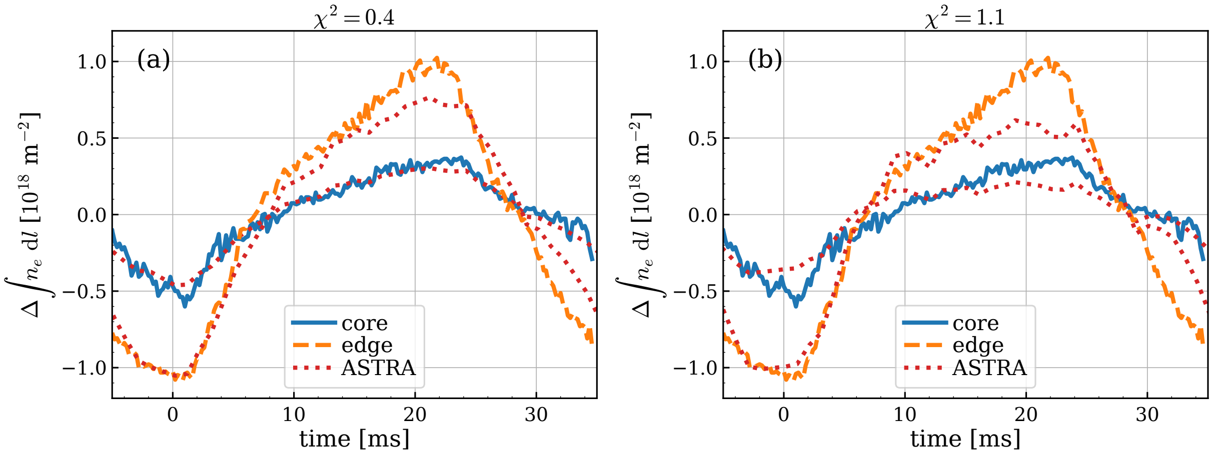

Figure 4.12.: The density modulation as measured by interferometry channels H-1 (core) and H-5 (edge), and the simulated time traces from ASTRA. (a) shows a fit with $\chi^2 = 0.4$, with modulating D, no pinch, and a mean neutral atom influx across the separatrix of $11 \times 10^{21}\,\mathrm{s^{-1}}$. The fit in (b) has $\chi^2 = 1.1$, with a temporally constant D, a pinch with $v = -13\,\mathrm{m\,s^{-1}}$, and a mean neutral atom influx across the separatrix of $6 \times 10^{21}\,\mathrm{s^{-1}}$.

and measurement arise from measurement uncertainties. In practice this would require that the uncertainties σ_i in equation (4.21) are determined very accurately, which is challenging because of the unknown poloidal variation of the SOL density. Therefore the two example fits shown in figure 4.12 with different χ^2 values are considered to judge which fits to accept.

For $\chi^2 = 0.4$ (figure 4.12a) the experimental time traces are fitted well. Some discrepancies are visible: the minimal and maximal values for H-5 are lower in the simulation than in the experiment, and while the simulated H-5 signal drops more slowly than the experimental one

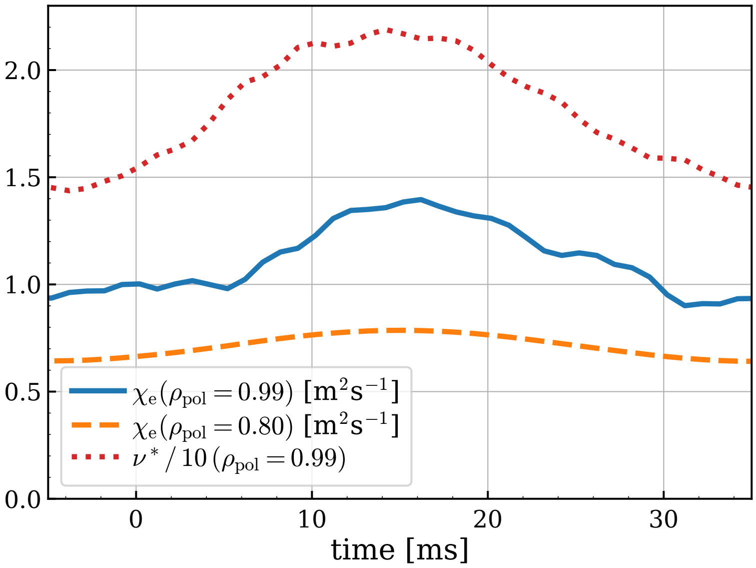

Figure 4.13.: The heat diffusivity χ_e at $\rho_{pol} = 0.99$ (blue, solid) and $\rho_{pol} = 0.80$ (orange, dashed), and collisionality ν^* (red, dotted) at $\rho_{pol} = 0.99$ as a function of time. The same case as in figure 4.12a is shown.

after $t = 30\,\text{ms}$, the H-1 signal drops faster. These discrepancies could however be caused by a non symmetric SOL behavior or to some extent be statistical fluctuations. The fit with $\chi^2 = 1.1$ (figure 4.12b) shows far more severe discrepancies: both for H-1 and H-5 the density reaches a steady state too early, resulting in too low densities at $t \approx 20\,\text{ms}$. $\chi^2 = 1$ is selected as threshold beyond which the fits are not plotted because the agreement is too poor.

Pascal Windhager from the Technical University of Vienna investigated in his bachelor's thesis, supervised by the author of this dissertation, how the neutral particle density measured by the NPA can be incorporated into the ASTRA analysis. This aspect of the analysis was not published previously. Figure 4.14 shows the experimental and the fitted density profile. In ASTRA, as always in this work, the novel method `NEUT2` is used to calculate the neutral density for the given boundary conditions. At the separatrix and in the steep gradient region good agreement is obtained. The bend at $\rho_{pol} = 0.9$ is less abrupt in the simulation. At radii inside of $\rho_{pol} = 0.7$ `NEUT2` yields higher densities than the NPA measurements. Discrepancies are however to be expected due to the usage of slab geometry in `NEUT2`, which is a valid assumption only in the edge. The neutral density at these radii is irrelevant for the presented studies as the density, and therefore particle source, is small.

As discussed in section 4.1.3 the NPA measurements are a local reconstruction, but the neutral density required for the transport analysis is the flux-surface averaged value. Therefore, to avoid relying on inadequate data, the neutral density is *not* fitted in the remainder of the thesis.

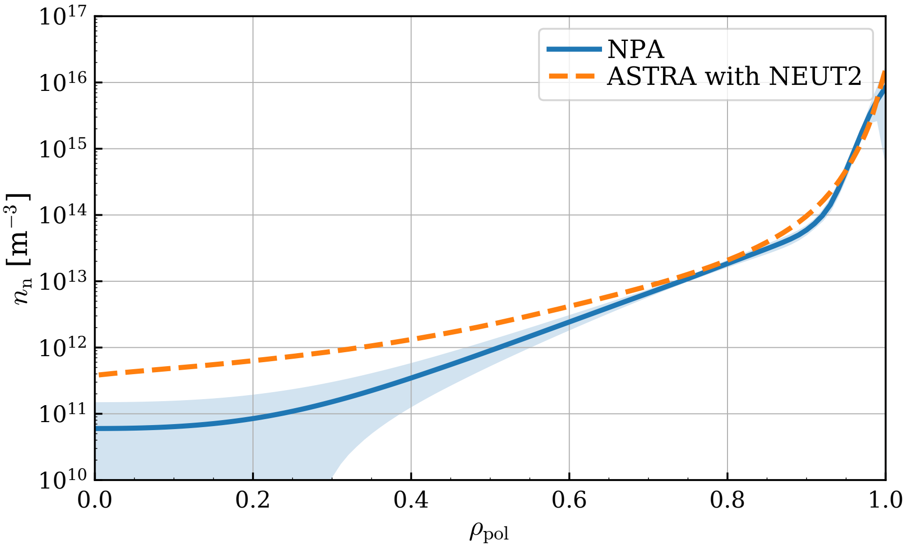

Figure 4.14.: Profiles of the neutral density n_n. The density as reconstructed from the neutral particle analyzer data and the neutral density in a fitted ASTRA simulation are shown. This is the only figure in the whole document where a case with a fit to the NPA data is shown.

4.3. Results

This section investigates which particle diffusivities (D) and pinch velocities (v) can explain the density modulation measured in the experiment; and it will be shown how the heat diffusivity χ_e evolves during the modulation. Instead of the discussion about neutrals published in [Sch22] a more general analysis is presented in section 5.3.3.

Figures 4.15 and 4.16 show the most important parameters from the successful simulations as function of the averaged neutral particle flux. The dependence of the determined quantities on the neutral particle flux is generally weak, with the pinch velocity v showing the strongest dependence. The minor variations in the determined quantities show the robustness of the results against variations in the unknown neutral particle flux.

Points marked as red '+' correspond to simulations where D modulates between $\rho_{pol} = 0.95$ and $\rho_{pol} = 1$, while simulations that employ temporally constant D appear as blue 'x'. Only data points are shown whith are better than the threshold of $\chi^2 = 1$ defined earlier, with faint colors corresponding to high χ^2 values. Simulations with mean particle fluxes across the separatrix higher than $\approx 45 \times 10^{21}\,\mathrm{s}^{-1}$ violate energy conservation, as described in section 4.2.1, and are therefore excluded.

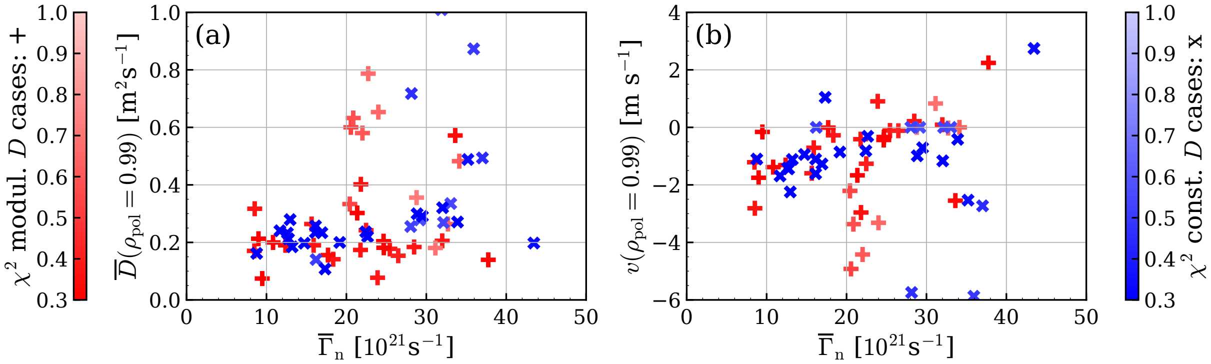

Figure 4.15.: The mean particle diffusivity (a) and pinch velocity (b) at $\rho_\mathrm{pol} = 0.99$, against the mean particle flux across the separatrix $\overline{\Gamma_\mathrm{n}}$. Simulations utilizing modulating D appear as red +, simulations with temporally constant D as blue x. There are isolated simulations with $\chi^2 > 0.7$ outside of the shown areas.

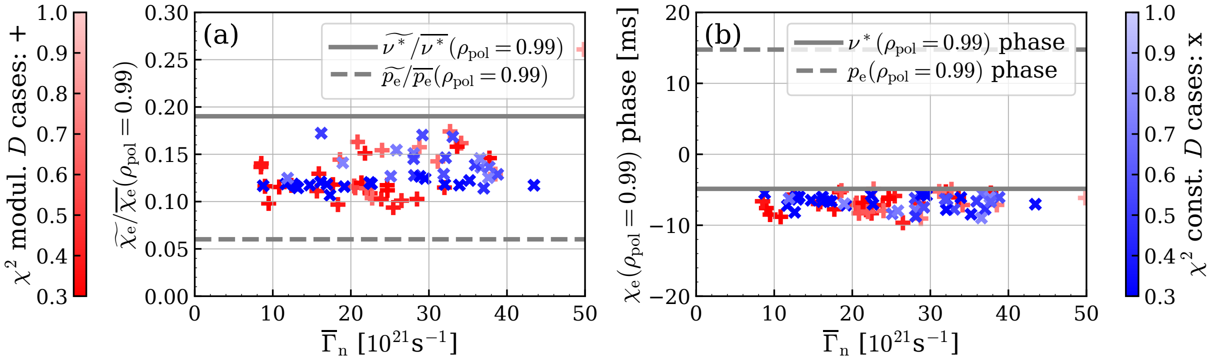

Figure 4.16.: The relative modulation amplitude (a) and phase (b) of heat diffusivity (crosses), collisionality (solid grey line) and electron pressure (dashed grey line), against the mean particle flux across the separatrix $\overline{\Gamma_\mathrm{n}}$. Simulations utilizing modulating D appear as red +, simulations with temporally constant D as blue x. There are isolated simulations with $\chi^2 > 0.7$ outside of the shown areas.

4.3.1. Particle Transport Coefficients D and v

Figures 4.15a and 4.15b show the solution sets for D and v. Because D is time dependent in the modulating case (blue), the temporal average $\overline{D}$ is discussed. Most simulations are contained in $\overline{D} = (0.20 \pm 0.13)\,\mathrm{m^2\,s^{-1}}$ and $v = (-1 \pm 2)\,\mathrm{m\,s^{-1}}$. The experimental data is consistent with purely diffusive transport. There are simulations with higher particle diffusivity and more negative pinch velocities, correlating with larger χ^2 values and worse agreement with the experiment. Red and blue crosses, corresponding to solutions of the two different transport models with constant and modulating D, are largely intermixed and do not occupy different regions in the parameter space. Section 5.3.3 will discuss in detail how the modulating particle transport influences the reconstruction of D and v, making the determined values for D and v unreliable. Explaining the available data does not require a pinch.

4.3.2. Temporal Evolution of Transport

Unlike particle transport the heat transport depends only weakly on the source term. Together with the spatially resolved measurements of T_e, this results in a considerably more accurate determination of χ_e than of D. Figure 4.13 shows the temporal evolution of χ_e at two radial positions and collisionality ν^*, as defined in [Oya06], for one illustrating case. All three quantities modulate in phase. The temperature modulation at the edge and its propagation into the confined region is not only due to neutral effects and a change of n_e: transport, and thus the turbulence causing it, is increased by fuelling. This chapter focuses on transport close to the separatrix at $\rho_\mathrm{pol} = 0.99$.

χ_e and ν^* modulate with similar phase and relative amplitude. Such a link between collisionality and turbulent transport is expected in several theoretical works [Rog98, Bon19, Bou12]. This is in line with the experimental observation that an increase in fuelling does not lead to the expected increase in density [Hug07, Mor20], because the change in transport with increasing ν^* was not taken into account. To quantitatively investigate how the heat transport changes, the relative modulation amplitude of $\chi_\mathrm{e}(\rho_\mathrm{pol} = 0.99)$ (figure 4.16a) and the phase of χ_e (figure 4.16b) are considered. Both quantities are determined by fitting a sine to $\chi_\mathrm{e}(\rho_\mathrm{pol} = 0.99)$. The relative modulation amplitude of ν^* is $\pm 19\,\%$. The modulation amplitudes in successful simulations fall exclusively between $\pm 9\,\%$ and $\pm 18\,\%$. A linear dependency between χ_e and ν^*, as predicted for drift-Alfvén turbulence, would result in identical relative modulation amplitudes of $\pm 19\,\%$. This is just above the range of measured data, but also the driving gradients decrease as transport increases, $\approx 8\,\%$ at the separatrix for n_e and $\approx 12\,\%$ at the separatrix for T_e. Qualitatively, the gradients at $\rho_\mathrm{pol} = 0.99$ behave identically, but quantitatively they are less reliably measured. Figure 4.16b shows the phase of $\chi_\mathrm{e}(\rho_\mathrm{pol} = 0.99)$ and $\nu^*(\rho_\mathrm{pol} = 0.99)$. Both quantities modulate with less than 5 ms difference in phase for all simulations, showing that transport and ν^* are strongly correlated. Also the electron pressure p_e is shown in figures 4.16a and 4.16b. It modulates with smaller relative amplitude than χ_e or ν^*, and in the opposite direction such that the phases are shifted by half a period. To conclude, an increasing χ_e is strongly linked to an increasing ν^*. The minor differences in the phase could easily stem from other influencing quantities that modulate out of phase, e.g. the pressure gradient.

Experimental data suggests that D modulates in phase with χ_e: according to the lithium beam, the density gradient at the separatrix flattens ≈ 10 ms after the valve is opened (figure 4.4c). The helium beam data shows more noise, making the determination of the exact timing more difficult. Simultaneously, the interferometry shows a slowing of the density rise (figure 4.3b). At the same time, heat transport increases as shown in figure 4.13. The next chapter will investigate the connection between particle transport and flattening density gradients extensively.

Note that modulation experiments offer an advantage over the analysis of steady state discharges with different fuelling levels when looking at the relative changes of χ_e: the transported power

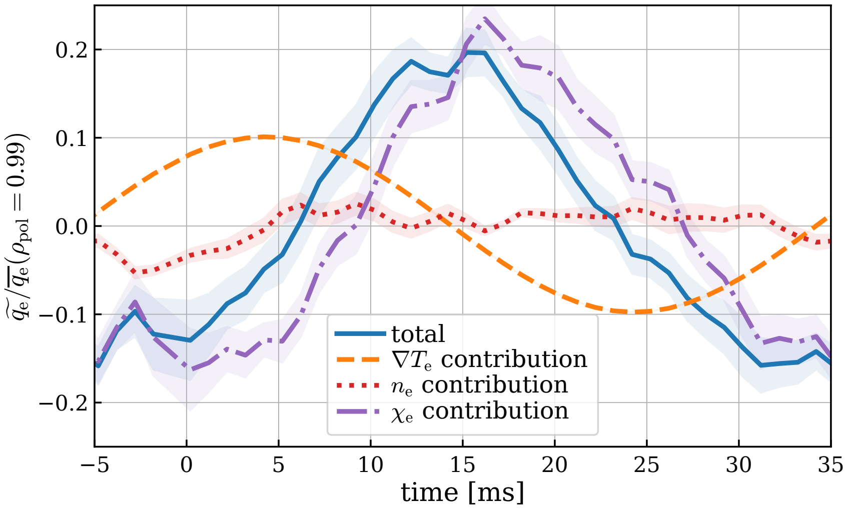

Figure 4.17.: The relative change of the electron heat flux q_e at $\rho_{pol} = 0.99$ as a function of time. The shown quantities are the total change (blue solid line) and the linearized contributions of ∇T_e (orange dashed line), n_e (red dotted line) and χ_e (purple dash-dotted line). The shaded areas show the one-sigma uncertainty of the distribution of fit results. The electron temperature is prescribed, therefore it is identical for all fits and has no uncertainty in this context.

depends not only at χ_e and ∇T_e but also on n_e. Uncertainties of n_e therefore influence the accuracy of χ_e. But constant errors in n_e cancel when calculating the relative changes of χ_e. By modulating instead of comparing different phases or even discharges, the conditions change less, keeping more of the errors of the density profile constant and thus without effect.

Another advantage of the modulation experiments is that transport can be studied in conditions which are not accessible when considering the steady state. Figure 4.17 shows, among others, the electron heat flux across the flux surface at $\rho_{pol} = 0.99$ (blue solid line). It modulates by $\approx \pm 20\,\%$, while in steady state the profiles adjust such that the heat flux equals the net heat input inside of the respective flux surface. Therefore, plasma conditions are probed with the modulation technique that are not directly accessible otherwise.

The heat flux is now separated into its individual components to judge whether the increase in transport or other effects have the largest impact on the cold pulse propagation. The electron heat flux is given by

$$q_e = n_e \chi_e \nabla T_e. \tag{4.22}$$

Each quantity is split into the mean value and the modulation:

$$\begin{align} q_e &= \left(n_{e,0} + \widetilde{n_e}\right)\left(\chi_{e,0} + \widetilde{\chi_e}\right)\nabla\left(T_{e,0} + \widetilde{T_e}\right) \tag{4.23}\\ &\approx n_{e,0}\chi_{e,0}\nabla T_{e,0} + n_{e,0}\chi_{e,0}\nabla\widetilde{T_e} + \widetilde{n_e}\chi_{e,0}\nabla T_{e,0} + n_{e,0}\widetilde{\chi_e}\nabla T_{e,0}, \tag{4.24}\end{align}$$

where terms of second and third order are discarded in the last step. The individual contributions of the density-, temperature- and heat diffusivity modulation are shown in figure 4.17. The density modulation has the smallest impact (red dotted line), while the increase in heat diffusivity has the largest impact (purple dash-dotted line). The changing gradient of the electron temperature also impacts the heat flux considerably (orange dashed line). But due to the phase shift of $\approx 12\,\mathrm{ms}$ with respect to the dominant contribution by heat diffusivity it mainly causes a phase shift and does little to alter the amplitude of the q_e modulation.

4.4. Conclusions

Fuelling modulation experiments were performed at the ASDEX Upgrade tokamak in an L-mode plasma to study the edge particle transport. Previously, the analysis of core particle transport by modulation experiments has been carried out for a variety of plasma conditions [Tal19]. The smaller study presented here is highly relevant because edge particle transport is far less understood than core particle transport:

1. Faster time scales and shorter length scales have to be resolved experimentally. One example of this are detrimental SOL effects on reflectometry that disturb the reconstruction of profiles. These effects, among others, required to discard reflectometry data which has proven to be highly valuable for core transport studies [Tal19]. Similarly it is not possible to rely on the Thomson scattering diagnostic as the time scales considered cannot be resolved. Instead, data from various diagnostics, e.g. ECE, interferometry, thermal helium beam spectroscopy, lithium beam spectroscopy, is analyzed in an integrated data approach to arrive at conclusions.

2. The (flux surfaced averaged) neutral particle source in the plasma edge is difficult to quantify, already in steady state but even more so in dynamic situations which are required to disentangle diffusion and convection. Despite these additional hindrances compared to core transport, conclusions could be drawn about the particle transport.

3. Gas puff modulation studies performed for particle transport studies usually assume that transport itself is not perturbed by the modulation. It is shown that, at least in the edge, this is in general not a valid assumption.

What happens when the deuterium gas flow into the torus is modulated? When the gas flow increases, the separatrix cools and increases in density. The cooling propagates as cold pulse into the core plasma. Interferometry measures a density increase inside the separatrix. The density profile at the separatrix flattens, suggesting an increase in transport.

By modelling the discharge in ASTRA the solution set of parameters is characterized, and thus transport coefficients and properties concerning fuelling and edge turbulence could be drawn, given the modelling assumptions. The well resolved measurements of n_e and T_e from the lithium and thermal helium beams were essential for the analysis.

The experimental data allows for a range of particle diffusivities and pinch velocities in the region outside of $\rho_\mathrm{pol} = 0.95$: most simulations lie within $\overline{D} = (0.20 \pm 0.13)\,\mathrm{m^2\,s^{-1}}$ and $v = (-1 \pm 2)\,\mathrm{m\,s^{-1}}$. A pinch is not necessary to explain the measured data. Later, in section 5.3.3, the validity of transport coefficients obtained with the presented method is discussed in detail. The relative modulation amplitude of χ_e is quantified to be between $\pm 9\,\%$ and $\pm 18\,\%$. High heat diffusivity correlates with high collisionality ν^*, as predicted by several works [Bon19, Bou12, Rog98]. The cold pulse which propagates in the plasma is due to the increased heat diffusivity. Experimental data suggests that particle transport modulates in phase with ν^* and χ_e.

In the next chapter the presented method will be used to analyse more L-mode plasmas with varying density as well as other plasma scenarios.

5. Particle and Heat Transport in the Edge of Tokamak Plasmas

In the core, plasma density and temperature are approximately constant on each flux surface due to the fast parallel transport, while there are poloidal asymmetries in the SOL. It is not obvious and subject of current research how poloidally symmetric the density just inside the separatrix is. In the previous chapter the density outside of $\rho_{\mathrm{pol}} = 0.99$ was not included in the quantitative analysis to avoid the assumption of poloidal symmetry and keep the results as robust as possible. This chapter will follow the usual [Wil13, Sal15, Mor20] convention to assume poloidal symmetry until the separatrix, allowing to fit the evolution of the density gradient at the separatrix. With this additional information it is possible to estimate the modulation of particle transport just inside the separatrix.

Findings from this chapter were presented at the 2022 H-Mode Workshop in Princeton, New Jersey; and at the 2022 ITPA meetings of the "Pedestal and Edge Physics" and "Transport and Confinement" groups in Cadarache, France.

5.1. Experiments

As in chapter 4, the experimental setup and measurements will be discussed before continuing with the analysis.

5.1.1. L-Modes at Different Densities

The AUG L-mode discharge #37758 was already the topic of the previous chapter. Now the analysis is expanded to include two later segments in the same discharge: 3.0–3.48 s and 3.9–4.4 s in addition to the previous segment at 2.1–2.45 s. The three segments differ only in the fuelling particle flow: in addition to the modulated flow of 8×10^{21} deuterium atoms per second ($\mathrm{D\,s^{-1}}$) with a 55 % duty cycle additional 0, 5×10^{21} and $10 \times 10^{21}\,\mathrm{D\,s^{-1}}$ (chronological order) are fuelled in the lower divertor. The plasma current is $I_{\mathrm{P}} = 0.8\,\mathrm{MA}$ and the toroidal magnetic field $B_{\mathrm{t}} = -2.4\,\mathrm{T}$. Central electron cyclotron resonance heating (ECRH) of 590 kW is applied.

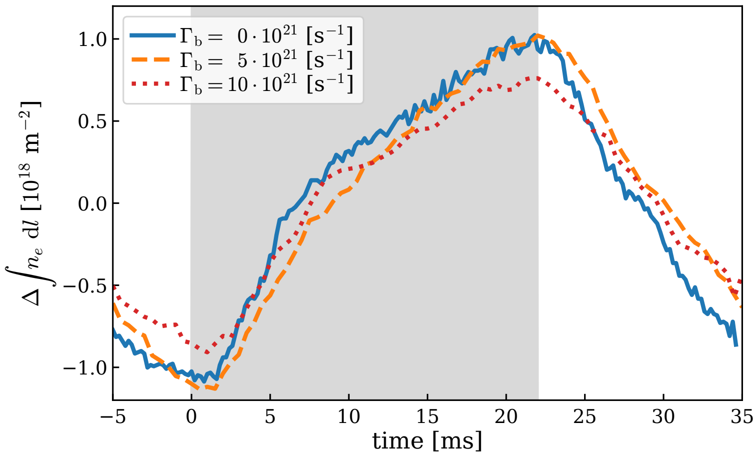

Figure 5.1.: The conditionally averaged time traces of edge interferometer H-5 for three different baseline fuelling levels in L-mode #37758. The modulation valve is open only in the grey shaded area.

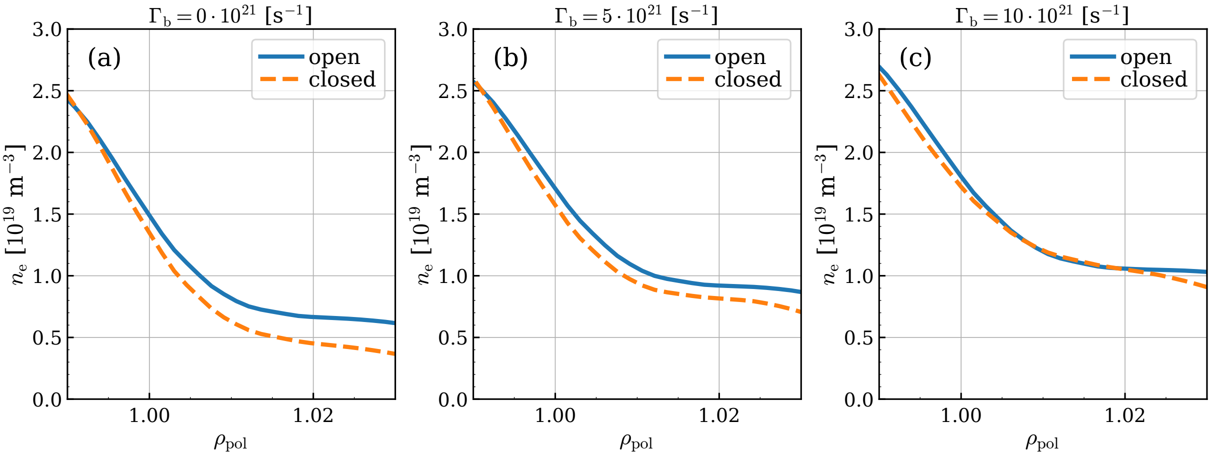

Figure 5.2.: Lithium beam profiles for three different baseline fuelling levels in L-mode #37758, each for open and closed modulation valve.

Γ_b [10^{21}s^{-1}]	n_e [10^{19}m^{-3}]	T_e [eV]	central P_e [kPa]
0	5.7 ± 0.3	1660 ± 200	15.1 ± 2.0
5	5.9 ± 0.4	1530 ± 170	14.5 ± 1.9
10	6.3 ± 0.4	1340 ± 160	13.5 ± 1.8

Table 5.1.: Central electron density, temperature and pressure at $\rho_{pol} = 0.2$ for the three investigated segments in AUG discharge #37758.

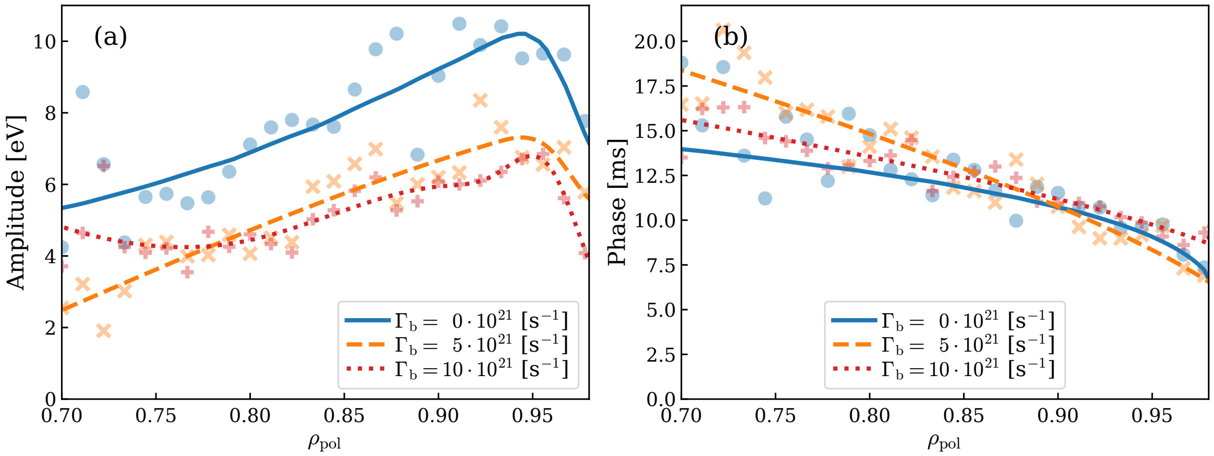

Figure 5.3.: Modulation amplitude (a) and phase (b) of the electron temperature for three different baseline fuelling levels in L-mode #37758. A positive phase corresponds to a delay with respect to the valve action. Both experimental data from ECE (symbols) and fits (lines) are shown. A phase shift of 0 would refer to a maximum cooling rate directly when the valve opens, positive phase shifts refer to a delayed cooling.

Increasing the fuelling leads to an increased central density and decreased central temperature and pressure as shown in table 5.1. The temporal evolution of the edge density as measured by interferometry is displayed in figure 5.1. The time traces are very similar. The differences between the segments could originate from the behavior of the plasma inside the separatrix or the SOL plasma. Using the lithium beam diagnostic (figure 5.2) one sees a density increase both inside and outside of the separatrix when increasing the background fuel flow. The statistical error of the density measurements is of the order of $2 \times 10^{17}\,\mathrm{m}^{-3}$ and not visible in figure 5.2. The response to the modulating gas flow differs: at $0\,\mathrm{s}^{-1}$ (figure 5.2a) and $5 \times 10^{21}\,\mathrm{s}^{-1}$ (figure 5.2b) the SOL density increases when the valve is opened, while the density increase in the confined region is less pronounced. The density gradient at the separatrix *decreases*. At $10 \times 10^{21}\,\mathrm{s}^{-1}$ (figure 5.2c) the SOL density remains almost unchanged while the density in the confined region increases. The density gradient at the separatrix therefore *increases*.

Also in the cases with background fuelling, a cold pulse propagates in the edge plasma. Due to the higher density of the later segments the helium beam data is unavailable, leaving only the ECE data which is reliable inside of $\rho_{\mathrm{pol}} = 0.98$. The amplitude of the T_{e} modulation (figure 5.3a) generally decreases with increasing background fuelling, while the radial dependency is similar. In the phase of T_{e} (figure 5.3b) an inward travelling cold pulse is visible in all cases. The speed of propagation differs between the three cases with the intermediate background fuelling (dashed orange line) being the slowest, and the case without background fuelling (blue solid line) being the fastest.

5.1.2. H-Modes with Varying Heating Power

Discharge #37760 is set up identically as the L-mode #37758 which was discussed in the previous section, except for the location of the modulation valve. Unexpectedly, this caused a transition into H-mode. For #37773, which also used the HFS modulation valve, the ECR heating power was increased from 0.6 MW to 1.8 MW. The time intervals under consideration are 2.85–3.45 s (#37760) and 2.80–3.50 s (#37773). The increased heating power in #37773 leads to the appearance of broad structures at $\approx 60\,\mathrm{kHz}$ in the spectrogram of the line emissions of the helium beam which are discussed in more detail in the next section. For all ELMy H-modes in this thesis 1 ms before and 4 ms after each ELM are removed, meaning only the inter-ELM-phase is considered.

The edge interferometry (figure 5.4) shows that the differences in heating power lead to different responses to fuelling: with 0.6 MW of ECRH the density rises strongly after the valve is opened. Similar to the L-modes discussed in the previous section, the initial density increase until $\approx 7\,\mathrm{ms}$ is steeper than the density increase between 7 ms and 22 ms. The absolute change in line integrated density is $2.7 \times 10^{18}\,\mathrm{m}^{-2}$, which is a stronger response than in L-mode. With 1.8 MW of ECRH the signal to noise ratio is worse and the density increase is less pronounced with an absolute change of $1.1 \times 10^{18}\,\mathrm{m}^{-2}$.

The lithium beam profiles (figure 5.5) show that the separatrix density rises in both cases when the valve is opened. With 0.6 MW ECRH (5.5a) the density steepens at the separatrix, coinciding with a stronger density increase of $6 \times 10^{18}\,\mathrm{m}^{-3}$ at $\rho_{\mathrm{pol}} = 0.99$ compared to $4 \times 10^{18}\,\mathrm{m}^{-3}$ at the separatrix. With 1.8 MW the electron density increases by $3 \times 10^{18}\,\mathrm{m}^{-3}$ both at $\rho_{\mathrm{pol}} = 0.99$ and $\rho_{\mathrm{pol}} = 1.0$, resulting in an unaltered gradient.

As in the L-modes cases, a cold pulse propagates inside of the separatrix. The amplitude is comparable to the L-mode cases in figure 5.3 with the low heating case having a maximum amplitude of $\pm 7.6\,\mathrm{eV}$ at $\rho_{\mathrm{pol}} = 0.94$. The maximum amplitude in the high heating case is $\pm 5.9\,\mathrm{eV}$ at $\rho_{\mathrm{pol}} = 0.85$. At the radii outside of $\rho_{\mathrm{pol}} = 0.85$, which are most relevant for the edge transport studies conducted here, the amplitude in the high heating case is smaller while the phase is mostly identical. Further inwards the cold pulse propagates faster for the high heating case.

5.1.3. ECR Heated H-Modes at Different Densities and EDA H-Mode

AUG discharge #37773, whose second stationary segment was discussed already in the previous section, is identical to #37758 except for the location of the modulation valve which is situated on the HFS and the increased heating power of 1.8 MW ECRH. The discharge is in H-Mode at all investigated timepoints. Due to the higher temperature the resistivity of the plasma

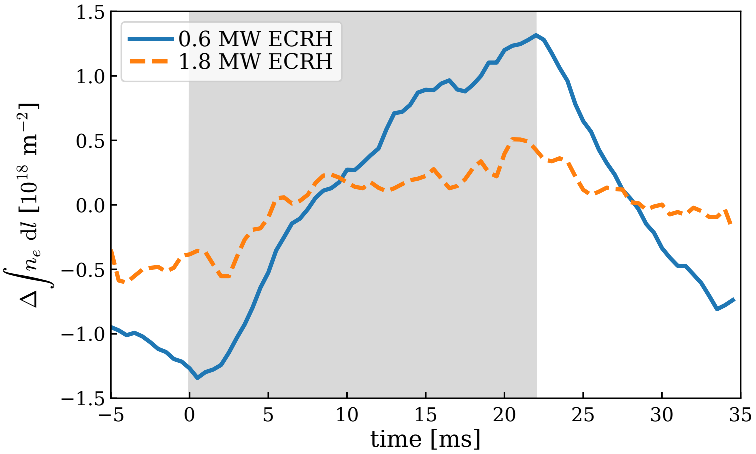

Figure 5.4.: The conditionally averaged time traces of edge interferometer H-5 for two different heating powers in H-mode, both with $\Gamma_\mathrm{b} = 5 \times 10^{21}\,\mathrm{s}^{-1}$. The modulation valve is open only in the grey shaded area.

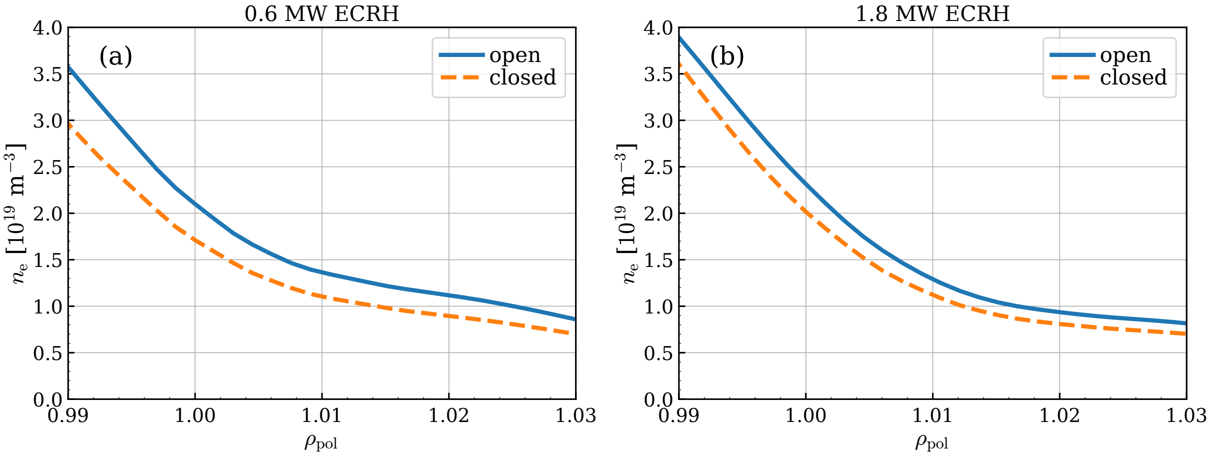

Figure 5.5.: Lithium beam profiles for two different heating powers in H-mode, each for open and closed modulation valve. The background fuelling flow $\Gamma_\mathrm{b} = 5 \times 10^{21}\,\mathrm{s}^{-1}$ is identical in both cases.

is reduced, allowing driving the plasma current for a longer length of the discharge, allowing to include an additional step in fuelling at the end. The four stationary segments 1.95–2.5 s, 2.8–3.5 s, 3.9–4.75 s and 5.05–5.8 s are investigated, with respective additional fuelling flows Γ_b of 0, 5×10^{21}, 10×10^{21} and $12 \times 10^{21}\,\mathrm{D\,s^{-1}}$ (chronological order) from the lower divertor.

Figure 5.7 shows the spectrogram of the helium beam emissions at $\rho_\mathrm{pol} = 0.99$. Starting from 1.7 s, there is a narrow banded structure between 30 kHz and 70 kHz. This structure, which is the quasi-coherent mode (QCM), causes transport which can keep the pedestal stable to ideal MHD modes and is characteristic for the EDA H-mode. Starting from 2.2 s, a broad structure is visible between 40 kHz and 90 kHz which remains for the rest of the discharge. This broad structure is reminiscent of the quasi-continuous exhaust regime (QCE) which will be presented in the next

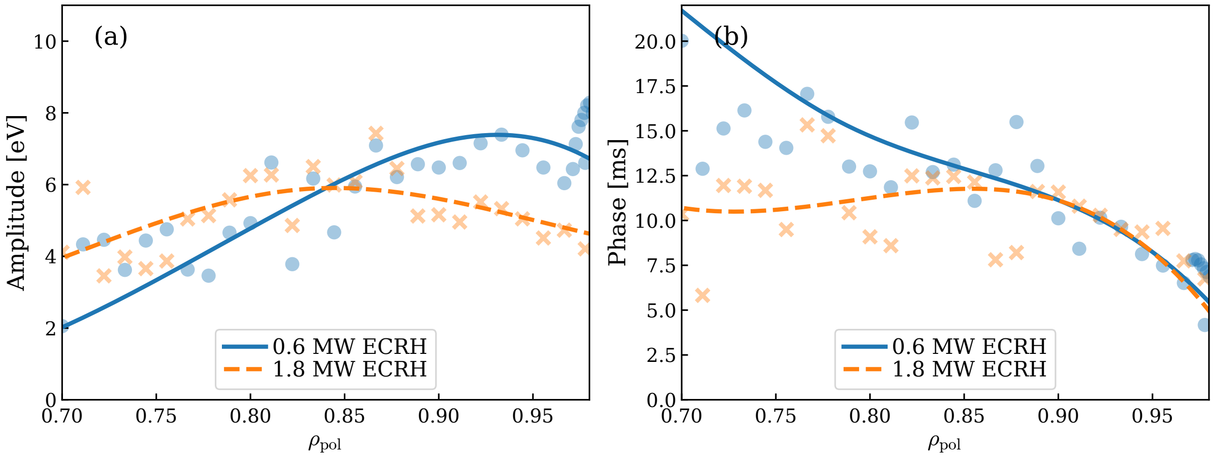

Figure 5.6.: Modulation amplitude (a) and phase (b) of the electron temperature for two different heating powers in H-mode, both with $\Gamma_b = 5 \times 10^{21}\,\mathrm{s}^{-1}$. A positive phase corresponds to a delay with respect to the valve action. Both experimental data from ECE (symbols) and fits (lines) is shown. A phase shift of 0 would refer to a maximum cooling rate directly when the valve opens, positive phase shifts refer to a delayed cooling.

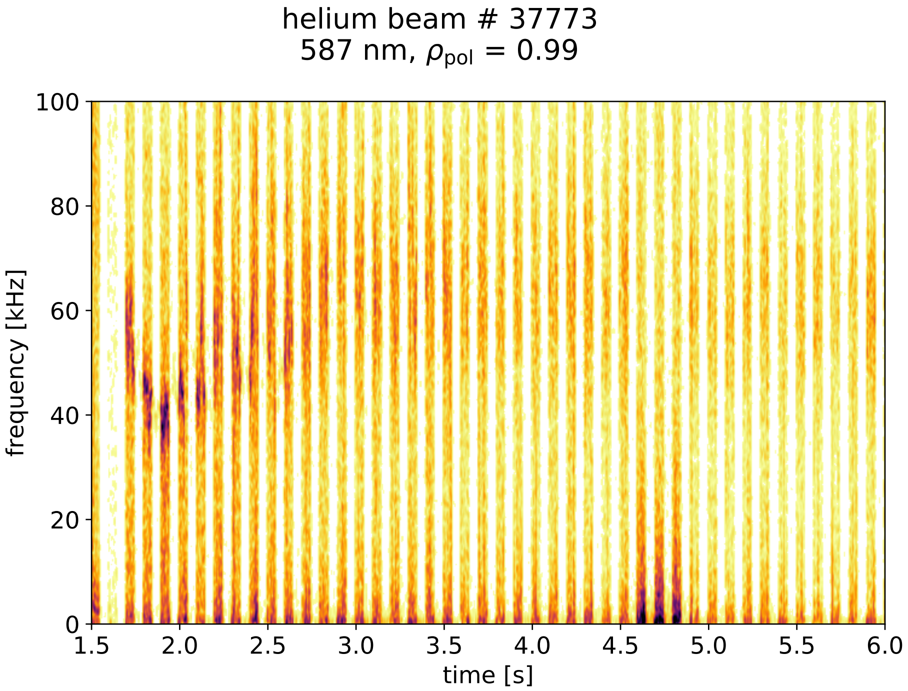

Figure 5.7.: Spectrogram of helium beam emissions in AUG discharge #37773 with a wave length of 587 nm from the channel observing $\rho_{\mathrm{pol}} = 0.99$. The vertical stripes come from the chopping of the helium beam. Between 4.5 s and 4.9 s the observed location changes due to a strike line scan.

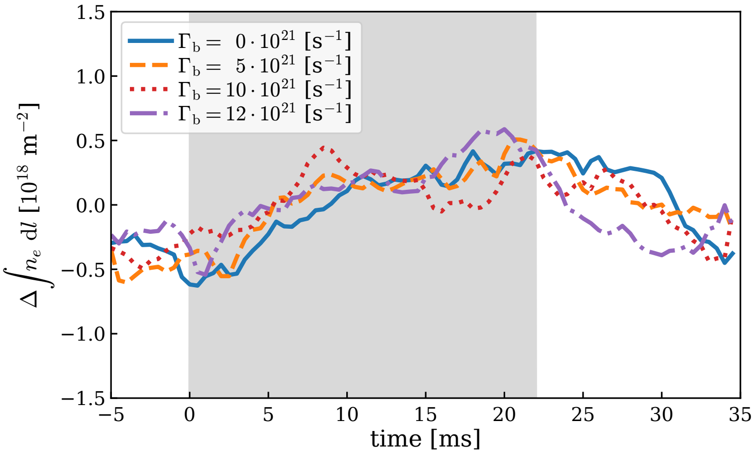

Figure 5.8.: The conditionally averaged time traces of edge interferometer H-5 for four different background fuelling levels in H-mode #37773 with ECR heating of 1.8 MW. The modulation valve is open only in the grey shaded area.

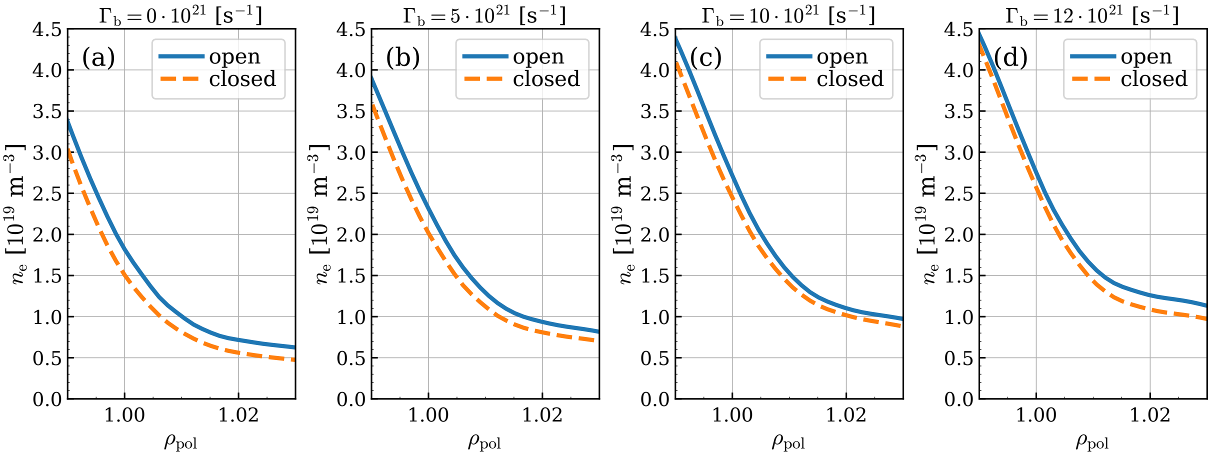

Figure 5.9.: Lithium beam profiles for four different background fuelling levels in H-mode #37773 with ECR heating of 1.8 MW, each for open and closed modulation valve.

section. The QCM vanishes around 2.7 s. The first segment in the discharge is classified as an EDA H-mode.

The edge interferometry (figure 5.8) responds similarly to the fuelling modulation in all four cases. The absolute change in line integrated density is $\approx 1 \times 10^{18}\,\mathrm{m}^{-2}$ in all cases. As before the density increases with increased fuelling, where the EDA H-mode (no background fuelling) reacts the slowest and the case with $\Gamma_\mathrm{b} = 12 \times 10^{21}\,\mathrm{s}^{-1}$ the fastest.

With an increasing background fuelling flow the edge density increases (figure 5.9). In all cases the separatrix density increases when the modulation valve is opened, with the low fuelling cases responding weaker to the modulation: for the $\Gamma_\mathrm{b} = 0\,\mathrm{s}^{-1}$ (figure 5.9a) the difference is

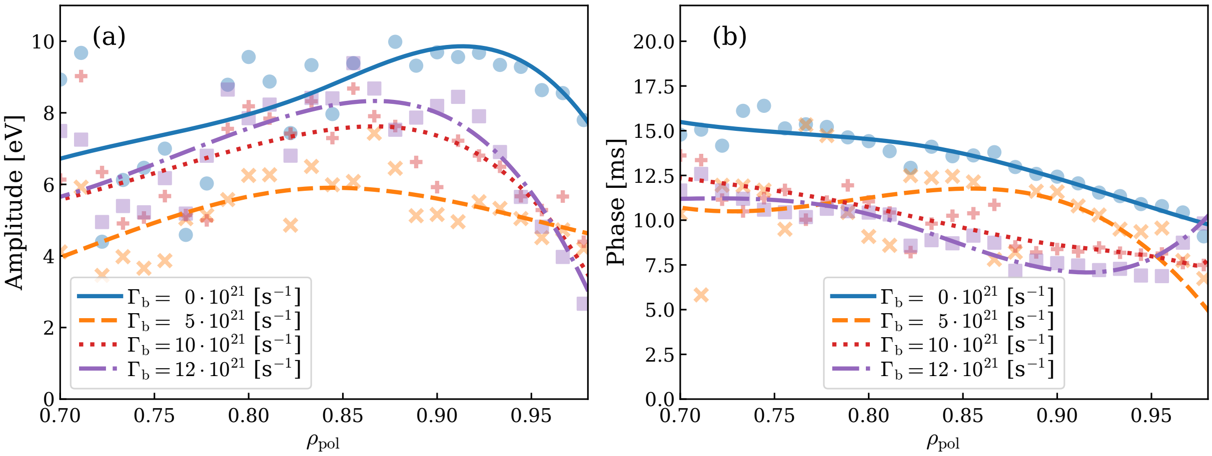

Figure 5.10.: Modulation amplitude (a) and phase (b) of the electron temperature for four different background fuelling levels in H-mode #37773 with ECR heating of 1.8 MW. A positive phase corresponds to a delay with respect to the valve action. Both experimental data from ECE (symbols) and fits (lines) are shown. A phase shift of 0 would refer to a maximum cooling rate directly when the valve opens, positive phase shifts refer to a delayed cooling.

$3 \times 10^{18}\,\mathrm{m}^{-3}$, while for $\Gamma_\mathrm{b} = 12 \times 10^{21}\,\mathrm{s}^{-1}$ (figure 5.9d) the difference is $2 \times 10^{18}\,\mathrm{m}^{-3}$. The separatrix density gradient remains unaltered within the experimental uncertainties.

A cold pulse propagates in all cases. For the EDA H-mode with $\Gamma_\mathrm{b} = 0\,\mathrm{s}^{-1}$ (solid blue line in figure 5.10a) the cold pulse shows the highest maximum amplitude of 10 eV and the largest phase delay with 10 ms at $\rho_\mathrm{pol} = 0.98$ (solid blue line in figure 5.10b). For the three more strongly fuelled cases without a QCM, trends are visible: the amplitude of the three cases peaks around $\rho_\mathrm{pol} = 0.85$ compared to $\rho_\mathrm{pol} = 0.91$ for the EDA H-mode. Higher background fuelling coincides with a larger amplitude and less delay of the cold pulse. It was previously discussed that the density response of the higher fuelling cases is less pronounced than for the low fuelling cases. From the increased cold pulse amplitude, it can be concluded that this is not because of a reduced fuelling efficiency and therefore a reduced perturbation of the plasma, because the electron temperature is influenced even stronger. When modelling the discharges later it is found that indeed electron heat transport increases more strongly in the high fuelling cases. If the particle transport responds analogously this suggests that the reduced increase in density is because the fuelled particles are flushed more effectively from the pedestal in the higher fuelling cases due to the larger increase in transport. Section 5.3.3 will discuss the implications of the altered transport on the density response in more depth.

5.1.4. QCE Discharges with LFS and HFS Fuelling

The last two cases for which a transport analysis will be conducted are the two AUG QCE discharges #37774 and #37871 at 6.6–7.35 s and 6.6–7.6 s, respectively. As usual for QCE discharges, the plasmas are strongly shaped with a triangularity of 0.38 and an elongation of

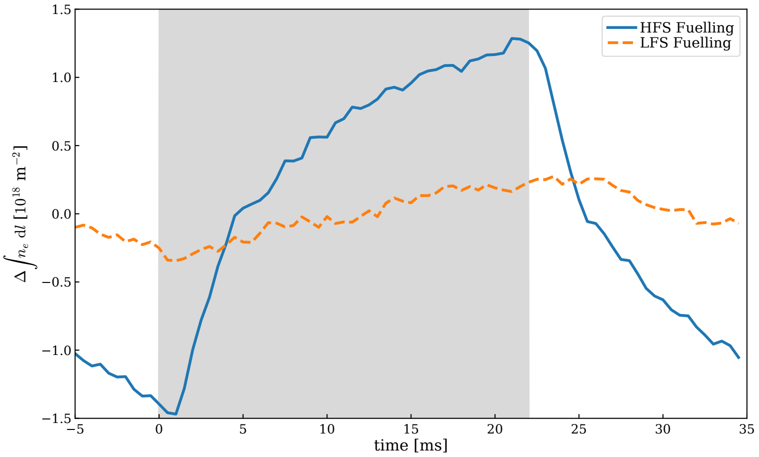

Figure 5.11.: The conditionally averaged time traces of edge interferometer H-5 for QCE discharges with HFS (#37774) and LFS (#37871) fuelling. The valve is open only in the grey shaded area.

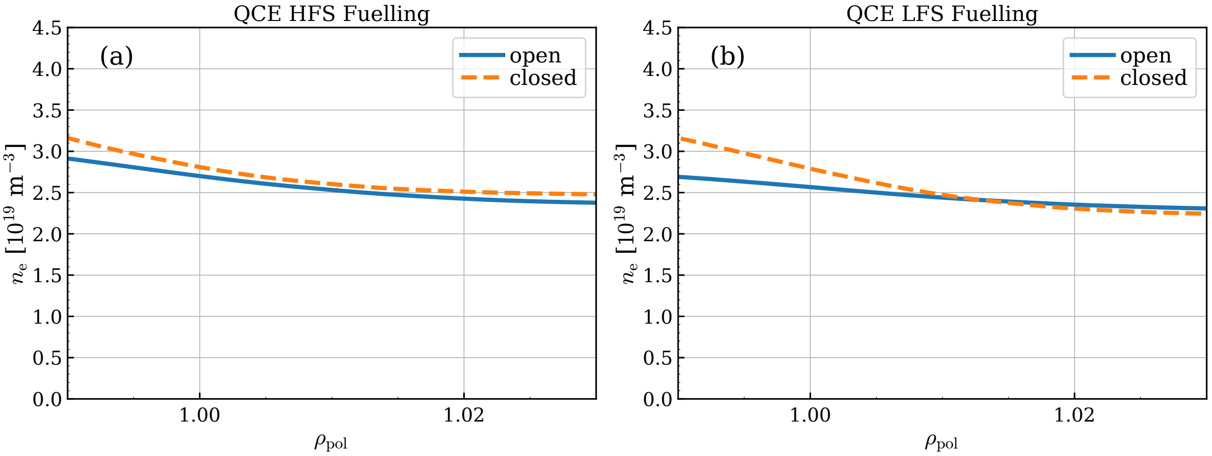

Figure 5.12.: Lithium beam profiles for QCE discharges with HFS (#37774) and LFS (#37871) fuelling, each for open and closed modulation valve.

1.64. Fuelling occurs exclusively through the fast acting valves used for the modulation. The two discharges differ only in the fuelling location: #37774 is fuelled from the HFS while #37871 is fuelled from the LFS. As before the maximum particle flow is $8 \times 10^{21}\,\mathrm{D\,s^{-1}}$ with a 55 % duty cycle. The plasma current is $I_{\mathrm{P}} = 600\,\mathrm{kA}$ and the toroidal magnetic field $B_{\mathrm{t}} = -2.44\,\mathrm{T}$. The plasma is heated by 5 MW NBI and 2.8 MW ECR.

Edge interferometry (figure 5.11) shows drastic differences between the discharges. With HFS fuelling, the edge density rises quickly 1 ms after the valve opens. The density rise slows around 5 ms and continues until the valve closes at 22 ms. After the valve is closed the density drops quickly until 25 ms and slower thereafter. The line integrated density changes by $2.8 \times 10^{18}\,\mathrm{m^{-2}}$ during the modulation period. With LFS fuelling, the density reacts much weaker but qualitatively similar. The absolute change in line integrated density is merely $0.6 \times 10^{18}\,\mathrm{m^{-2}}$, and the density declines at 26 ms with a delay of 4 ms to the valve closing.

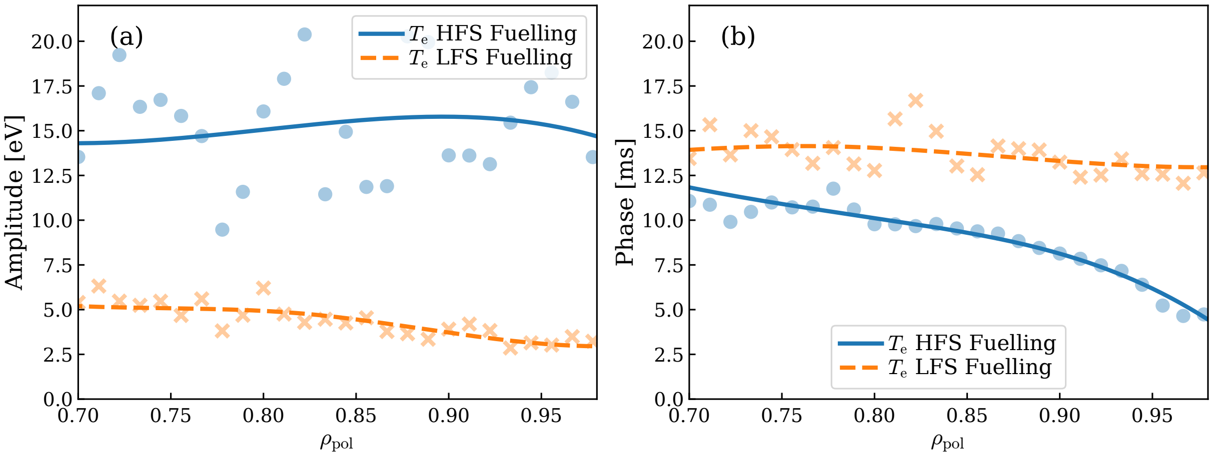

Figure 5.13.: Modulation amplitude (a) and phase (b) of the electron temperature for QCE discharges with HFS (#37774) and LFS (#37871) fuelling. A positive phase corresponds to a delay with respect to the valve action. Both experimental data from ECE (symbols) and fits (lines) are shown. A phase shift of 0 would refer to a maximum cooling rate directly when the valve opens, positive phase shifts refer to a delayed cooling.

The edge density (figure 5.12) remains above $2 \times 10^{19}\,\mathrm{m}^{-3}$ even far from the separatrix, a phenomenon known as density shoulder [Car17, Via17]. At the separatrix the density and the density gradient are reduced in both cases, but stronger when fuelling from the LFS. With HFS (LFS) fuelling, the density at the separatrix *de*creases by $1.1 \times 10^{18}\,\mathrm{m}^{-3}$ ($2.2 \times 10^{18}\,\mathrm{m}^{-3}$) and the gradient thereof reduces by $30\,\%$ ($60\,\%$).

Discrepancies between the two discharges also appear in the cold pulse propagation (figure 5.13). With HFS fuelling (solid blue line) the amplitude is comparably large with value between 12.5 eV and 15 eV outside of $\rho_{pol} = 0.70$. The phase is comparable to the discharges discussed previously with a delay of 5 ms at $\rho_{pol} = 0.98$ which grows to 12 ms at $\rho_{pol} = 0.70$. With LFS fuelling T_e behaves very differently: the amplitude is merely 3 eV in the pedestal and grows to 5 eV at $\rho_{pol} = 0.70$. Cooling starts strongly delayed 13 ms after the valve is opened and propagates with no reliably measurable delay to $\rho_{pol} = 0.70$: the whole region cools simultaneously.

Outside of $\rho_{pol} = 0.9$, CXRS ion temperature data is available in addition to the electron temperatures measured by ECE for the case with HFS fuelling. A cooling also in the ion channel can be observed, with an amplitude of up to ±9 eV it is smaller than the 15 eV in the electron channel. The cold pulse in the ion temperature appears delayed with respect to the electron temperature, this discrepancy is however within the scatter of the experimental data for most radii.

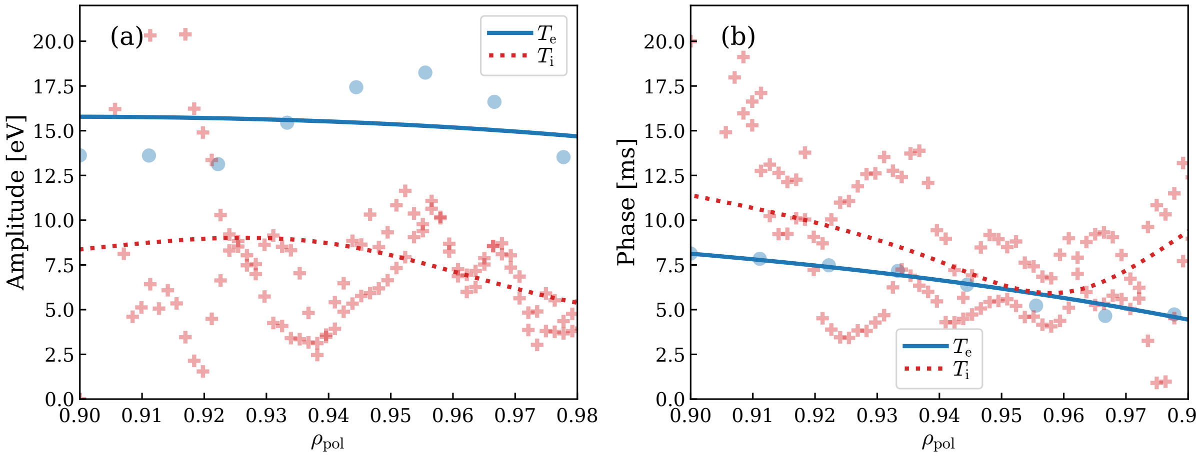

Figure 5.14.: Modulation amplitude (a) and phase (b) of electron (solid blue) and ion (dotted red) temperature for the QCE discharge with HFS fuelling (#37774). A positive phase corresponds to a delay with respect to the valve action. Both experimental data from CXRS (symbols) and fits (lines) are shown. A phase shift of 0 would refer to a maximum cooling rate directly when the valve opens, positive phase shifts refer to a delayed cooling.

5.1.5. I-Phase

The first discharge for which the response of the plasma to the gas puff modulation was analyzed, and with which the analysis model was initially developed, was discharge #36599 from 5.3 s to 5.6 s. A transport analysis for this case will however not be shown because the experimental data shows effects detrimental to this application.

#36599 is a discharge with a plasma current of 1 MA and a toroidal magnetic field of −2.5 T. The heating in the investigated phase is due to 500 kW ECRH. However, earlier in the discharge the heating power was higher, resulting in a transition into an ELMy H-mode. With the drop in heating power, the plasma transitioned into an I-phase, a regime with reduced turbulent edge transport and intermittent relaxation events [Réf20].

Figure 5.15 shows all five DCN interferometry time traces for this discharge. First, consider the edge channels H-4 and H-5. The modulation amplitude is small, comparable to the H-mode cases with 1.8 MW of ECRH in #37773. Previous cases featured an initially steep density increase, followed by a slower rise until the maximum is reached when the valve is closed again. Here, H-4 and H-5 increase comparably fast in two steps from 0 ms to 10 ms and 15 ms to 20 ms. Due to the short time window there is a comparably large amount of noise on the signal.

The core channels H-0, H-1 and H-2 appear strongly delayed compared to the edge channels. In section 4.1.1 and figure 4.4 H-1 and H-5 were compared for the first L-mode case. The core channel was not delayed compared to the edge channel. In L-mode, the density modulation responsible for the modulation measured by interferometry is poloidally symmetric and located in the edge: when scaling H-5 according to these assumptions, good agreement with the exper-

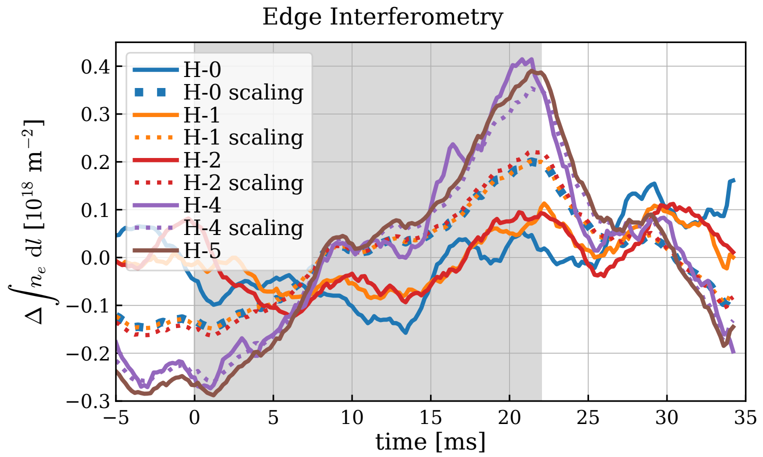

Figure 5.15.: Time traces from DCN interferometry. With the assumption that the density modulation is located between $\rho_{\mathrm{pol}} = 0.9$ and $\rho_{\mathrm{pol}} = 1.0$ and uniform one can compute the time traces for channels H-0, H-1, H-2 and H-4 given H-5. These scaled time traces are shown as dotted lines. In the gray shaded area the fuelling valve is open.

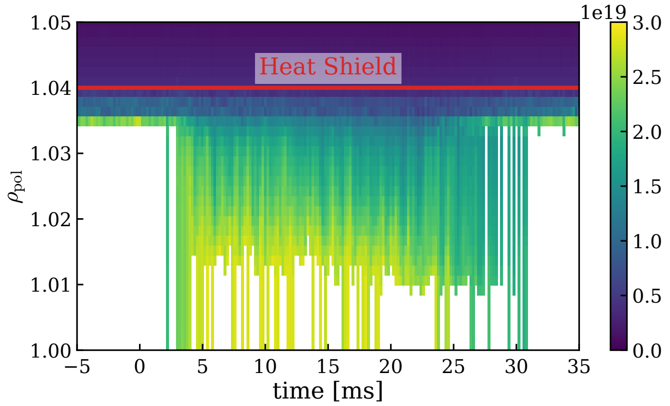

Figure 5.16.: The electron density on the HFS as measured by reflectometry. White areas are not resolvable with reflectometry because of the cutoff density of $3 \times 10^{19}\ \mathrm{m}^{-3}$. The wall location on the HFS at $\rho_{\mathrm{pol}} = 1.04$ is marked as red line. The fuelling valve is open between 0 ms and 22 ms.

imentally measured signal for H-1 is obtained. For the I-phase this is not the case. The scaled H-5 signals, i.e. the predictions for the other channels, are shown as dotted lines in figure 5.15. The measured modulation in the core channels is delayed by more than 10 ms compared to the predictions from a poloidally symmetric edge modulation.

The developed ASTRA model is not able to reproduce all interferometry time traces simultaneously. One reason for the inability of the model to reproduce the experimental data is the assumption of poloidal symmetry in the SOL. Figure 5.16 shows the density as measured by reflectometry in the SOL on the HFS. The cutoff density is $3 \times 10^{19}\ \mathrm{m}^{-3}$. Before the valve is opened the cutoff density is already reached at $\rho_{\mathrm{pol}} \approx 1.035$, which is never the case in the LFS SOL, not even with the density shoulder in the QCE cases. 3 ms after the valve is opened the

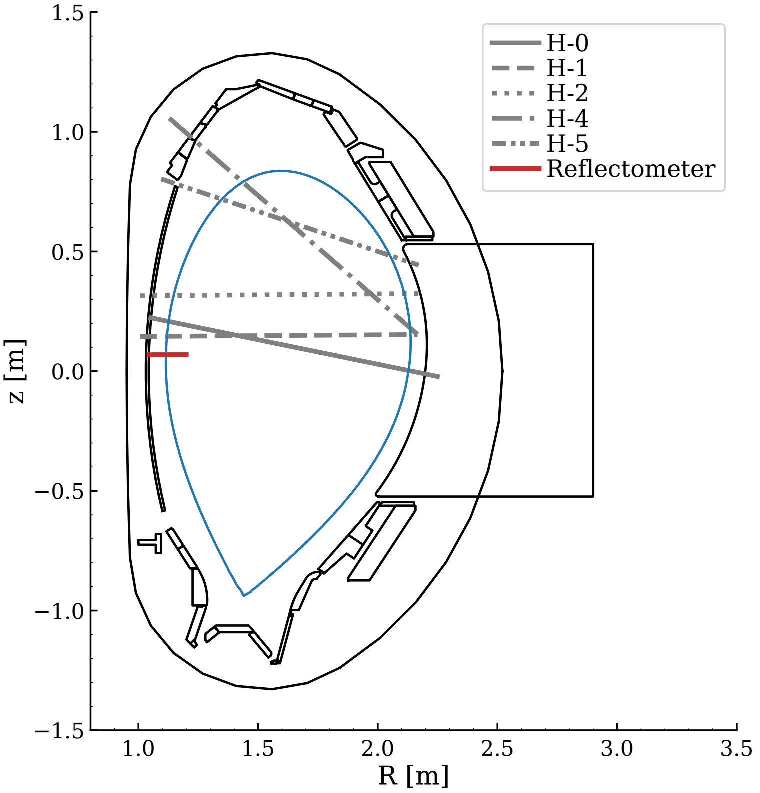

Figure 5.17.: Poloidal projection of ASDEX Upgrade with separatrix (solid blue line), lines of integration for the DCN interferometer (grey lines), and the HFS reflectometer (solid red line).

SOL density declines, and the cutoff density is reached only at $\rho_\mathrm{pol} \approx 1.015$. The SOL density then continues to decline until ≈ 25 ms, with the cutoff density moving to $\rho_\mathrm{pol} \approx 1.010$. At this time, shortly after the valve has been closed, the density at $\rho_\mathrm{pol} = 1.035$ begins to increase again, reaching the cutoff at 28 ms. In summary the HFS SOL density is *de*creased by fuelling.

In the HFS SOL the density can be much higher than on the LFS. The reason for this are drifts in the divertor [Rei17]. Usually, the outer divertor is hotter than the inner divertor, coinciding with a higher plasma potential. The resulting electric fields cause drifts, i.e. convection of particles in the divertor to the HFS. A possible explanation for the reduction of the HFS SOL density due to fuelling is the following: when the fuelling valve is open, the outer divertor cools, reducing the electric field and the drift velocity. Therefore the particle flux to the HFS is reduced, resulting in a lower plasma density.

Figure 5.17 shows the position of the HFS reflectometer and the lines along which the interferometer integrates the density. All integration lines lie in the R-z plane and originate at the LFS midplane. The edge channels H-4 and H-5 pass the plasma in the upper region and traverse the HFS SOL close to the top of the plasma. The core channels H-0, H-1 and H-2 on the other hand pass the plasma almost horizontally, crossing the HFS SOL close to the midplane where also the reflectometer is located. Although accurately quantifying the HFS SOL density is difficult due to the reached cutoff, one can estimate the density reduction due to fuelling to be at least $1 \times 10^{19}\,\mathrm{m}^{-3}$, an order of magnitude above the density increases observed at the LFS. Integrated over $\approx 4\,\mathrm{cm}$ this gives $\approx 4 \times 10^{17}\,\mathrm{m}^{-2}$, which is more than the modulation amplitude of the core DCN channels.

DCN interferometry is therefore strongly influenced, if not dominated, by the modulation of the high density at the HFS. Because the modulation cannot be quantified sufficiently one cannot rely on interferometry to study the density response in this discharge. This discharge will therefore not be discussed any further.

5.2. Heat Transport

Using the experimental data presented in the previous section one can model the discharge with ASTRA as presented in chapter 4. As an addition also the density gradient at the separatrix is fitted. One minor change concerns the parametrization of the prescribed profiles: for the cases which are not in L-mode, $\rho_{\mathrm{pol}} = 0.97$ is used instead of $\rho_{\mathrm{pol}} = 0.95$ as new boundary where the piece-wise constant profiles are allowed to change to reflect the narrower steep gradient region. First, the electron heat transport will be discussed as it does only depend on the measured temperature and density, which are much more accurately determined than the particle source and the particle transport. After a comparison of electron and ion heat diffusivities the chapter will continue with particle transport and fuelling.

5.2.1. Electron Heat Transport in the Pedestal Region

The first discussed result is the electron heat diffusivity χ_{e} in the steep gradient region as a function of time, which is shown in figure 5.18. This section mainly focuses on relative changes of χ_{e} because the absolute value is comparably uncertain: T_{i} is available only for one case, in the other cases it is not known how heat transport is shared between ions and electrons. As we will discuss in section 5.2.3 the lack of T_{i} measurements does not affect any conclusions drawn from the relative changes of heat transport.

In the investigated scenarios, opening the fuelling valve generally leads to an increase in χ_{e}. Figure 5.18a shows the L-mode cases, with the solid blue line for no background fuelling being the increase in transport discussed already in chapter 4. With increasing fuelling (dashed orange line) χ_{e} reacts weaker but quicker. The highest fuelling level (red dotted line) is similar to the case without background fuelling, but transport increases slightly earlier.

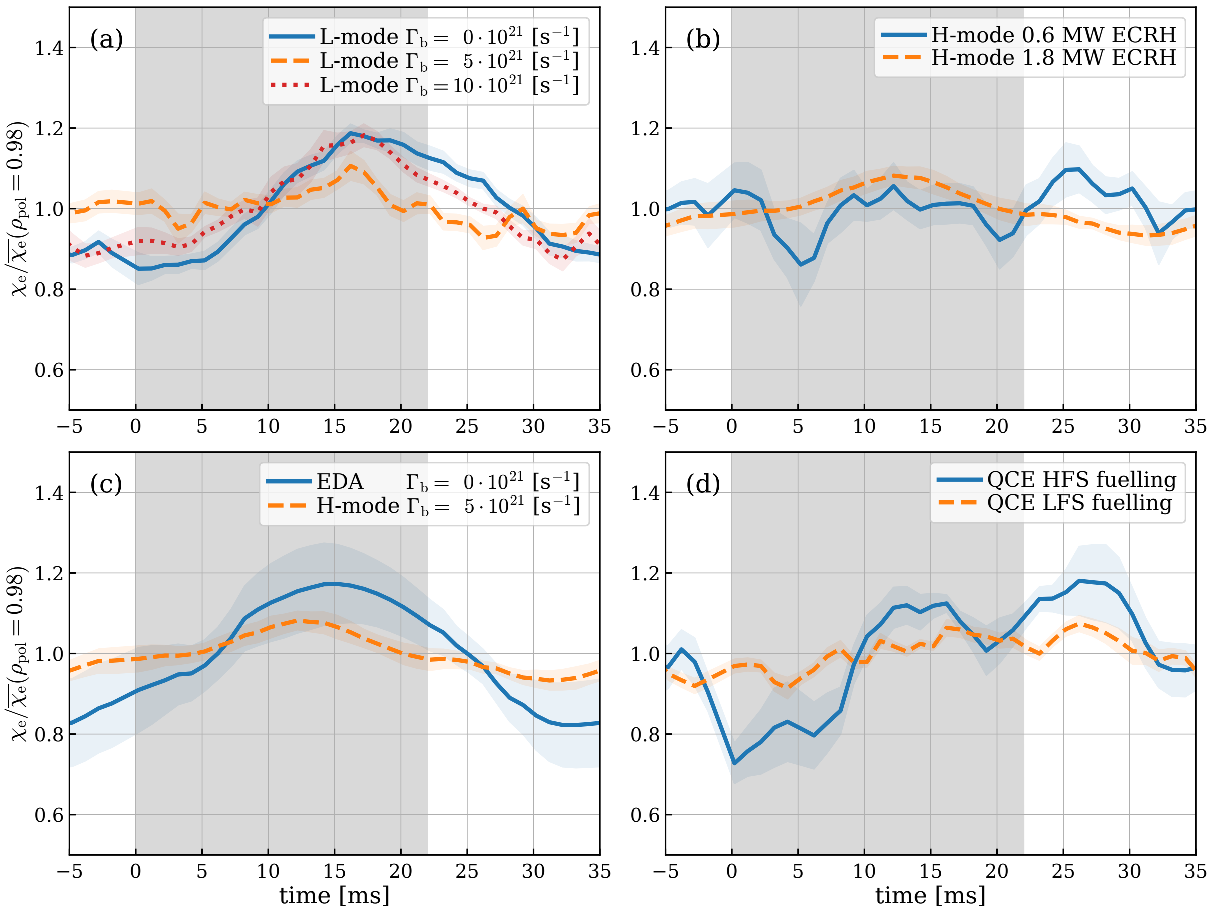

Figure 5.18.: The electron heat diffusivity χ_e at $\rho_{pol} = 0.98$ as a function of time normalized to the mean value. Lines are the point-wise median of all successful fits, and the shaded areas the corresponding uncertainties (one sigma). In panel (c) the individual lines show less noise because additional filtering of the density boundary condition is necessary. The modulation valve is open only in the grey shaded area.

The two H-mode phases with different amounts of heating (figure 5.18b) behave dissimilar. With 0.6 MW of ECRH (blue solid line) transport does not increase with increased fuelling. When the valve is opened at 0 ms, transport appears to *de*crease for ≈ 4 ms and increases after the valve is closed. It is not clear if this effect is statistically significant. The case with 1.8 MW of ECRH (dashed orange line), which uses the same amount of background fuelling $\Gamma_b = 5 \times 10^{21}\,\mathrm{s}^{-1}$, on the other hand behaves very similar to the L-mode discharge with the same fuelling flux in figure 5.18a: a moderate increase in transport occurs after the valve was opened.

Figure 5.18c shows χ_e for different fuelling levels in H-mode. The heat diffusivity in the EDA H-mode (blue solid line) modulates with comparable amplitude to the L-mode with identical fuelling flux (blue solid line in figure 5.18a), albeit it reacts several millisecond faster to the increase in fuelling. The $\Gamma_b = 5 \times 10^{21}\,\mathrm{s}^{-1}$ case (orange dashed line), which was already discussed in panel (b), shows a weaker and quicker modulation of χ_e.

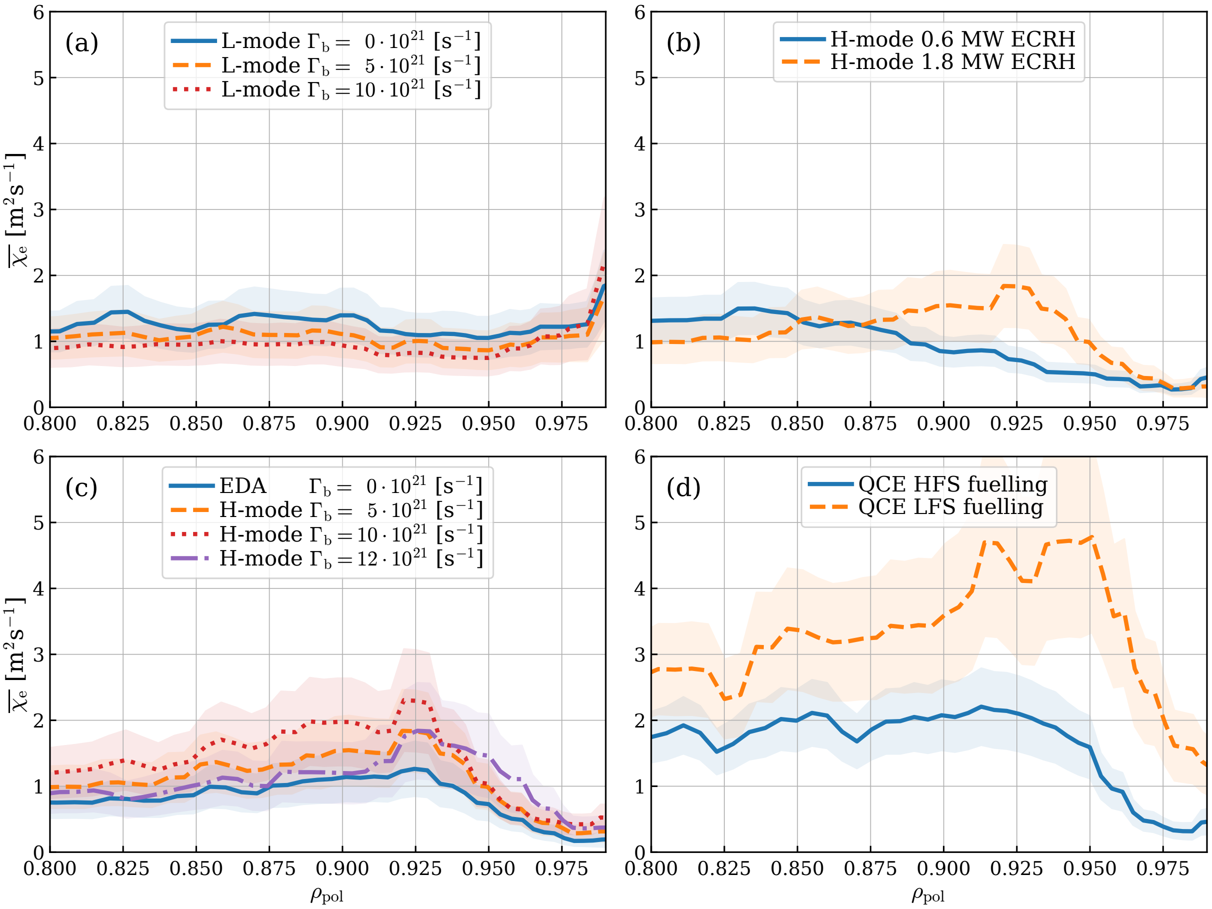

Figure 5.19.: Temporally averaged electron heat diffusivities χ_e for all considered cases as a function of normalized radius. Lines are the point-wise median of all successful fits, and the shaded areas the corresponding uncertainties (one sigma).

The QCE cases are shown in figure 5.18d. With HFS fuelling (blue solid line) χ_e is smallest exactly when the valve opens at 0 ms. At 8 ms transport increases and remains high until $\approx$ 30 ms. χ_e then returns to the low values when the valve opens. Around 20 ms transport decreases slightly but the statistical significance is questionable. χ_e reacts far weaker when fuelling from the LFS: it is higher between 10 ms and 30 ms than between 30 ms and 50 ms = 10 ms. This difference is consistent with the behavior of the HFS-fuelling case. A more detailed analysis is difficult due to the unfavorable signal-to-noise ratio.

5.2.2. Heat Transport Inwards of the Pedestal

Figure 5.19 shows the χ_e profiles (temporally averaged), obtained using ASTRA, for all considered cases. In all cases, except for the L-modes in panel (a), the edge transport barrier is visible as a reduction of χ_e in the pedestal region. For the QCE with LFS fuelling (orange dashed line) one obtains a χ_e which is twice as large as for HFS fuelling (blue solid line) outside of

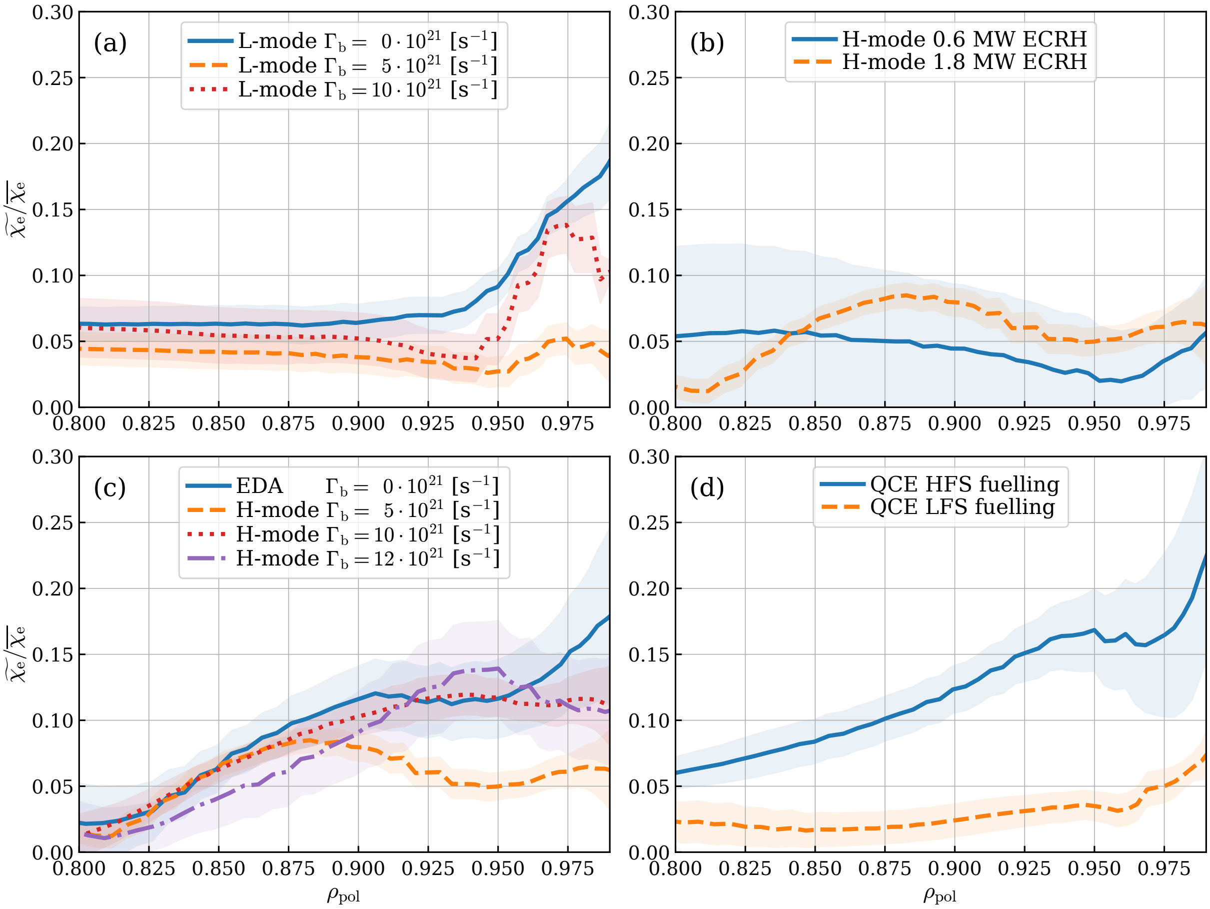

Figure 5.20.: Amplitudes of the electron heat diffusivity χ_e modulation, normalized by the mean χ_e (shown in figure 5.19), for all considered cases as a function of normalized radius. Lines are the point-wise median of all successful fits, and the shaded areas the corresponding uncertainties (one sigma).

$\rho_{pol} = 0.9$. This large difference for the two similar discharges is a simulation artifact coming from the missing ion temperatures in the LFS case, but as will be discussed in section 5.2.3, this does not corrupt any conclusions drawn in this thesis.

As discussed in section 5.2.1, the heat transport coefficients change with the fuelling modulation. The relative amplitude of the χ_e modulation is shown in figure 5.20. For L-modes, figure 5.20a, the modulation is restricted to the pedestal: χ_e modulates only weakly inside of $\rho_{pol} = 0.95$. The amplitudes for $\Gamma_b = 0\,\mathrm{s}^{-1}$ and $\Gamma_b = 10 \times 10^{21}\,\mathrm{s}^{-1}$ are similar, while the case with $\Gamma_b = 5 \times 10^{21}\,\mathrm{s}^{-1}$ shows only small changes of χ_e. Figure 5.21a shows the corresponding phase of the modulation: inside the pedestal the cases $\Gamma_b = 0\,\mathrm{s}^{-1}$ and $\Gamma_b = 10 \times 10^{21}\,\mathrm{s}^{-1}$ have a similar phase of 8 ms, while the case with $\Gamma_b = 5 \times 10^{21}\,\mathrm{s}^{-1}$ has a phase of 3 ms. Inside of the pedestal the phases differ, but the small amplitude makes the determination of the phase error prone.

The analysis continues with the H-mode cases. In the case with only 0.6 MW of ECRH (solid blue line in figures 5.20b and 5.21b) the modulation amplitude is smaller than in the other H-mode cases, and the uncertainties of amplitude and phase are large. For the H-modes with

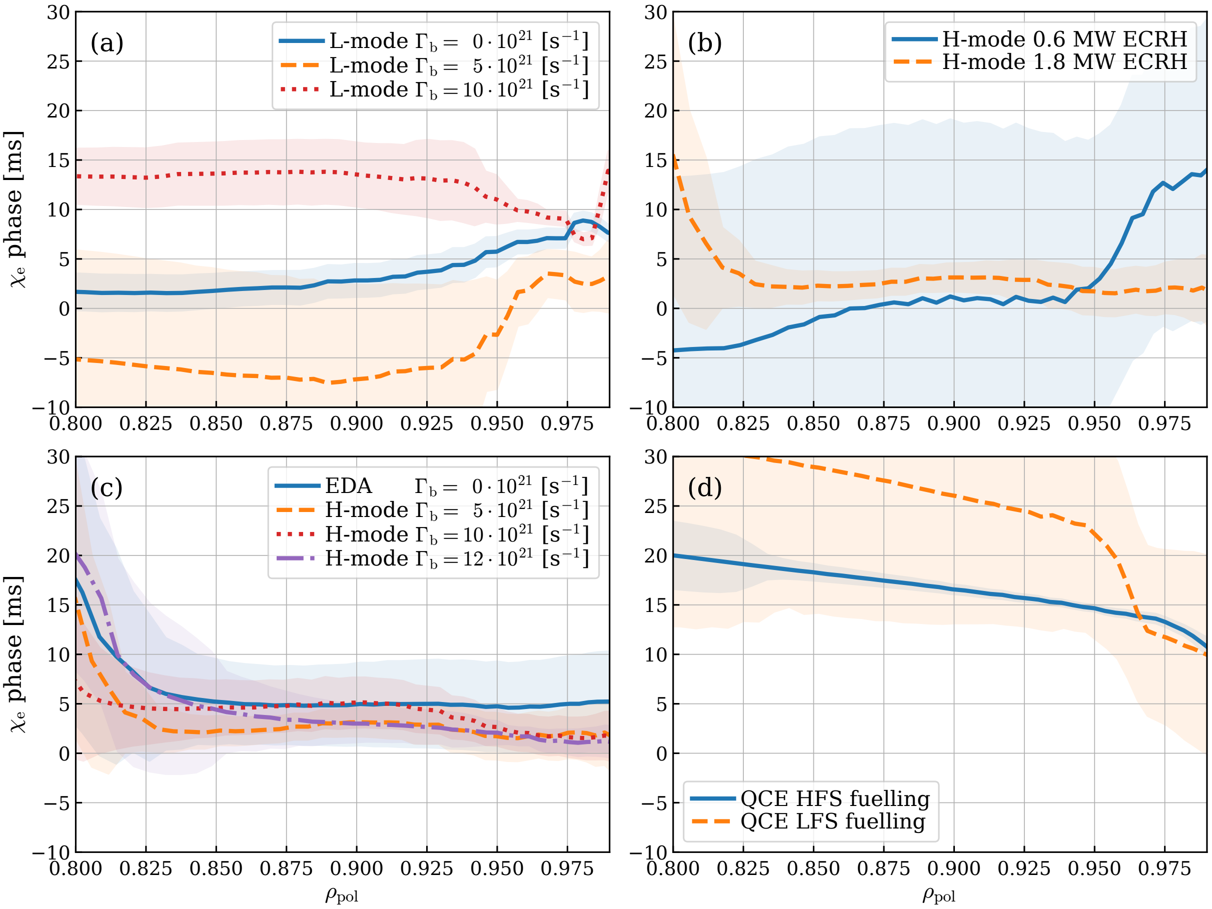

Figure 5.21.: Phases of the electron heat diffusivity χ_e modulation for all considered cases as a function of normalized radius. Lines are the point-wise median of all successful fits, and the shaded areas the corresponding uncertainties (one sigma).

1.8 MW of ECRH (figures 5.20c), the modulation amplitudes found in the pedestal are similar to the L-mode cases. The amplitude however remains large until after $\approx \rho_{pol} = 0.9$. The H-modes with background fuelling react quickly to the opening of the valve with a phase delay of 1–2 ms (5.21c) before transport increases. The EDA H-modes reacts slightly delayed with a phase of 5 ms. Going inwards the phase delay remains between 0 ms and 10 ms until $\rho_{pol} = 0.85$. To summarize, for the presented H-mode cases, χ_e increases from the separatrix to $\rho_{pol} = 0.85$ almost instantly when we open the valve.

The final scenario is the QCE. The relative amplitude of the χ_e modulation (figure 5.20d) is only small for LFS fuelling (orange dashed line), but large for HFS fuelling (solid blue line). For HFS fuelling the amplitude remains large also for smaller radii, similar to the H-mode cases. Considering the phase with HFS fuelling (solid blue line in figure 5.21d) one observes a comparably large delay of 10 ms until transport rises in the pedestal, and even longer delays further inside the plasma: inward of $\rho_{pol} = 0.95$ the phase delay is larger than 15 ms, constituting more than a 90° phase shift compared to the H-mode cases. The uncertainty of the phase

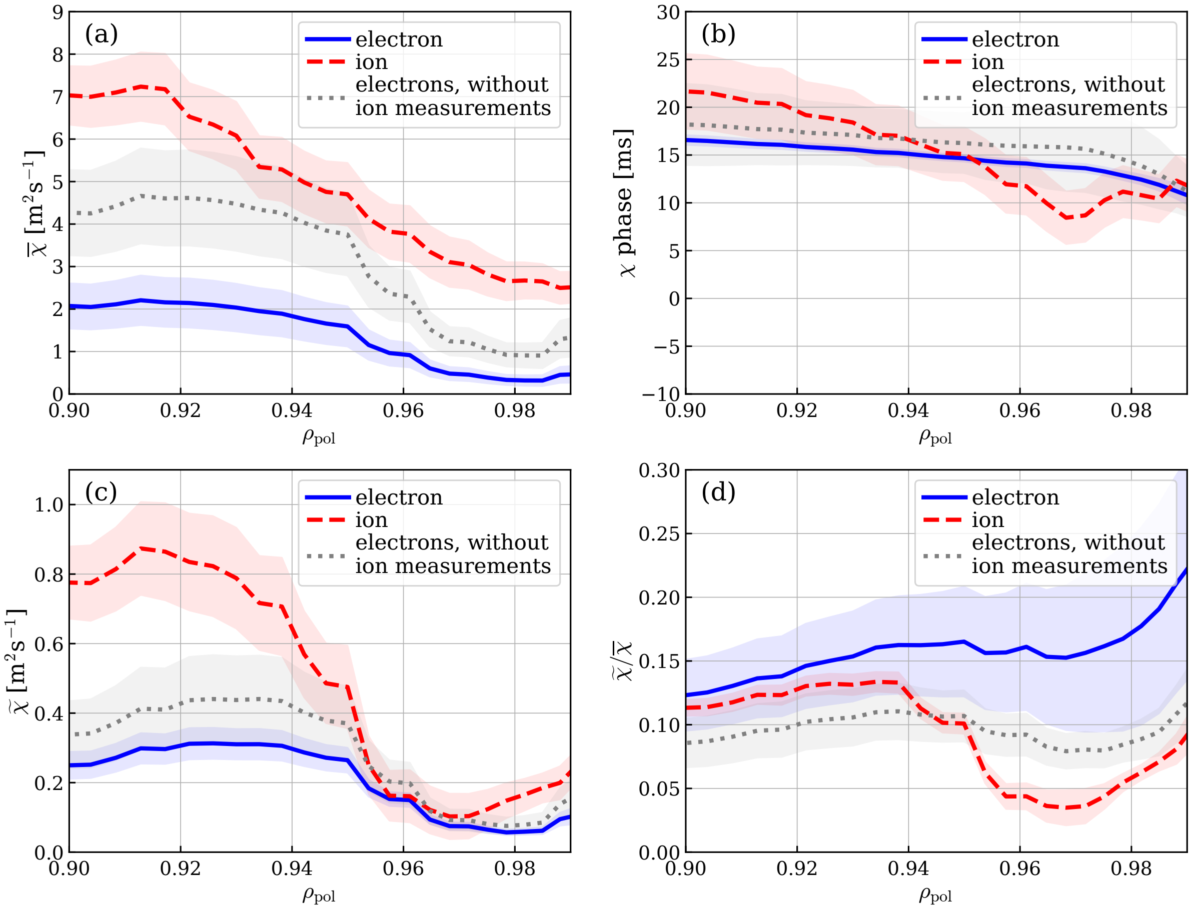

Figure 5.22.: Comparison of χ_e (blue solid line) and χ_i (red dashed line) for AUG discharge #37774 (QCE with HFS fuelling). Shaded areas show the one-sigma statistical uncertainties of the reconstructed values. Shown are the temporally averaged heat diffusivities (a), the phase of the modulation (b), the absolute amplitude of the modulation (c), and the relative amplitude of the modulation (d).

modulation is small. One effect that improves the accuracy is the availability of ion temperature data. In the pedestal for the case with LFS fuelling (dashed orange line) χ_e modulates with a similar phase, but the uncertainty is much larger due to the weaker modulation amplitude and the missing T_i data. Inside of the pedestal the phase, which is less reliable due to the very small amplitude, is larger than for the HFS fuelling case.

5.2.3. Electron and Ion Transport Channels

The two QCE discharges under investigation (#37774 and #37871) are heated by NBI, allowing the measurement of ion temperatures using CXRS (section 3.5). When fuelling on the LFS (#37871) the spectroscopic measurements are corrupted by molecular emissions. In this section therefore only the case with HFS fuelling (#37774) is discussed. For the analysis in this section we prescribe the ion temperature. Figure 5.22 also shows the analysis of χ_e with (blue solid lines) and without prescribed ion temperature (grey dotted lines) as it is performed for all other cases in this thesis. At the end of the section it will be discussed that the lacking ion temperatures do not endanger the conclusions.

Figure 5.22a shows the temporally averaged profiles of χ_e (blue solid line) and χ_i (red dashed line) in the radial range where reliable and well-resolved measurements of T_e and T_i profiles are available. χ_i is larger than χ_e at all locations by a factor of more than 2. Diffusivity in both transport channels declines with increasing radius. At and outside of $\rho_\mathrm{pol} = 0.97$ χ_e drops below $0.5\,\mathrm{m^2\,s^{-1}}$.

The previous section discussed that χ_e changes due to the fuelling modulation. The same is true for χ_i. The phase of the modulation is shown in figure 5.22. The phase of χ_e shows less uncertainty than the phase of χ_i. In the pedestal both quantities modulate in phase. At $\rho_\mathrm{pol} = 0.97$ the ion channel reacts faster than the electron channel with a phase delay of $\approx 10\,\mathrm{ms}$ compared to $\approx 14\,\mathrm{ms}$, respectively. Travelling further inwards the phase of χ_i increases more quickly than the phase of χ_e. At $\rho_\mathrm{pol} = 0.9$, χ_i is delayed by $\approx 5\,\mathrm{ms}$ compared to χ_e.

Figure 5.22c shows the absolute amplitude of the modulation. Inside of $\rho_\mathrm{pol} = 0.93$, χ_i modulates by $\approx \pm 0.8\,\mathrm{m^2\,s^{-1}}$ compared to the $\approx \pm 0.3\,\mathrm{m^2\,s^{-1}}$ of χ_e. At $\rho_\mathrm{pol} = 0.96$ both quantities modulate by $0.15\,\mathrm{m^2\,s^{-1}}$. In the pedestal χ_i reacts once again stronger than χ_e in absolute numbers.

By dividing the absolute amplitudes (figure 5.22c) by the mean values (figure 5.22a) one obtains the relative amplitudes shown in figure 5.22d. Inside of $\rho_\mathrm{pol} = 0.94$ both heat diffusivities modulate with the, within the estimated uncertainties, same relative amplitude. Between $\rho_\mathrm{pol} = 0.94$ and $\rho_\mathrm{pol} = 0.97$ the relative amplitude in the ion channel drops from $\pm 13\,\%$ to $\pm 4\,\%$. χ_e remains at $\approx 16\,\%$ in the same radial range. Starting at $\rho_\mathrm{pol} = 0.97$ the relative amplitude grows in both channels until they reach $\approx 22\,\%$ (χ_e) and $\approx 9\,\%$ (χ_i).

Between $\rho_\mathrm{pol} = 0.90$ and 0.94 the heat diffusivities of ion and electron channels are proportional to each other because they modulate with the same relative amplitude and phases that are almost identical considering experimental uncertainties. The ratio of χ_i and χ_e depends on the radius: at $\rho_\mathrm{pol} = 0.90$ it is 1/4, at $\rho_\mathrm{pol} = 0.94$ it has increased to 1/2. The fact that the diffusivities are proportional to each other points to a single transport mechanism whose influence grows and shrinks over the course of a modulation period; the ratio suggests ion temperature gradient (ITG) modes or trapped electron modes (TEM) [Kot19], and it excludes magnetohydrodynamical (MHD) modes, micro-tearing modes (MTM) and electron temperature gradient (ETG) modes from having a significant contribution.

Further outside, the situation is more complicated. At the pedestal top, between $\rho_\mathrm{pol} = 0.95$ and 0.97, both diffusivities modulate with the same *absolute* amplitude. χ_i is however still much larger than χ_e, leading to a smaller relative modulation amplitude for χ_i than for χ_e. The transport channels are not proportional to each other. This suggests two different explanations. One is that different transport mechanisms are active at the same time and radius, differing in their ratio of χ_i and χ_e, and reacting differently to the altered conditions. Or one mechanism is at work, which changes from almost exclusively transporting heat in the ion channel to causing more heat transport in the electron channel as well. Apart from turbulence, neoclassical transport, which generally produces more ion than electron heat transport, certainly contributes. One interpretation would be that turbulence is mainly responsible for the modulation of the heat diffusivities, and neoclassics for the larger absolute χ_i. The identical absolute modulation amplitude would then point towards MHD-like modes [Kot19]. However, according to NEOCLASS [Hou97], the neoclassical χ_i is about a factor of 4 below the required $\approx 2.5\,\mathrm{m}^2\,\mathrm{s}^{-1}$: $\chi_\mathrm{i,neocl} \approx 0.6\,\mathrm{m}^2\,\mathrm{s}^{-1}$ and $\chi_\mathrm{e,neocl} \approx 0.02\,\mathrm{m}^2\,\mathrm{s}^{-1}$.

In the steep gradient region outside of $\rho_\mathrm{pol} = 0.97$, the situation is similar to the pedestal top, with the difference that the absolute modulation amplitude of χ_i grows larger than the absolute modulation amplitude of χ_e.

Without prescribed ion temperature and the model used for the other cases in this thesis, the grey dotted lines in figure 5.22 are obtained. The grey dotted line is always close to the lines for χ_e from the analysis with prescribed ion temperatures. The phase is virtually identical, and the relative modulation amplitude is reduced. The general behavior is identical, and conclusions drawn in this thesis are not invalidated by these differences. Therefore the assumption to set $\chi_\mathrm{i} \propto \chi_\mathrm{e}$ is not critical.

5.3. Particle Transport

In this section it will be discussed that not only the heat transport, but also the particle transport changes on a short time scale with fuelling changes. First, particle transport close to the separatrix will be discussed, where one can see an increased particle diffusivity directly in the density profiles. This observation is supported by the conducted ASTRA simulations. Then the question of the existence of a pinch is approached, and it will be discussed how the temporally changing transport makes the problem of determining convective transport underdetermined.

5.3.1. Flattening of the Density Gradient at the Separatrix

In all cases, the edge density as measured by the H-5 interferometer increases when fuelling is increased. Simultaneously, a flattening of the separatrix density gradient is observed in several discharges, namely in L-mode with no and low background fuelling and the QCE discharges (figures 5.2 and 5.12).

Intuitively, an increase in fuelling would be expected to coincide with an increase in the number of neutral atoms crossing the separatrix. An increased particle source also agrees well with the measured increase in pedestal top density. The developed ASTRA models, in which heat and particle transport are consistent with the measured data, also agree that the neutral flux is higher when the valve is open: figure 5.24 shows the ratio of the neutral particle flux across the separatrix when the valve is open and when the valve is closed. For all discharges with a flattening of the density gradient at the separatrix, the neutral particle flux is larger when the valve is open.

It will now be shown that the flattening of the density suggests an increase in particle diffusivity D. This, however, does not mean that D remains constant or is reduced in the cases where the separatrix density does not flatten: increased particle flux due to additional fuelling could cause steeper gradients even if D increases.

The density in the steep gradient region reaches steady state after a few millisecond. The particle transport equation (2.1) then becomes

$$0 = \frac{\partial}{\partial \rho}\left(D\frac{\partial n_\mathrm{e}}{\partial \rho} - v n_\mathrm{e}\right) + S_\mathrm{e}. \tag{5.1}$$

The for flattening necessary increase in D is more severe the stronger the source S_e grows with additional fuelling. To arrive at the minimally necessary change, $\Delta S_\mathrm{e} = 0$ is assumed, with Δ being the change from closed to open. Equation (5.1) then becomes

$$0 = \Delta\left[\frac{\partial}{\partial \rho}\left(D\frac{\partial n_\mathrm{e}}{\partial \rho} - v n_\mathrm{e}\right)\right] + \Delta\left[S_\mathrm{e}\right] \tag{5.2}$$

$$0 = \Delta\left[\frac{\partial}{\partial \rho}\left(D\frac{\partial n_\mathrm{e}}{\partial \rho} - v n_\mathrm{e}\right)\right] \tag{5.3}$$

$$0 = \frac{\partial}{\partial \rho}\left(\Delta\left[D\frac{\partial n_\mathrm{e}}{\partial \rho}\right] - \Delta\left[v n_\mathrm{e}\right]\right) \tag{5.4}$$

$$\Delta\left[D\frac{\partial n_\mathrm{e}}{\partial \rho}\right] = \Delta\left[v n_\mathrm{e}\right] + C, \tag{5.5}$$

with C being a radius independent number. At $\rho = 0$ the particle flux is 0, mandating $C = 0$, yielding

$$\Delta\left[D\frac{\partial n_\mathrm{e}}{\partial \rho}\right] = \Delta\left[v n_\mathrm{e}\right]. \tag{5.6}$$

Constant Particle Transport Coefficients If the particle transport coefficients are constant, equation (5.6) becomes

$$D\Delta\left[\frac{\partial n_\mathrm{e}}{\partial\rho}\right] = v\Delta\left[n_\mathrm{e}\right] \tag{5.7}$$

$$\frac{\Delta\left[\partial_\rho n_\mathrm{e}\right]}{\Delta\left[n_\mathrm{e}\right]} = \frac{v}{D}. \tag{5.8}$$

$\frac{\partial n_\mathrm{e}}{\partial\rho}$ is always negative in the pedestal region of the shown discharges. D is always positive. In the L-mode #37758, n_e rises and $\frac{\partial n_\mathrm{e}}{\partial\rho}$ becomes less negative, constituting a rise as well. Therefore outward convection (positive v) would be necessary.

In the QCE discharges, n_e drops instead. Therefore an inward convection, a pinch, would be necessary.

Purely Diffusive Particle Transport If we set $v = 0$, equation (5.6) becomes

$$\Delta\left[D\frac{\partial n_\mathrm{e}}{\partial\rho}\right] = D_\mathrm{open}\frac{\partial n_\mathrm{e,open}}{\partial\rho} - D_\mathrm{closed}\frac{\partial n_\mathrm{e,closed}}{\partial\rho} = 0 \tag{5.9}$$

$$\frac{D_\mathrm{open}}{D_\mathrm{closed}} = \frac{\partial_\rho n_\mathrm{e,closed}}{\partial_\rho n_\mathrm{e,open}} \tag{5.10}$$

The density profile is flattening in the considered discharges. Therefore D has to increase when the fuelling valve is opened.

5.3.2. ASTRA Modelling of the Particle Transport

With the ASTRA model presented in chapter 4, it is impossible to reproduce the flattening of the separatrix density in the L-mode case #37758: as discussed above, either D has to increase significantly or strong convective contributions are necessary. In chapter 4 it was assumed that the particle transport coefficients are uniform outside of $\rho_\mathrm{pol} = 0.95$. To reproduce the flattening of n_e, the transport coefficients are restricted to values that are incompatible with the requirement of reproducing the the density evolution further inside.

When one however restricts the region in which D and v modulate to outside of $\rho_\mathrm{pol} = 0.99$, the experiment can be reproduced

- if D is allowed to modulate,
- if D and v are allowed to modulate proportional to each other,

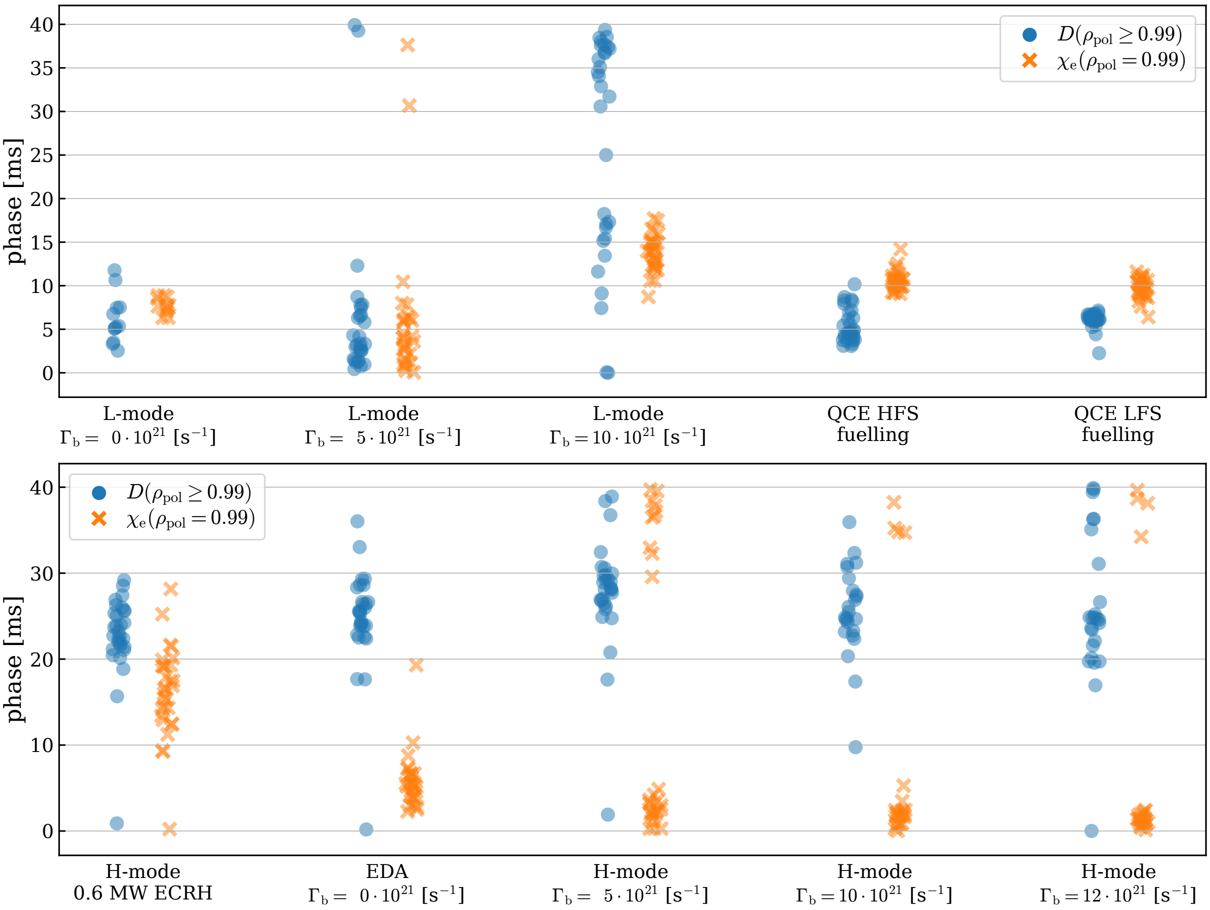

Figure 5.23.: The phase of the modulation of D (blue circles) and χ_e (orange crosses) in the vicinity of the separatrix. Each point corresponds to a successful ASTRA run.

- *not* if only v modulates.

We therefore conclude that D at the separatrix does *not* remain constant. It modulates more strongly close to the separatrix than inside, otherwise either the pedestal density cannot increase sufficiently or the separatrix density does not flatten.

To reproduce the evolution of the separatrix density gradient one has to treat the modulation of D as a free parameter that is fitted to the experimental data instead of fixing it as in chapter 4. Figure 5.23 shows the fitted phase of D and the phase of χ_e at $\rho_{\text{pol}} = 0.99$. For the L-mode case with no background fuelling ($\Gamma_b = 0\,\text{s}^{-1}$) the phase of χ_e is determined to be 6–9 ms. The predicted phase of D lies within a 10 ms interval centered at 7 ms. To conclude, D modulates, and it does so in phase with χ_e. With intermediate background fuelling ($\Gamma_b = 5 \times 10^{21}\,\text{s}^{-1}$) the phases of D and especially χ_e are less accurately determined. The median phase shift is less than for the case without additional fuelling, meaning that the increase of transport after the opening of the valve occurs more rapidly. The phases of D and χ_e are again identical withing the uncertainties. The case with high background fuelling ($\Gamma_b = 10 \times 10^{21}\,\text{s}^{-1}$) differs from the two previous cases in that the separatrix gradient becomes *steeper* instead of shallower when opening the modulation valve. In agreement with the argument from earlier in this section, D does not have to increase to combine the separatrix density gradient and the general increase of edge density. As a result good agreement with the experiment is possible with arbitrary phases of D, which is exactly the result of the ASTRA simulations shown in figure 5.23.

For the two QCE cases, the phases of both χ_e and D are very accurately determined with uncertainties between 5 ms to 8 ms. The different fuelling location does not influence the phases of χ_e and D. The predicted phase of D is 4 ms smaller than the phase of χ_e, corresponding to an earlier increase in particle transport than in electron heat diffusivity. This comparably small difference could be physical and for example show that transport at the separatrix reacts slightly faster than transport at $\rho_\mathrm{pol} = 0.99$.

The H-mode case with only 0.6 MW of ECRH shows phases of D and χ_e with uncertainties comparable to the L-mode case with the same additional fuelling of $5 \times 10^{21}\,\mathrm{s}^{-1}$. The phase of χ_e is delayed by 10 ms compared to the L-mode case, and the phase of D even by 20 ms. This is the largest difference between the phases of D and χ_e encountered so far. Similar to the L-mode case with high fuelling, the separatrix density *steepens* when the valve is opened, making changes in particle transport not as obvious. However, other than in the high fuelling L-mode case the results for the phase of D still cluster.

The other H-mode cases and the EDA case, all with 1.8 MW of ECRH, show large differences between the phases of D and χ_e. In all cases, the electron heat diffusivity increases quickly after the valve is opened, while recovered phases of D are generally less localized and the phases are shifted by half a period. In the next section this discrepancy is linked to an insufficient model of the particle transport.

The investigated cases fall into two categories: L-modes and QCE where it is found that χ_e and D modulate in phase, and the H-modes where differences are found between the phases of D and χ_e. The same separation occurs when considering the fuelling, selected by the optimization routine, for the models such that they reproduce the experiment. Figure 5.24 shows the ratio of neutral particle fluxes across the separatrix for the open and closed valve. A value greater than 1 corresponds to more neutral particles crossing the separatrix when the valve is open than when the valve is closed. In the top panel, which contains the cases with in-phase modulation of D and χ_e, the increase in fuelling leads to more neutral particles crossing the separatrix and therefore a larger source in the pedestal. For the H-mode cases in the bottom panel this is not the case: in the model, more fuelling does not lead to a larger source in the pedestal. In the next section it is argued that for the H-mode cases the implemented model for particle transport is insufficient; explaining the difference of the phases of D and χ_e, and the absence of a stronger source with additional fuelling. In conclusion, in all cases where the model can be trusted, D and χ_e at the pedestal foot modulate in phase.

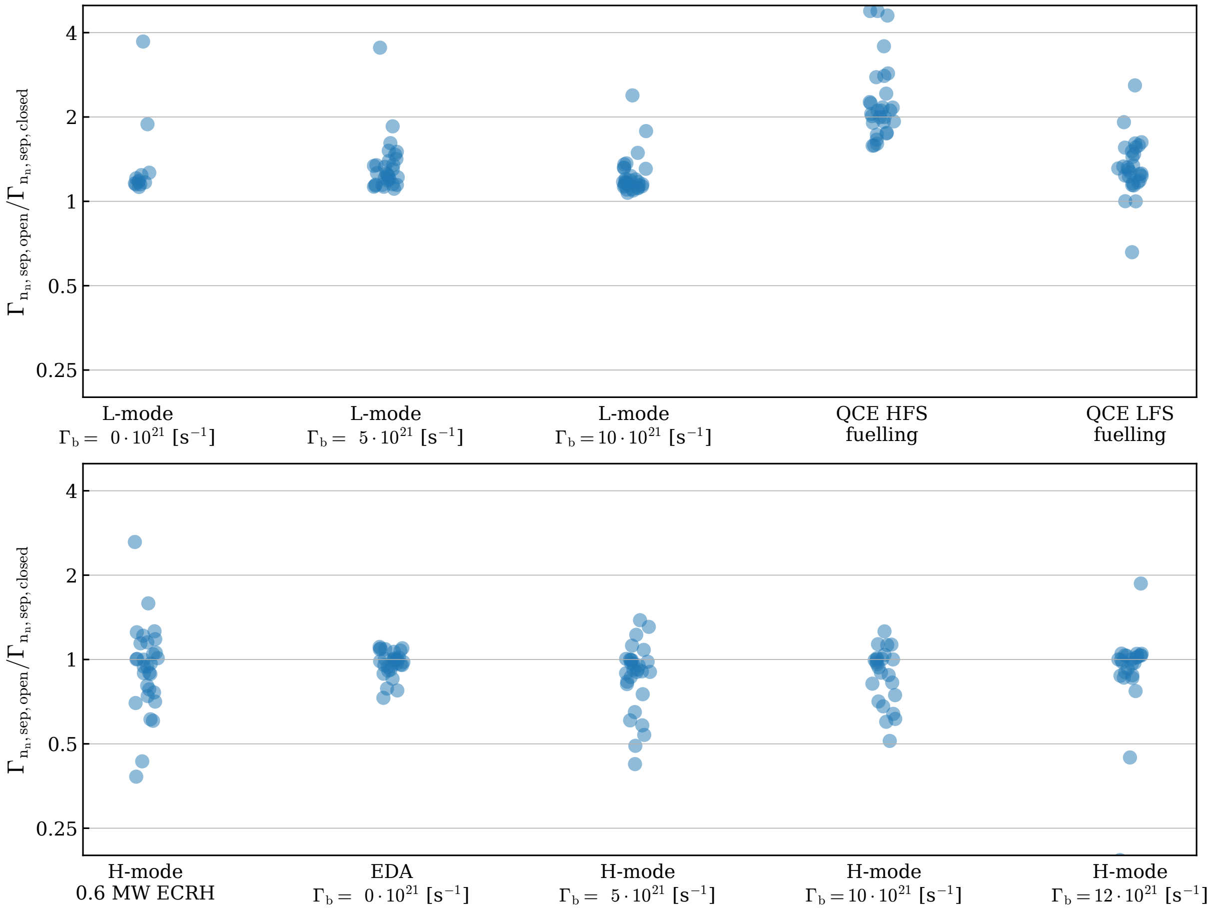

Figure 5.24.: The relative increase of flux of neutral atoms across the separatrix when opening the fuelling valve, as selected by the optimization routine for agreement between the ASTRA simulations and the experimental data. Each circle represents a successful fit.

5.3.3. Implications of Modulating Particle Transport Coefficients for Determining D and v

In the previous sections the change of transport coefficients on fast time scales in response to a change in fuelling was presented and quantified. This interesting phenomenon allows studying properties of turbulence in the edge, but also makes the disentanglement of D and v vastly more difficult. It will be shown how the altered transport conditions fit together with the measurements under the assumption $D \approx \chi_e$, resolving the issue of the unexpected behavior in the H-mode cases.

Mathematical Analysis

Before discussing two qualitative examples it will be shown from a mathematical point of view that a temporally evolving D can justify every density evolution. Starting with the density equation (2.1) we obtain

$$\partial_t n_\mathrm{e} = \partial_\rho \left(D\partial_\rho n_\mathrm{e} - v n_\mathrm{e}\right) + S_\mathrm{e} \tag{5.11}$$

$$\partial_t n_\mathrm{e} = \left(\partial_\rho D\right) \partial_\rho n_\mathrm{e} + D\, \partial_\rho^2\, n_\mathrm{e} - \partial_\rho \left(v n_\mathrm{e}\right) + S_\mathrm{e} \tag{5.12}$$

$$\partial_t n_\mathrm{e} - S_\mathrm{e} + \partial_\rho \left(v n_\mathrm{e}\right) - D\, \partial_\rho^2\, n_\mathrm{e} = \left(\partial_\rho D\right) \partial_\rho n_\mathrm{e} \tag{5.13}$$

$$\partial_\rho D = -D \frac{\partial_\rho^2\, n_\mathrm{e}}{\partial_\rho n_\mathrm{e}} + \partial_t n_\mathrm{e} - S_\mathrm{e} + \partial_\rho \left(v n_\mathrm{e}\right). \tag{5.14}$$

Equation (5.14) is interpreted as ordinary differential equation for $D(\rho, t)$ for given $n_\mathrm{e}(\rho, t)$, $v(\rho, t)$ and $S_\mathrm{e}(\rho, t)$. Physically, the dependence of D on t comes from an unknown dependency on the plasma parameters. For every combination of those parameters and for every time t it is possible to solve the differential equation. The method to determine D and v with the aid of modulation experiments, as it is usually used, assumes D and v to be independent of time; these D and v then have to solve equation 5.14 for all t. From the previous section it is known, however, that D is not identical for all points in time. This means a $D(\rho, t)$ can be determined for each t and each choice of v, and there is no information left to determine the physical value of v. From a technical point of view we have to take care of the integration constant, which can be used to set the particle flux at the magnetic axis to zero, and the division by the density gradient which can be 0. D will also become negative in some occasions, but in general these restrictions will not be enough to decide if a pinch is present.

Qualitative Explanation of the Edge Density Evolution

Figure 5.25 shows illustrations for two different cases, an H-mode (a) and a QCE discharge (b). The initial discussion will assume that the source S_e does not change. Later the modulated source will be introduced into the discussion. The initial density profile with the closed modulation valve is shown as blue solid line. When the valve is opened, the separatrix density rises (H-mode) or falls (QCE). The particle transport translates these changes to changes at the pedestal top: in H-mode the pedestal top density would rise, in QCE it would fall. On the one hand, if the pedestal stems from constant source and diffusion alone, the absolute changes of the pedestal top density and the separatrix density would be identical. On the other hand, if it stems from diffusion and pinch alone, the relative changes would be identical; because the pedestal top density is higher than the separatrix density the pedestal due to a pinch would react more strongly. Regardless of whether the particle source or a pinch is the main contributor to the density pedestal, the changes go in the wrong direction. The purple solid line shows the measured density response for the two cases. In H-mode, the edge interferometry mandates that the pedestal top density does not increase, while in the QCE discharge the pedestal top density it mandates a density increase.

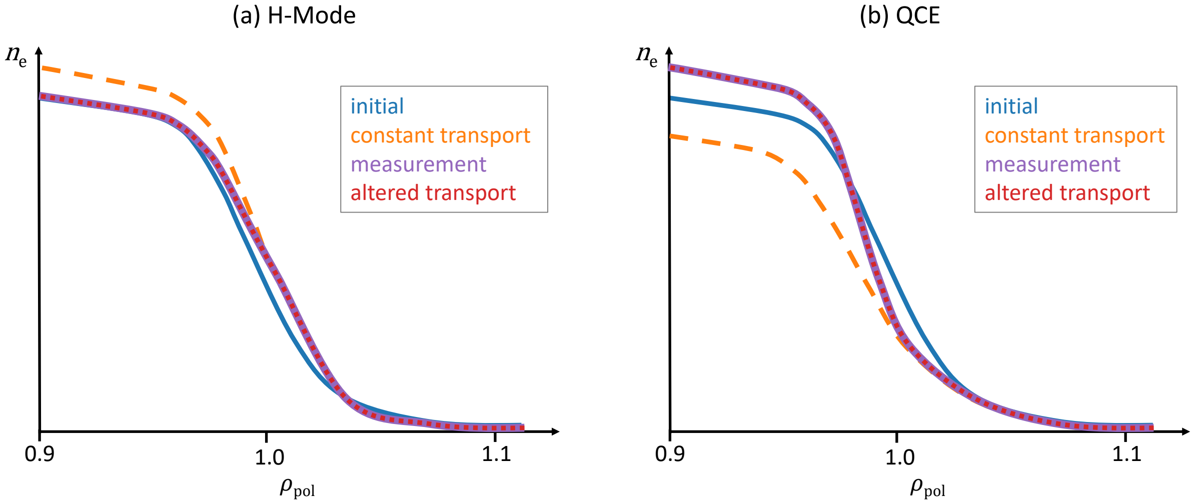

Figure 5.25.: Qualitative illustration of the profiles different transport mechanisms would cause when the separatrix density changes while the particle source S_e remains constant. The two examples we are investigating are an H-mode (a) and a QCE (b). We illustrate how a density pedestal purely due to a pinch and unaltered diffusion would react differently than the experiment, and that a changing diffusivity could lead to agreement. We show the initial profile with closed valve (blue solid line) and several profiles with the altered separatrix boundary as boundary condition: the profile a pinch would generate (orange dashed line) and the profile we measure for the opened valve (purple thick solid line), which is identical to the profile we can tailor with a pinch and an altered particle diffusivity (red dotted line).

The investigation in section 5.2.3 showed that χ_e and χ_i modulate in phase. And in section 5.3 it was found that χ_e and D modulate in phase in the trustworthy cases. Therefore, χ_e will now be interpreted as a proxy for D. Section 5.2.2 discussed that the electron heat transport changes significantly in the whole edge region. For the H-mode cases, transport increased abruptly in the whole edge region when the valve was opened. An increased diffusivity leads both for source-caused and pinch-caused density gradients to a flattening, dissipating the density increase from the separatrix density which acts as boundary condition. The envisioned density profile with increased D is shown as red dotted line in figure 5.25a.

In the QCE discharge transport behaves oppositely: χ_e at the pedestal top rises only 15 ms after the valve is opened, merely 7 ms before the valve closes again. Averaged over the open- and the closed-valve intervals the pedestal top χ_e is lower when the valve is open than when it is closed. D likely behaves analogously, the reduced particle diffusivity then leads to a steepening of the density profile, allowing the pedestal top density to recover and even surpass the value from before the valve opening. Again this last profile is illustrated as red dotted line in figure 5.25b.

The developed ASTRA model follows a different route: D is kept temporally constant inside of $\rho_{pol} = 0.99$. Therefore the optimization routine adjusts the particle source to compensate the difference between the orange dashed lines and the thick purple lines in figure 5.25. For the H-modes this means reducing the neutral particle flow across the separatrix when the valve is opened, and for the QCE this means increasing the particle flow when the valve is opened.

Equation 5.14 does not allow to differentiate between the explanation resting on modulating diffusivity and the explanation of modulating source, unless the detailed evolution of D would already be known. However, a reduced particle flux across the separatrix, when increasing fuelling, appears unlikely, and subsequently, the explanation relying on the increased diffusivity is more plausible. For the QCE likely both effects contribute.

5.3.4. Fuelling Efficiency

This section is addresses how much of the fuelling particle flux is being ionized inside of the separatrix.

To answer this question it is not sufficient to only consider the density response. The H-mode cases with 1.8 MW of ECRH for example show only a weak density increase, but in the previous section it was discussed how this is most likely due to a strong increase in particle transport and *not* a weak increase or even decrease of the particle source.

With the QCE cases one has the opportunity for a better comparison. The setup, and therefore the plasma conditions, of both discharges is identical except for the fuelling location. Within experimental uncertainties, heat and particle diffusivities are in phase (figure 5.23), but with LFS fuelling the amplitudes are considerably smaller. Also the temporal evolution of the pedestal top density is very similar in both cases, but with LFS fuelling the amplitude is $\approx 80\,\%$ smaller. The core plasma behaves similarly in the two cases, but with different amplitudes. To conclude, the applied perturbation, i.e. the particle source, is much stronger in the HFS fuelling case than in the LFS fuelling case. The QCE cases feature a density shoulder, i.e. a high plasma density in the whole LFS SOL. The dense SOL plasma appears to partially ionize the fuelled neutrals and transport the particles to the divertor, and thus shields the core plasma from the fuelled neutrals.

6. Discussion

From steady state density profiles only D/v can be estimated, even if the particle source S_e is known. Because the temporal evolution of the density profile contains additional information, it is necessary to investigate transient events to estimate D and v separately [Sal15, Wil13, Tal19]. Also in this work transient events, caused by modulating the fuelling flow, are studied. It is, however, found that transport in the pedestal region and in the outer core, i.e. outside of $\rho_\mathrm{pol} = 0.8$, reacts very sensitively to altered conditions in all investigated L-mode, EDA H-mode, H-mode and QCE discharges. Particle, electron heat and ion heat transport increase with increased fuelling, but not necessarily with identical amplitude. Because of this strong link between all transport channels, the electron heat diffusivity χ_e is used as proxy for the particle diffusivity. χ_e can be determined more easily and reliably than D due to the more reliable data at the pedestal top, negligible power source at the edge and purely diffusive transport. The results propose to always analyse the heat diffusivity when working on particle transport: it shows comparably simply and robustly whether transport is changing.

One important question is how fuelling changes transport. Neutrals can directly interact with turbulence, an effect which is discussed and studied for the scrape-off layer [Thr18, Cor21]. In the confined region a more indirect cause for the changes in transport is suspected: an increased particle source, due to the fuelling, increases the local plasma density and cools the plasma because ionization and heating of the neutrals requires energy. As a point of reference, the fuelled particle flux of $8 \times 10^{21}\,\mathrm{s}^{-1}$ requires 200 kW, a substantial fraction of the available heating power, to be heated to 50 eV. These initial changes to the kinetic profiles influence turbulence. A relevant parameter for this is collisionality $\nu^* \propto n_\mathrm{e}/T_\mathrm{e}^2$, which correlates with the found χ_e close to the separatrix, as predicted by theory (section 4.3). The altered transport then also alters the kinetic profiles, dominating the further evolution in the steep gradient region and in H-mode also in the outer core.

Section 2.4 discusses a model for the edge density where incoming neutral particles are ionized by electron impact; the influx of neutral particles is balanced by a diffusive outflux of plasma. Such a model without pinch matches the experiments presented in this work well. It is paramount to not assume D to be identical for different fuelling levels or even discharges, as transport is sensitive to altered conditions. Increased fuelling leads to a larger particle source. When transport at the pedestal top reacts only little to the altered conditions, as in the investigated L-modes, this increased source leads to a moderate increase in pedestal top density. When transport increases strongly and immediately when fuelling is increased, as for the investigated ELMy H-modes and the EDA H-mode, the additional particles are flushed out from the confined region and only a small increase in density is visible. When transport is reduced by fuelling or reacts strongly delayed, as for the investigated QCE discharges, the density increase due to the increased particle source is amplified by reduced transport. In all investigated cases the behavior of the electron density, and the postulated particle transport changes, are in agreement with the behavior of χ_e. Due to the under-determinedness of the particle transport coefficients it is also possible to construct interpretations with a particle pinch instead of a source. Using χ_e as proxy for D, such an explanation would require that this pinch would have to modulate stronger than, identical to or weaker than / opposite to D, depending on case and position. The presented analysis cannot refute interpretations with a strong pinch such as Stacey et al. [Sta12]. But models which include the source as important contributor for the edge density gradient, such as those from [Mah02], require only the 'natural' change of the particle source due to fuelling, and therefore appear more plausible. To be able to determine D and v from a modulation experiment, it is necessary to not only have the time dependent flux surface averaged particle source, but also quantitative knowledge of the changes of D and v. The reconstructed particle diffusivity ranges between $0.02\,\mathrm{m^2\,s^{-1}}$ and $2\,\mathrm{m^2\,s^{-1}}$, depending on both the convection speed and the particle source. A constant transport coefficient across the steep gradient region could not match the dynamics. Instead, a stronger transport modulation at the pedestal foot is necessary to match the data. Increased particle diffusivity, and therefore limited density changes when adding fuelling, is reminiscent of investigations by Hughes et al. [Hug07]. Dunne et al. [Dun16] found a degradation of the pedestal top pressure with increased fuelling and density. This degradation is however due to reduced MHD stability, coinciding with earlier ELM crashes, and not due to turbulent transport which was studied here. Altered transport due to modulating fuelling was recently also found by Macwan et al. [Mac21], although without a comparable quantitative analysis, with a different focus and on a smaller machine.

Figure 6.1 from Bonanomi et al. shows the growth rate of edge instabilities for L-mode plasmas in the tokamaks ASDEX Upgrade and JET, with deuterium and hydrogen plasmas. The collisionalities of L-modes in this thesis are above one. In this range, the calculated growth rate increases with collisionality, agreeing both with the presented experiments and other theoretical investigations [Bou12, Rog98]. The modes are drift-wave-like. If the passing electrons are assumed to be adiabatic, i.e. instantly equilibrate potential perturbations along the field lines, the growth rate instead declines when collisionality increases, in excellent agreement with the drift-Alfvén picture of turbulence [Rog98, Sco05, Eic20].

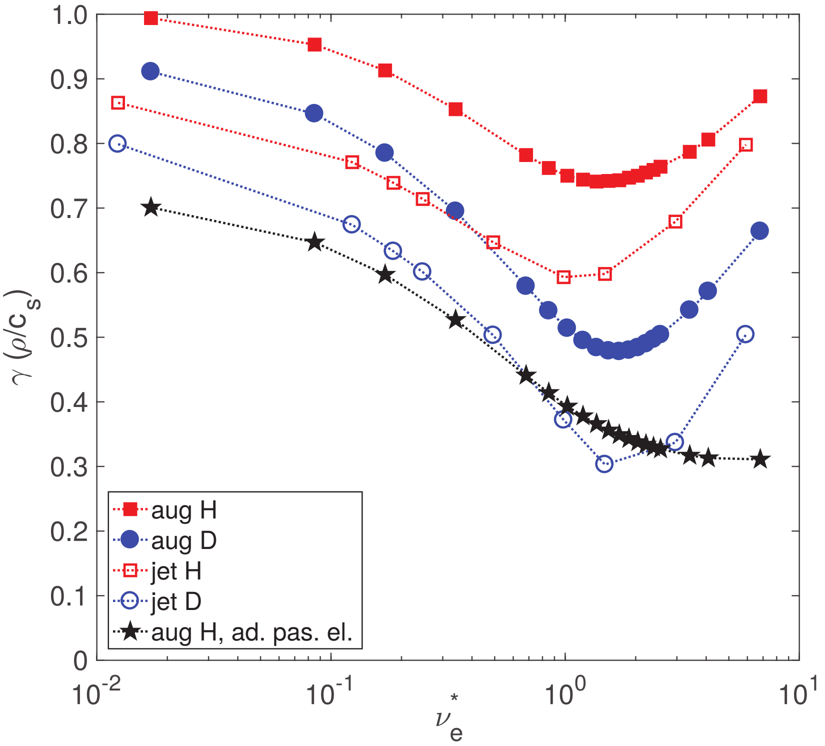

Figure 6.1.: The dominant growth rate in L-mode edge plasmas as function of collisionality. Hydrogen (Protium) and Deuterium plasmas from AUG and JET. Black stars show simulations where the electrons are assumed to be adiabatic. Figure is from Bonanomi et al. [Bon19].

6.1. Gyrokinetic Analysis with GENE

Tobias Görler performed a numerical analysis with the gyrokinetic turbulence code GENE [Jen00b, Goe11] for three of the presented cases: the L-mode with low fuelling, the EDA H-mode and the HFS fuelled QCE discharge. For all cases the radial positions $\rho_{\text{pol}} = 0.90$ and $\rho_{\text{pol}} = 0.98$ were selected. Due to the enormous costs of nonlinear edge simulations, the analysis is restricted to linear instability investigations in a flux-tube simulation domain to obtain first insights in a reasonable time span. The input profiles, i.e. density and temperatures, come from the ASTRA modelling.

In all cases one finds dominant ion temperature gradient modes (ITG) on large scales and electron temperature gradient modes (ETG) on small scales at $\rho_{\text{pol}} = 0.90$. In the steep gradient region, at $\rho_{\text{pol}} = 0.98$, the discharges differ: in L-mode large-scale trapped-electron modes (TEM) likely dominate transport. In the EDA H-mode and the QCE discharge, kinetic ballooning modes (KBM), also on large scales, are found to be dominant. This could be a remnant of the flux-tube approach and KBM could become subdominant in global simulations [Hat19]. Especially for the EDA case, the transition from KBM to TEM is within the experimental error bars. The

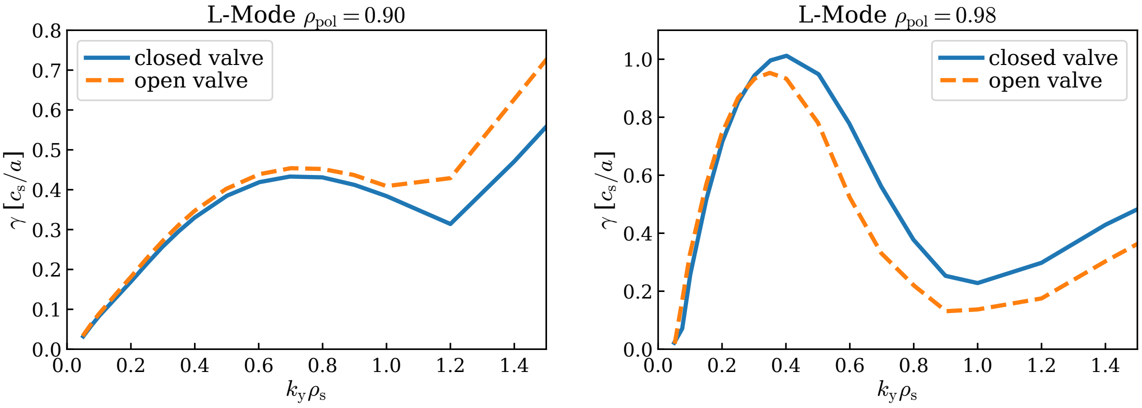

Figure 6.2.: The linear growth rates γ from GENE at $\rho_{\mathrm{pol}} = 0.90$ and $\rho_{\mathrm{pol}} = 0.98$ for the L-mode case #37758 for opened and closed valve, as a function of the normalized inverse structure size $k_{\mathrm{y}}\rho_{\mathrm{s}}$. Only the dominant large scales are shown.

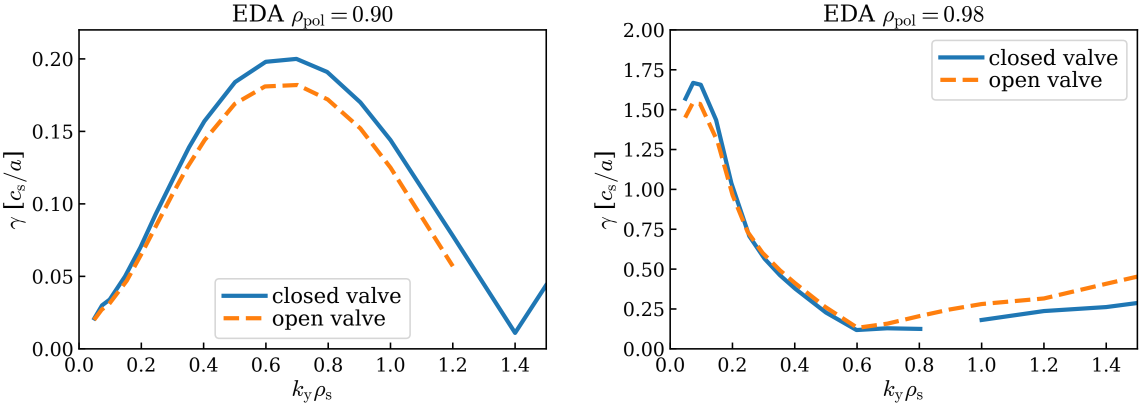

Figure 6.3.: The linear growth rate γ from GENE at $\rho_{\mathrm{pol}} = 0.90$ and $\rho_{\mathrm{pol}} = 0.98$ for the EDA case #37773 for opened and closed valve, as a function of the normalized inverse structure size $k_{\mathrm{y}}\rho_{\mathrm{s}}$. Only the dominant large scales are shown.

found ballooning modes for QCE agree well with the general understanding of this scenario [Har22, Rad22].

The GENE simulations were performed at different time points during the modulation period. For the QCE discharge at $\rho_{\mathrm{pol}} = 0.90$, the times 0 ms, 10 ms, 20 ms and 30 ms with respect to the valve opening to resolve the temporal behavior seen in the experimental analysis. All other cases are analyzed at 0 ms and 20 ms, i.e. when the valve has been closed and opened for as long as the modulation allows. Figures 6.2, 6.3 and 6.4 show the obtained dominant growth rates, at large scales, as function of turbulent structure size for the three modelled discharges. The small scales at $\rho_{\mathrm{pol}} = 0.90$ show the same trends as the large scales, and are not shown. At $\rho_{\mathrm{pol}} = 0.98$ the large scales dominate strongly, and are also not shown.

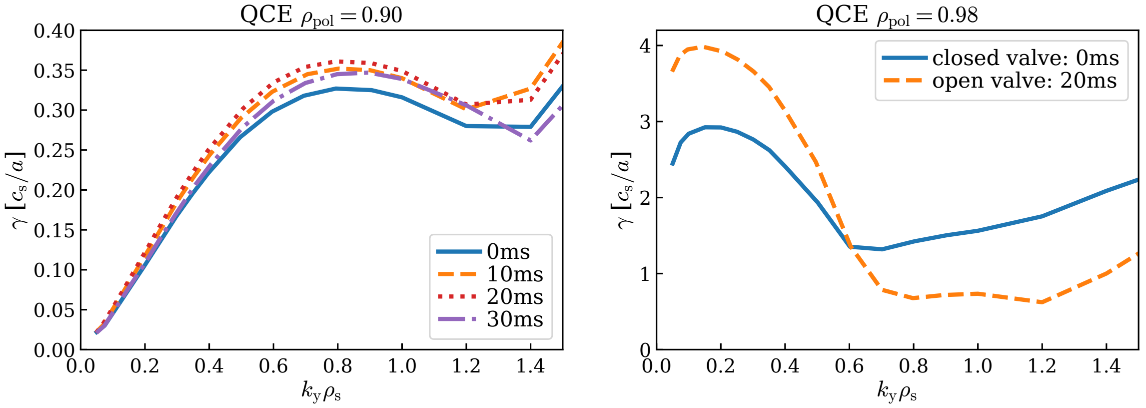

Figure 6.4.: The linear growth rate γ from GENE at $\rho_{\mathrm{pol}} = 0.90$ and $\rho_{\mathrm{pol}} = 0.98$ for the QCE case #37774, as a function of the normalized inverse structure size $k_y\rho_s$. For $\rho_{\mathrm{pol}} = 0.90$ four points in time are evaluated, for $\rho_{\mathrm{pol}} = 0.98$ the same points in time as in figures 6.2 and 6.3 are shown. Only the dominant large scales are shown.

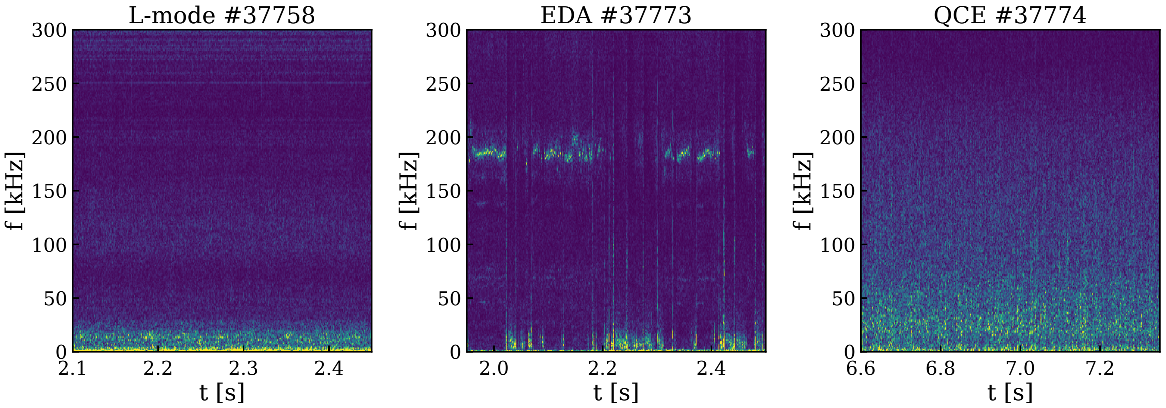

Figure 6.5.: Spectrograms of the magnetic pick-up coil `MHI B31-14` for the three cases which are analyzed with GENE.

In L-mode (figure 6.2) at $\rho_{\mathrm{pol}} = 0.90$, the growth rates are larger when the valve is open for all structure sizes. At $\rho_{\mathrm{pol}} = 0.98$ the behavior is not as uniform. Large structures, i.e. values of $k_y\rho_s$ smaller than 0.3, grow slightly faster when the valve is open, while smaller structures grow faster when the valve is closed. The expected transport from turbulent structures is approximated by combining the growth rate with the structure size as $\gamma/\left(k_y\rho_s\right)^2$ [Dan05]. Weighing the growth rates accordingly reveals that structures with $k_y\rho_s < 0.3$ contribute more to transport than smaller structures. Therefore, also in the pedestal, transport is increased with increased fuelling. The experimental results for χ_e show the same dependency.

Figure 6.3, depicting results for the EDA H-mode, yields the reverse behavior: the dominant modes, at small $k_y\rho_s$, grow more weakly when the valve is open. In the experiment, transport in the whole edge region increased promptly when the valve was opened. A possible explanation can be found when considering the spectrograms shown in figure 6.5. The EDA H-mode is the only case where a high-frequency mode between 180 kHz and 190 kHz is visible in the magnetics. Whenever the high-frequency mode is present, the low-frequency components below 30 kHz, originating from turbulence, are absent. This suggests that the high-frequency mode causes sufficient transport to suppress these other instabilities. The linear flux-tube simulations with GENE presented here do not capture the transport of this mode.

The QCE pedestal is once again dominated by large structures, which exhibit an increased growth rate for the fuelled case. This increase by $\approx 30\,\%$ is far larger than what was seen for the other cases. Also the experiment finds an increase in transport when opening the valve. The found KBM is the proposed instability for the QCE pedestal foot [Har22, Rad22]. At $\rho_{\mathrm{pol}} = 0.90$, the agreement between GENE and the ASTRA analysis is imperfect. According to GENE, transport is indeed comparably small at $t = 0\,\mathrm{ms}$, but, already at $t = 10\,\mathrm{ms}$, GENE finds transport comparable to the later points in time.

All in all, the linear flux-tube instability analysis with GENE reproduces and identifies some of the underlying trends. A more complete picture would, however, require nonlinear and possibly radially global simulations considering the various experimental input parameter uncertainties. This tremendous task is left for future work.

6.2. Edge Density Profile in Future Reactors

The final section before the discussion chapter returns to the question of the introduction: what will the density profile of future reactors be?

The two effects which can lead to a steep density gradient are a pinch and a finite particle flux across the separatrix. A pinch is not apparent in present experiments, but cannot be excluded. Additionally, it is not clear how edge particle transport will differ between present machines and future devices.

Also the particle flux across the separatrix is not known, but a lower bound can be estimated [Rom15]: a reactor utilizing D-T fuel will produce 3.6×10^{20} helium ions per second for each gigawatt of fusion power; in steady state the helium flux across the separatrix therefore has to be $3.6 \times 10^{20}\,\mathrm{s}^{-1}$ for a 1 GW reactor. A high concentration of helium would dilute the fuel. Assuming equal transport for helium and hydrogen isotopes, the D-T flux across the separatrix has to be more than 20 times the flux of helium to maintain a helium concentration below 5 % [Rom15]. For ITER, with 500 MW of fusion power, this results in a flux across the separatrix of

$3.6 \times 10^{21}\,\mathrm{s}^{-1}$. The density gradient at the edge for purely diffusive transport follows from

$$\Gamma = AD\nabla n_\mathrm{e} \tag{6.1}$$

$$\nabla n_\mathrm{e} = \frac{\Gamma}{AD}, \tag{6.2}$$

with A being the area of the flux surface. D in the ITER pedestal is unknown, therefore one cannot predict the associated density gradient. With $D = 0.2\,\mathrm{m}^2\,\mathrm{s}^{-1}$ we obtain $1 \times 10^{20}\,\mathrm{m}^{-4}$, approximately 5 % of the density gradient at $\rho_\mathrm{pol} = 0.985$ in the AUG QCE discharge #37774 at 6.8 s.

In large devices, such as ITER and DEMO, the SOL is expected to shield neutrals efficiently, similar to what was discussed in the previous section. The neutral flux across the separatrix originating from recycling and gas fuelling is therefore expected to be small, smaller than the $3.6 \times 10^{21}\,\mathrm{s}^{-1}$ deemed necessary to keep the helium concentration low [Rom15]. Pellet fuelling can increase the particle source in the confined region. For the EU-DEMO power plant pellet fluxes of $\approx 7 \times 10^{21}\,\mathrm{s}^{-1}$ are expected [Lan20].

In conclusion, ITER and Demo will feature a density gradient at the edge, except if particles are convected outward. But it likely will be smaller than in present devices because the large gas fuelling and recycling particle source in the pedestal region is strongly reduced. The particle flux across the separatrix, and with it the density gradient in the pedestal, however, has to be kept high enough to facilitate helium exhaust, requiring sufficient pellet fuelling.

7. Summary and Outlook

Understanding transport in the edge of tokamak plasmas is crucial for predicting future devices and for planning reactors. In this work, to study transport coefficients at the plasma edge, gas puff modulation experiments were performed in several L-mode, enhanced D-α (EDA) H-mode, H-mode and quasi-continuous exhaust (QCE) discharges. Accurate edge data were obtained, both for the plasma density and the electron temperature, and in one case also for ion temperatures. For the extensive analysis, all discharges were modelled using the ASTRA transport code, incorporating a new and improved neutral model. Fits of the unknown, randomly initialized parameters yielded both accurate diffusivities for heat transport and a set of solutions for the particle transport.

When the fuelling valve is opened, the plasma in the outermost region at and outside of the separatrix cools as neutrals are ionized, and the plasma is diluted by the new plasma particles. Simultaneously, the plasma density inside of the separatrix generally rises due to the increased particle source. The analysis shows that transport in heat and particle channels changes due to these altered conditions, and that the individual channels behave similarly or even identically. The altered transport conditions lead to a cold pulse which propagates into the core plasma, and make a determination of particle diffusivity and convection impossible. Heat diffusivity on the other hand, due to the well-known source term and its purely diffusive nature, was determined accurately, and allows to determine the characteristics of the underlying dominant transport mechanisms. It was not only shown that the pedestal top, or outer core, behaves differently than the steep gradient region, but also that the pedestal foot close to the separatrix has to be treated independently. The evolution of the density profile can always be understood as the result of an increased particle source due to fuelling and a particle diffusivity which evolves similarly to the heat diffusivity; convective particle transport is never necessary.

In all discharges, transport across the separatrix increases with increased fuelling, but the behavior further inside differs. The analyzed discharges fall into three categories. First, in L-mode, transport close to the separatrix is proportional to collisionality which is increased by additional fuelling. Inside of the steep gradient region, transport reacts only weakly to the altered conditions. Second, two QCE discharges, one fuelled from the high field side and one from the low field side, behave similarly to each other, with less neutrals penetrating the low field side scrape-off layer where the density is high. Transport at the pedestal foot increases with fuelling, in agreement with transport dominated by kinetic ballooning modes as they were found in gyrokinetic simulations and as suggested by Harrer et al. and Radovanovic et al. [Har22, Rad22]. Transport at the pedestal top is reduced, or increased with a large delay, by the additional fuelling. Third, in the EDA H-mode and other H-modes, transport increases in the whole edge region, until $\rho_{\mathrm{pol}} \approx 0.85$, only a few milliseconds after fuelling is increased.

The edge density profile in next generation devices, such as ITER or DEMO, will show a density gradient, even if particle transport is purely diffusive: sufficient helium exhaust requires a particle flux on the order of $1 \times 10^{22}\,\mathrm{s}^{-1}$ per gigawatt of fusion power. Diffusive transport requires a density gradient to cause this flux of particles.

Outlook

Determining the particle diffusivity and convection speed using modulation experiments appears very difficult: In this work it was discovered that the transport coefficients are sensitive enough to be altered even by the modulation itself, introducing sufficient additional unknowns to make the transport equations under-determined.

One way forward is to expand the comparison of experimental observations to simulations. In section 6.1 it was found that linear GENE simulations are able to reproduce some, but not all trends observed in the experiment. It would be of interest whether nonlinear simulations agree better with the experiment. These nonlinear simulations could also improve the understanding of the experiment. A different approach would be to perform less computationally expensive investigations with quasilinear turbulence models such as TGLF [Sta07]. These models were recently shown to be able to reproduce many aspects of L-mode edge plasmas [Ang22]. The reproduction of the measured cold pulse would be a further test of the model, and would aid in the interpretation of the experiment.

The temperature pedestal is often more narrow than the density pedestal [Beu11]. A possible explanation is that transport is reduced in the full pedestal width, i.e. the width of the temperature pedestal, but the density pedestal is narrower because the particle source is narrower than the transport barrier. If one where to replace the recycling and gas fuelling particle source with a particle source in the core, i.e. with pellet fuelling, the small particle diffusivity in the edge transport barrier has to transport the fuelled particle flux through the whole transport barrier. One would then expect that the density pedestal grows in width to match the temperature pedestal because the steep density gradient is necessary everywhere, and not just in the outer region, to produce sufficient particle flux for the steady state. Experimentally, this could be investigated with strong pellet fuelling and reduced recycling, e.g. with a fresh boronization. Such an investigation of the edge density profile with dominant pellet fuelling would also connect to the edge density profile in next generation devices.

Bibliography

[Ang22] C. Angioni, T. Gamot, G. Tardini, et al. Confinement properties of L-mode plasmas in ASDEX Upgrade and full-radius predictions of the TGLF transport model. *Nuclear Fusion*, 62(6):066015, 2022.

[Bar87] R. Bartiromo, G. Bracco, M. Brusati, et al. Design and calibration of the JET neutral particle analyzer. *Review of scientific instruments*, 58(5):788–795, 1987.

[Beu11] M. Beurskens, T. Osborne, P. Schneider, et al. H-mode pedestal scaling in DIII-D, ASDEX Upgrade, and JET. *Physics of Plasmas*, 18(5):056120, 2011.

[Big90] H. Biglari, P. Diamond, and P. Terry. Influence of sheared poloidal rotation on edge turbulence. *Physics of Fluids B: Plasma Physics*, 2(1):1–4, 1990.

[Boe03] J. A. Boedo, D. L. Rudakov, R. A. Moyer, et al. Transport by intermittency in the boundary of the DIII-D tokamak. *Physics of Plasmas*, 10(5):1670–1677, 2003.

[Bog21] K. Bogar, B. Geiger, P. Schneider, et al. Direct determination of midplane background neutral density profiles from neutral particle analyzers. *Nuclear Fusion*, 61(3):036001, 2021.

[Bon19] N. Bonanomi, C. Angioni, P. Crandall, et al. Effect of the isotope mass on the turbulent transport at the edge of L-mode plasmas in ASDEX Upgrade and JET-ILW. *Nuclear Fusion*, 59(12):126025, 2019.

[Bou12] C. Bourdelle, X. Garbet, R. Singh, et al. New glance at resistive ballooning modes at the edge of tokamak plasmas. *Plasma Physics and Controlled Fusion*, 54(11):115003, 2012.

[Car17] D. Carralero, J. Madsen, S. Artene, et al. A study on the density shoulder formation in the SOL of H-mode plasmas. *Nuclear Materials and Energy*, 12:1189–1193, 2017.

[Cav16] M. Cavedon, T. Pütterich, E. Viezzer, et al. Interplay between turbulence, neoclassical and zonal flows during the transition from low to high confinement mode at ASDEX Upgrade. *Nuclear Fusion*, 57(1):014002, 2016.

[Cav17] M. Cavedon, T. Pütterich, E. Viezzer, et al. Pedestal and Er profile evolution during an edge localized mode cycle at ASDEX Upgrade. *Plasma Physics and Controlled Fusion*, 59(10):105007, 2017.

[Cit17] J. Citrin, C. Bourdelle, F. J. Casson, et al. Tractable flux-driven temperature, density, and rotation profile evolution with the quasilinear gyrokinetic transport model QuaLiKiz. *Plasma Physics and Controlled Fusion*, 59(12):124005, 2017.

[Cor21] A. Coroado and P. Ricci. Moving toward mass-conserving simulations of plasma turbulence and kinetic neutrals in the tokamak boundary with the GBS code. *Physics of Plasmas*, 28(2):022310, 2021.

[Dan05] T. Dannert and F. Jenko. Gyrokinetic simulation of collisionless trapped-electron mode turbulence. *Physics of Plasmas*, 12(7):072309, 2005.

[Dav21] P. David, M. Bernert, T. Pütterich, et al. Optimization of the computation of total and local radiated power at ASDEX Upgrade. *Nuclear Fusion*, 61(6):066025, 2021.

[D'i11] D. D'ippolito, J. Myra, and S. Zweben. Convective transport by intermittent blob-filaments: Comparison of theory and experiment. *Physics of Plasmas*, 18(6):060501, 2011.

[Dun16] M. G. Dunne, S. Potzel, F. Reimold, et al. The role of the density profile in the ASDEX-Upgrade pedestal structure. *Plasma Physics and Controlled Fusion*, 59(1):014017, 2016.

[Eic13] T. Eich, A. Leonard, R. Pitts, et al. Scaling of the tokamak near the scrape-off layer H-mode power width and implications for ITER. *Nuclear fusion*, 53(9):093031, 2013.

[Eic20] T. Eich, P. Manz, R. Goldston, et al. Turbulence driven widening of the near-SOL power width in ASDEX Upgrade H-Mode discharges. *Nuclear Fusion*, 60(5):056016, 2020.

[Eic21] T. Eich, P. Manz, et al. The separatrix operational space of ASDEX Upgrade due to interchange-drift-Alfvén turbulence. *Nuclear Fusion*, 61(8):086017, 2021.

[Eva05] T. Evans, R. Moyer, J. Watkins, et al. Suppression of large edge localized modes in high confinement DIII-D plasmas with a stochastic magnetic boundary. *Journal of nuclear materials*, 337:691–696, 2005.

[Fis08] R. Fischer, E. Wolfrum, J. Schweinzer, et al. Probabilistic lithium beam data analysis. *Plasma Physics and Controlled Fusion*, 50(8):085009, 2008.

[Fis10] R. Fischer, C. Fuchs, B. Kurzan, et al. Integrated data analysis of profile diagnostics at ASDEX Upgrade. *Fusion science and technology*, 58(2):675–684, 2010.

[Fre08] J. P. Freidberg. *Plasma physics and fusion energy.* Cambridge university press, 2008.

[Gen92] K. Gentle, O. Gehre, and K. Krieger. Determination of particle transport coefficients in ASDEX by gas modulation. *Nuclear fusion*, 32(2):217, 1992.

[Gil20] L. Gil, C. Silva, T. Happel, et al. Stationary ELM-free H-mode in ASDEX Upgrade. *Nuclear Fusion*, 60(5):054003, 2020.

[Goe11] T. Goerler, X. Lapillonne, S. Brunner, et al. The global version of the gyrokinetic turbulence code GENE. *Journal of Computational Physics*, 230(18):7053–7071, 2011.

[Gre99] M. Greenwald, R. Boivin, P. Bonoli, et al. Characterization of enhanced Dα high-confinement modes in Alcator C-Mod. *Physics of Plasmas*, 6(5):1943–1949, 1999.

[Gri17a] M. Griener, J. M. Burgos, M. Cavedon, et al. Qualification and implementation of line ratio spectroscopy on helium as plasma edge diagnostic at ASDEX Upgrade. *Plasma Physics and Controlled Fusion*, 60(2):025008, 2017.

[Gri17b] M. Griener, O. Schmitz, K. Bald, et al. Fast piezoelectric valve offering controlled gas injection in magnetically confined fusion plasmas for diagnostic and fuelling purposes. *Review of scientific instruments*, 88(3):033509, 2017.

[Gri18] M. Griener, E. Wolfrum, M. Cavedon, et al. Helium line ratio spectroscopy for high spatiotemporal resolution plasma edge profile measurements at ASDEX Upgrade. *Review of Scientific Instruments*, 89(10):10D102, 2018.

[Gro02] R. Groebner, M. Mahdavi, A. Leonard, et al. The role of neutrals in high-mode (H-mode) pedestal formation. *Physics of Plasmas*, 9(5):2134–2140, 2002.

[Gut20] W. F. Guthrie. *NIST/SEMATECH e-Handbook of Statistical Methods (NIST Handbook 151).* National Institute of Standards and Technology, 2020.

[Haa98] G. Haas and H. Bosch. In vessel pressure measurement in nuclear fusion experiments with asdex gauges. *Vacuum*, 51(1):39–46, 1998.

[Hai93] E. Hairer, S. Nørsett, and G. Wanner. *Solving ordinary differential equations, I: Nonstiff problems.* Springer, 1993.

[Har22] G. Harrer, M. Faitsch, L. Radovanovic, et al. Quasicontinuous exhaust scenario for a fusion reactor: The renaissance of small edge localized modes. *Physical Review Letters*, 129(16):165001, 2022.

[Hat19] D. Hatch, M. Kotschenreuther, S. Mahajan, et al. Direct gyrokinetic comparison of pedestal transport in JET with carbon and ITER-like walls. *Nuclear Fusion*, 59(8):086056, 2019.

[Hou97] W. Houlberg, K.-C. Shaing, S. Hirshman, et al. Bootstrap current and neoclassical transport in tokamaks of arbitrary collisionality and aspect ratio. *Physics of Plasmas*, 4(9):3230–3242, 1997.

[Hug07] J. Hughes, B. LaBombard, J. Terry, et al. Edge profile stiffness and insensitivity of the density pedestal to neutral fuelling in Alcator C-Mod edge transport barriers. *Nuclear Fusion*, 47(8):1057, 2007.

[IEO21] International Energy Outlook 2021. Technical report, U.S. Energy Information Administration, 1000 Independence Ave SW, Washington, DC, 2021.

[Jen00a] F. Jenko. Particle pinch in collisionless drift-wave turbulence. *Physics of Plasmas*, 7(2):514–518, 2000.

[Jen00b] F. Jenko, W. Dorland, M. Kotschenreuther, et al. Electron temperature gradient driven turbulence. *Physics of plasmas*, 7(5):1904–1910, 2000.

[Jof19] E. Joffrin, S. Abduallev, M. Abhangi, et al. Overview of the JET preparation for deuterium–tritium operation with the ITER like-wall. *Nuclear Fusion*, 59(11):112021, 2019.

[Kal13] A. Kallenbach, M. Bernert, R. Dux, et al. Impurity seeding for tokamak power exhaust: from present devices via ITER to DEMO. *Plasma Physics and Controlled Fusion*, 55(12):124041, 2013.

[Kir04] A. Kirk, G. Counsell, E. Arends, et al. H-mode pedestal characteristics on MAST. *Plasma physics and controlled fusion*, 46(5A):A187, 2004.

[Kop00] J. Koponen, T. Geist, U. Stroth, et al. Perturbative particle transport studies in the W7-AS stellarator. *Nuclear fusion*, 40(3):365, 2000.

[Kot19] M. Kotschenreuther, X. Liu, D. Hatch, et al. Gyrokinetic analysis and simulation of pedestals to identify the culprits for energy losses using ‘fingerprints’. *Nuclear Fusion*, 59(9):096001, 2019.

[Kra91] K. S. Krane. *Introductory nuclear physics*. John Wiley & Sons, 1991.

[Lag17] F. Laggner, S. Keerl, J. Gnilsen, et al. Divertor, scrape-off layer and pedestal particle dynamics in the ELM cycle on ASDEX Upgrade. *Plasma Physics and Controlled Fusion*, 60(2):025002, 2017.

[Lan20] P. T. Lang, F. Cismondi, C. Day, et al. Optimizing the EU-DEMO pellet fuelling scheme. *Fusion Engineering and Design*, 156:111591, 2020.

[Loa14] A. Loarte, G. Huijsmans, S. Futatani, et al. Progress on the application of ELM control schemes to ITER scenarios from the non-active phase to DT operation. *Nuclear Fusion*, 54(3):033007, 2014.

[Loa15] A. Loarte, F. Liu, G. Huijsmans, et al. MHD stability of the ITER pedestal and SOL plasma and its influence on the heat flux width. *Journal of Nuclear Materials*, 463:401–405, 2015.

[Lud20] T. Luda, C. Angioni, M. Dunne, et al. Integrated modeling of ASDEX upgrade plasmas combining core, pedestal and scrape-off layer physics. *Nuclear Fusion*, 60(3):036023, 2020.

[Mac21] T. Macwan, H. Raj, K. Singh, et al. Gas-puff induced cold pulse propagation in ADITYA-U tokamak. *Nuclear Fusion*, 61(9):096029, 2021.

[Mah02] M. Mahdavi, T. Osborne, A. Leonard, et al. High performance H mode plasmas at densities above the Greenwald limit. *Nuclear fusion*, 42(1):52, 2002.

[Man20] P. Manz, C. Hufnagel, A. Zito, et al. The diffusion limit of ballistic transport in the scrape-off layer. *Physics of Plasmas*, 27(2):022506, 2020.

[Mar11] Y. Marandet, A. Mekkaoui, D. Reiter, et al. Transport of neutral particles in turbulent scrape-off layer plasmas. *Nuclear fusion*, 51(8):083035, 2011.

[McC97] K. McCormick, S. Fiedler, G. Kocsis, et al. Edge density measurements with a fast Li beam probe in tokamak and stellarator experiments. *Fusion Engineering and Design*, 34:125–134, 1997.

[McD18] R. McDermott, R. Dux, T. Pütterich, et al. Evaluation of impurity densities from charge exchange recombination spectroscopy measurements at ASDEX Upgrade. *Plasma Physics and Controlled Fusion*, 60(9):095007, 2018.

[MD21] V. Masson-Delmotte, P. Zhai, A. Pirani, et al., editors. *Climate Change 2021: The Physical Science Basis. Contribution of Working Group I to the Sixth Assessment Report of the Intergovernmental Panel on Climate Change.* Cambridge University Press, 2021.

[Mly10] A. Mlynek, G. Schramm, H. Eixenberger, et al. Design of a digital multiradian phase detector and its application in fusion plasma interferometry. *Review of scientific instruments*, 81(3):033507, 2010.

[Moo76] D. S. Moore. Chi-Square Tests. Technical report, Purdue University Department of Statistics, West Lafayette, Indiana, 1976.

[Mor20] S. Mordijck. Overview of density pedestal structure: role of fueling versus transport. *Nuclear Fusion*, 60(8):082006, 2020.

[Nag93] K. Nagashima, A. Sakasai, and T. Fukuda. Gas puff modulation experiments on JT-60U. *Nuclear fusion*, 33(11):1677, 1993.

[Nau07] V. Naulin. Turbulent transport and the plasma edge. *Journal of Nuclear Materials*, 363-365:24–31, 2007.

[Nic21] T. Nicholas, T. Davis, F. Federici, et al. Re-examining the role of nuclear fusion in a renewables-based energy mix. *Energy Policy*, 149:112043, 2021.

[Nol10] B. Nold, G. D. Conway, T. Happel, et al. Generation of blobs and holes in the edge of the ASDEX Upgrade tokamak. *Plasma Physics and Controlled Fusion*, 52(6):065005, 2010.

[Oya06] N. Oyama, P. Gohil, L. Horton, et al. Pedestal conditions for small ELM regimes in tokamaks. *Plasma physics and controlled fusion*, 48(5A):A171, 2006.

[Par15] *Paris Agreement.* United Nations Treaty Collection, Chapter XXVII 7. d, 2015. URL `https://unfccc.int/sites/default/files/resource/parisagreement_publication.pdf`. Adopted 2015-12-12.

[Per02] G. V. Pereverzev and P. Yushmanov. ASTRA. Automated System for TRansport Analysis in a tokamak. 2002.

[Rad22] L. Radovanovic, M. Dunne, E. Wolfrum, et al. Developing a physics understanding of the quasi-continuous exhaust regime: pedestal profile and ballooning stability analysis. *Nuclear Fusion*, 62(8):086004, 2022.

[Réf20] D. Réfy, E. Solano, N. Vianello, et al. Identity of the JET M-mode and the ASDEX Upgrade I-phase phenomena. *Nuclear Fusion*, 60(5):056004, 2020.

[Rei17] F. Reimold, M. Wischmeier, S. Potzel, et al. The high field side high density region in SOLPS-modeling of nitrogen-seeded H-modes in ASDEX Upgrade. *Nuclear Materials and Energy*, 12:193–199, 2017.

[Rek21] R. Reksoatmodjo, S. Mordijck, J. Hughes, et al. The role of edge fueling in determining the pedestal density in high neutral opacity Alcator C-Mod experiments. *Nuclear Materials and Energy*, 27:100971, 2021.

[Roa18] European research roadmap to the realisation of fusion energy. Technical report, EUROfusion, Boltzmannstr. 2, 85748 Garching, Germany, 2018.

[Rog98] B. N. Rogers, J. F. Drake, and A. Zeiler. Phase Space of Tokamak Edge Turbulence, theL-HTransition, and the Formation of the Edge Pedestal. *Physical Review Letters*, 81(20):4396–4399, 1998.

[Rom15] M. Romanelli, V. Parail, P. d. S. A. Belo, et al. Modelling of plasma performance and transient density behaviour in the H-mode access for ITER gas fuelled scenarios. *Nuclear Fusion*, 55(9):093008, 2015.

[Sal15] A. Salmi, T. Tala, P. Mantica, et al. Particle source and edge transport studies in JET H-mode gas puff modulation experiments. In *42nd EPS Conference on Plasma Physics*. European Physical Society, 2015.

[Sch22] C. U. Schuster, E. Wolfrum, E. Fable, et al. Edge transport and fuelling studies via gas puff modulation in ASDEX Upgrade L-mode plasmas. *Nuclear Fusion*, 62(6):066035, 2022.

[Sco05] B. D. Scott. Drift wave versus interchange turbulence in tokamak geometry: Linear versus nonlinear mode structure. *Physics of Plasmas*, 12(6):062314, 2005.

[Sco07] B. D. Scott. Tokamak edge turbulence: background theory and computation. *Plasma Physics and Controlled Fusion*, 49(7):S25, 2007.

[Sha16] L. M. Shao, E. Wolfrum, F. Ryter, et al. On the role of the edge density profile for the L-H transition power threshold in ASDEX Upgrade. *Plasma Physics and Controlled Fusion*, 58(2):025004, 2016.

[Smi16] V. Smil. *Energy transitions: global and national perspectives*. ABC-CLIO, 2016.

[Sny11] P. Snyder, R. Groebner, J. Hughes, et al. A first-principles predictive model of the pedestal height and width: development, testing and ITER optimization with the EPED model. *Nuclear Fusion*, 51(10):103016, 2011.

[Sta07] G. Staebler, J. Kinsey, and R. Waltz. A theory-based transport model with comprehensive physics. *Physics of Plasmas*, 14(5):055909, 2007.

[Sta12] W. Stacey, R. Groebner, and T. Evans. Non-diffusive transport in the tokamak edge pedestal. *Nuclear Fusion*, 52(11):114020, 2012.

[Ste18] E. Stefanikova, L. Frassinetti, S. Saarelma, et al. Effect of the relative shift between the electron density and temperature pedestal position on the pedestal stability in JET-ILW and comparison with JET-C. *Nuclear Fusion*, 58(5):056010, 2018.

[Str99] U. Stroth, T. Geist, J. P. T. Koponen, et al. Evidence for Convective Inward Particle Transport in a Stellarator. *Physical Review Letters*, 82(5):928–931, 1999.

[Sut96] W. Suttrop, A. G. Peeters, et al. *Practical limitations to plasma edge electron temperature measurements by radiometry of electron cyclotron emission.* Max-Planck-Institut für Plasmaphysik, 1996.

[Sut11] W. Suttrop, T. Eich, J. Fuchs, et al. First observation of edge localized modes mitigation with resonant and nonresonant magnetic perturbations in ASDEX Upgrade. *Physical review letters*, 106(22):225004, 2011.

[Tal19] T. Tala, H. Nordman, A. Salmi, et al. Density peaking in JET—determined by fuelling or transport? *Nuclear Fusion*, 59(12):126030, 2019.

[Thr18] A. S. Thrysøe, M. Løiten, J. Madsen, et al. Plasma particle sources due to interactions with neutrals in a turbulent scrape-off layer of a toroidally confined plasma. *Physics of Plasmas*, 25(3):032307, 2018.

[Via17] N. Vianello, C. Tsui, C. Theiler, et al. Modification of SOL profiles and fluctuations with line-average density and divertor flux expansion in TCV. *Nuclear Fusion*, 57(11):116014, 2017.

[Via19] N. Vianello, D. Carralero, C. Tsui, et al. Scrape-off layer transport and filament characteristics in high-density tokamak regimes. *Nuclear Fusion*, 60(1):016001, 2019.

[Vie18] E. Viezzer. Access and sustainment of naturally ELM-free and small-ELM regimes. *Nuclear Fusion*, 58(11):115002, 2018.

[Vir20] P. Virtanen, R. Gommers, T. E. Oliphant, et al. SciPy 1.0: Fundamental Algorithms for Scientific Computing in Python. *Nature Methods*, 17:261–272, 2020.

[VW16] F. Van Wyk, E. Highcock, A. Schekochihin, et al. Transition to subcritical turbulence in a tokamak plasma. *Journal of Plasma Physics*, 82(6), 2016.

[Wag82] F. Wagner, G. Becker, K. Behringer, et al. Regime of improved confinement and high beta in neutral-beam-heated divertor discharges of the ASDEX tokamak. *Physical Review Letters*, 49(19):1408, 1982.

[Wag07] F. Wagner. A quarter-century of H-mode studies. *Plasma Physics and Controlled Fusion*, 49(12B):B1, 2007.

[Wan18] H. Wang, H. Guo, A. Leonard, et al. Effects of divertor geometry on H-mode pedestal structure in attached and detached plasmas in the DIII-D tokamak. *Nuclear Fusion*, 58(9):096014, 2018.

[Wen22] D. Wendler, R. Dux, R. Fischer, et al. Collisional radiative model for the evaluation of the thermal helium beam diagnostic at ASDEX upgrade. *Plasma Physics and Controlled Fusion*, 64(4):045004, 2022.

[Wes11] J. Wesson and D. J. Campbell. *Tokamaks*, volume 149. Oxford university press, 2011.

[Wil13] M. Willensdorfer, E. Fable, E. Wolfrum, et al. Particle transport analysis of the density build-up after the L–H transition in ASDEX Upgrade. *Nuclear Fusion*, 53(9):093020, 2013.

[Wil14] M. Willensdorfer, G. Birkenmeier, R. Fischer, et al. Characterization of the Li-BES at ASDEX Upgrade. *Plasma Physics and Controlled Fusion*, 56(2):025008, 2014.

[Wol93] E. Wolfrum, F. Aumayr, D. Wutte, et al. Fast lithium-beam spectroscopy of tokamak edge plasmas. *Review of scientific instruments*, 64(8):2285–2292, 1993.

[Zoh96] H. Zohm. Edge localized modes (ELMs). *Plasma Physics and Controlled Fusion*, 38(2):105, 1996.

[Zoh13] H. Zohm, C. Angioni, E. Fable, et al. On the physics guidelines for a tokamak DEMO. *Nuclear Fusion*, 53(7):073019, 2013.

[Zoh15] H. Zohm. *Magnetohydrodynamic stability of tokamaks.* John Wiley & Sons, 2015.

Acknowledgements

Science relies on many dedicated people to advance our knowledge and technology, with fusion being by no means an exception. Also this thesis would not have been possible without colleagues that supported me throughout my work.

First of all, I would like to mention my supervisors Ulrich Stroth and Elisabeth Wolfrum for all their input, feedback, fruitful discussions, proofreading of various manuscripts and the possibility to conduct the research presented in this work. Thank you for your guidance and advice! Biggy Perey and Gabriele Dörsch supported me in various organisational tasks for what I am grateful.

Conducting experiments and obtaining good, optimally evaluated data from a large experiment such as ASDEX Upgrade relies on a great number of technicians, engineers and scientists, that I cannot possibly list all, to set up the experiment, run the machine and maintain all the diagnostics. I nevertheless will explicitly mention Michael Griener, Elisabeth Wolfrum, Daniel Wendler, Alexander Bock, Rainer Fischer, Klara Bogar, Phillip Schneider, Diego Cruz Zabala, Marco Cavedon, Ulrike Plank, Matthias Willensdorfer, Balazs Tal, Klara Höfler, Jörg Hobirk, Rachael McDermott, Takashi Nishizawa, Volker Rhode, Pascal de Marne, Branka Vanovac, Dirk Stieglitz, Dominik Brida, Eleonora Viezzer, Jorge Santos, Pierre David, and Lidija Radovanovic.

Writing code and modelling with ASTRA were other tasks where I profited from our large institute. To show my appreciation for all the hints and discussions I would like to mention Michael Bergmann, Emiliano Fable, Giovanni Tardini, Marco Muraca, Christian Kiefer and Maximilian Reisner. I want to especially highlight Tobias Görler who conducted the linear GENE simulations for me.

Not yet mentioned, but highly valuable, were the discussions with Clemente Angioni, Thomas Eich, Peter Manz, Karl Lackner, Tilmann Lunt, Francois Ryter, Gregor Birkenmeier, David Coster, Arne Kallenbach and Jörg Stober. Supervising the thesis project of Pascal Windhager was an enriching experience.

But it is not only from a professional point of view that I am glad to have been at IPP for the last years. With outings to the Echinger See, Christmas parties, virtual get-togethers, conferences and having lunch together, I had the pleasure of getting to know many of my colleagues on a personal level, and I hope to have found long-lasting friendships.

Finally, I am incredibly lucky in being so profoundly supported by my dearly beloved wife Giulia.

Thank you!